

AN ALL-OPTICAL 4-BIT ADDER COMPOSED OF FABRY-PEROT DEVICES

A Dissertation

Presented in Partial Fulfillment of the Requirements for the

Degree of Doctor of Philosophy

with a

Major in Electrical Engineering

in the

College of Graduate Studies

University of Idaho

by

Jennifer E. Houle

Major Professor: Dennis Sullivan, Ph.D.

Committee Members: Mark Kuzyk, Ph.D.; Ata Zadehgol, Ph.D.; Ting-Yen Shih, Ph.D.

Department Administrator: Joseph Law, Ph.D.

May 2023

## ABSTRACT

This work models an all-optical 4-bit adder comprised of Fabry-Perot devices. Each device is composed of two silver mirrors on either side of a cavity made of a nonlinear Kerr material. These devices are optically bistable and suitable for fast logic operations on the order of picoseconds. An amplifying buffer is used between devices to adjust the transmitted signal's amplitude to the desired value, and to provide control for logic operations. This work uses the method of finite-difference time-domain (FDTD) in one-dimensional (1D) space to demonstrate the feasibility of the proposed idea.

## ACKNOWLEDGEMENTS

First, I want to thank my committee members: Dr. Dennis Sullivan, Dr. Mark Kuzyk, Dr. Ata Zadehgol, and Dr. Ting-Yen Shih. I truly appreciate their support in this process.

I'm extremely grateful to Dr. Dennis Sullivan for his amazing support over the many years I have studied electrical engineering. I very much doubt I would have pursued a Ph.D. without his encouragement as well as his logistical support as a distance student. I have learned so much about engineering from him, particularly regarding simulations. He has been extremely generous sharing his time and knowledge.

I would also like extend my sincere gratitude to Dr. Mark Kuzyk for his patience as he helped me understand the physics of nonlinear optics. His enthusiasm for the subject is contagious and his knowledge unparalleled. I appreciate the many years he helped guide this work.

Additionally, I would like to thank Dr. Ata Zadehgol for his keen attention to detail and insights. I have gained much of my knowledge in electromagnetics from him.

I also sincerely appreciate the expertise that Dr. Joseph Lanska shared with me regarding his FDTD formulations and Python code.

Finally, I would like to thank Dr. Herbert Hess for piquing my interest in research so many years ago as an undergraduate student.

## DEDICATION

Thank you to my wonderful family for supporting me through this endeavor. My husband, Bijan, and my incredible daughters have always been encouraging.

I want to thank my parents for being a constant source of love and support my entire life.

I also want to thank my friend Bob, who was the first person to tell me I would wind up with a Ph.D. some day. I think I was about eight years old at the time, and I am pretty sure I laughed when he told me that. He was, of course, right in the end.

# TABLE OF CONTENTS

ABSTRACT . . . . .	ii
ACKNOWLEDGEMENTS . . . . .	iii
DEDICATION . . . . .	iv
TABLE OF CONTENTS . . . . .	v
LIST OF FIGURES . . . . .	vii
CHAPTER 1: INTRODUCTION . . . . .	1
CHAPTER 2: THE FDTD METHOD . . . . .	4
MAXWELL'S EQUATIONS . . . . .	4
MAXWELL'S EQUATIONS IN FREE SPACE . . . . .	4
ONE-DIMENSIONAL FDTD FORMULATION IN FREE SPACE . . . . .	6
STABILITY FACTOR . . . . .	9
BOUNDARY CONDITIONS . . . . .	9
MATERIAL MODELS IN FDTD . . . . .	11
ONE-DIMENSIONAL FDTD FORMULATION IN COMPLEX MATERIALS . . . . .	11
PLASMA . . . . .	12
KERR EFFECT . . . . .	15
LORENTZ FORMULATION . . . . .	16
LORENTZ AND KERR COMBINED FORMULATION . . . . .	19
PLASMA, LORENTZ, AND KERR FORMULATION . . . . .	20
CHAPTER 3: FABRY-PEROT DEVICE IN FDTD SIMULATION . . . . .	21
INPUT . . . . .	21
FREE SPACE SIMULATION . . . . .	23
SILVER MIRRORS . . . . .	25
CAVITY OF MIRRORS . . . . .	30
WAVEFORMS BETWEEN THE MIRRORS . . . . .	35
KERR EFFECT . . . . .	36
LORENTZ FORMULATION . . . . .	44
CHAPTER 4: LOGIC GATES COMPOSED OF FABRY-PEROT DEVICES . . . . .	51
BASIC LOGIC GATE DESIGN . . . . .	51
BASIC OPERATION . . . . .	51
OPTICAL LOGIC INPUTS . . . . .	56

OR GATE . . . . .	56
AND GATE . . . . .	57
MAJORITY GATE . . . . .	57
XOR GATE . . . . .	62
ADDER DESIGN . . . . .	64
HALF-ADDER . . . . .	64
FULL-ADDER . . . . .	67
2-BIT ADDER . . . . .	69
CHALLENGES AND SOLUTIONS . . . . .	71
BUFFERING WITH AMPLITUDE STANDARDIZATION . . . . .	71
BUFFERING WITH PHASE STANDARDIZATION . . . . .	72
PHASE DELAYS . . . . .	74
BUFFER PLACEMENT . . . . .	74
3-BIT AND 4-BIT ADDERS . . . . .	83
3-BIT ADDER . . . . .	83
4-BIT ADDER . . . . .	85
CHAPTER 5: CONCLUSIONS . . . . .	87
REFERENCES . . . . .	88
APPENDIX A: KERR APPROXIMATION COMPARISON . . . . .	93
APPENDIX B: LORENTZ FORMULATION COMPARISON . . . . .	100
APPENDIX C: THE PERFECTLY MATCHED LAYER (PML) . . . . .	106
APPENDIX D: TOTAL FIELD/SCATTERED FIELD . . . . .	112

## LIST OF FIGURES

2.1	Yee cell used in this work. The green dashed line shows the simulation propagation direction being used. . . . .	7
3.1	Plateau function of Eq. (3.1) with $a = 4$ showing (a) the function itself, (b) the function's first derivative, and (c) the function's second derivative. There are no discontinuities. . . . .	22
3.2	Hanning window plus plateau function of Eq. (3.2) showing (a) the function itself, (b) the function's first derivative, and (c) the function's second derivative. There are discontinuities in the second derivative. The function is normalized. . . . .	23
3.3	Example of a sinusoidal input contained within the envelope of Eq. (3.1). The simulations will typically use a much longer input consisting of more sinusoidal cycles. . . . .	24
3.4	Simulation space of 625 cells with free space and the PML. The input travels from the origin to the right. . . . .	24
3.5	Simulation space captured at (a) 0.01 ps, (b) 0.02 ps, and (c) 0.21 ps showing the input of Fig. 3.3 moving left to right and dissipating to the right of the PML. By 0.21 ps, the signal has dissipated entirely. The input pulse is wide in (b) to demonstrate the effectiveness of the PML and shows the signal quickly decaying to zero on the right side of the figure within the PML. . . . .	25
3.6	A comparison of the (a) real and (b) imaginary permittivity ( $\varepsilon$ ) of silver plasma across a range of frequencies from the Ishimaru model and the experimental values from Johnson. The vertical blue lines indicate the fundamental frequency of 500 THz and the third harmonic of 1500 THz. The Ishimaru model is used in these simulations. . . . .	26
3.7	Simulation showing the progression of an electric field pulse of 500 THz interacting with a silver plasma mirror. The pulse (a) moves to the right, (b) hits the plasma mirror, which is six cells wide, splitting, and (c) moves away from the mirror. The peak electric field strengths are displayed on the right of each plot showing the peak to the left of the plasma mirror ( $E(L)$ ) and to the right of the plasma mirror ( $E(R)$ ). . . . .	27

3.8	Fourier transforms of the signals corresponding to Fig. 3.7 of (a) the incident wave to the left of the plasma, (b) the initial state to the right of the plasma showing no signal, (c) the reflected signal as the incident signal is still interacting with the plasma, (d) the transmitted signal as the incident signal is still interacting with the plasma, (e) the reflected signal after the incident signal stops interacting with the plasma, and (f) the transmitted signal after the incident signal stops interacting with the plasma. The reflection is obtained by dividing the reflected value at 500 THz in (e) by the incident value at 500 THz in (a). For a 6-cell mirror, the reflection is 94.7%. . . . .	28
3.9	Simulation showing the progression of an electric field pulse of 10,000 THz interacting with a silver plasma mirror. The pulse (a) moves to the right, (b) hits a mirror six cells wide, and (c) moves away from the mirror. The peak electric field strengths are displayed on the right of each plot showing the peak to the left of the plasma ( $E(L)$ ) and to the right of the plasma ( $E(R)$ ). Almost the entire signal is transmitted since the signal is well above the plasma frequency. . . . .	29
3.10	Reflectivity as a function of the plasma mirror thickness, measured in number of cells. The green vertical line is the chosen thickness of six cells, and the green horizontal line is the corresponding reflectivity (simulated in Fig. 3.7 and Fig. 3.8). A thicker plasma mirror is more reflective. . . . .	30
3.11	Intensity absorption as a function of the plasma mirror thickness, measured in number of cells. The green vertical line is the chosen thickness of six cells, and the green horizontal line is the corresponding absorption (simulated in Fig. 3.7 and Fig. 3.8). As expected, there is less loss with a thicker plasma mirror because there is less signal moving through the lossy plasma mirror. . . . .	30
3.12	Simulation setup of two 6-cell thick mirrors used to form a cavity. The pulse moves from left to right starting at the origin. Transmitted data is saved to the right of the second mirror. Each mirror is six cells thick, and there are a varying number of cells comprising the cavity. . . . .	31
3.13	Transmitted intensity compared to the number of cavity cells. The green vertical lines correspond to half wavelengths for a 500 THz signal. Peak transmission is slightly offset from each of the lines due to the 6-cell plasma mirrors on either end of the cavity. . . . .	32
3.14	This shows the maximum transmission based on a 2.5-wavelength cavity composed of two silver mirrors. The cavity is 290 cells. (a) The intensity-over-time plot, (b) the cavity intensity versus the input intensity, and (c) the transmitted intensity versus the input intensity. . . . .	33



- 3.15 Peak  $E_z$  transmitted through the cavity versus cavity length for different mirror thicknesses while the reflection is held constant. The ideal cavity length is affected by the amount of signal absorbed in each mirror, as well as the complex interaction of the signal with the mirrors. 33
- 3.16 Transmission based on cavity length with the mirror thickness and reflection held constant for two different cell sizes. This shows consistency in the cavity lengths associated with peak transmission. . . . . 34
- 3.17 Intensity versus frequency for the FDTD simulation data and using Eq. (3.5). There is a manual adjustment to move the peak transmission of the equation to 500 THz to account for the mirrors. This shows that a constant separation of mirrors will allow peak transmission at frequencies that align generally with Eq. (3.5). . . . . 35
- 3.18 The magnitudes of  $E_y$  and  $H_z$  oscillate during the simulation. (a)-(d) capture points in time showing this oscillation within the cavity. The mirror surfaces are shown as green vertical lines. The light blue vertical line is the origin. The transmitted fields remain constant in magnitude. These snapshots occur when the input is at the maximum and held in the plateau region. . . . . 36
- 3.19 Simulation setup of two 6-cell thick mirrors used to form a cavity with a Kerr material in between the mirrors. The data moves from left to right starting at the origin. Transmitted data is saved to the right of the second mirror. . . . . 37
- 3.20 Transmitted intensity compared to the number of cavity cells of the structure of Fig. 3.19 simulating every even cavity length. The green vertical lines correspond to half wavelengths for a 500 THz signal (a cavity with a length of  $\lambda$ ,  $3\lambda/2$ ,  $2\lambda$ , etc.) in a material with a refractive index of 1.5. Peak transmission does not occur exactly at the predicted cavity lengths due to the 6-cell plasma mirrors on either end of the cavity, and because the Kerr effect will alter the effective refractive index. However, the peaks are half an integer wavelength offset from each other, as expected. The difference in peak transmission intensities is partially due to the granularity of the simulation. Some peaks show higher transmission than others since the ideal cavity length for transmission is not precisely met in this discrete system. . . . . 37
- 3.21 Simulation of a cavity consisting of two 6-cell silver plasma mirrors with a Kerr material in between. This shows the (a) intensities over time, (b) cavity intensity (averaged across the cavity) versus input intensity, and (c) transmitted intensity (calculated to the right of the cavity and time-averaged) versus input intensity. Both (b) and (c) show one hysteresis loop. . 38

- 3.22 Simulation of a cavity consisting of two silver plasma mirrors with a Kerr material in between. The input intensity is raised higher than in Fig. 3.21. This shows (a) the cavity intensity (averaged across the cavity) versus input intensity, and (b) the transmitted intensity (calculated to the right of the cavity and time-averaged) versus input intensity. Both (a) and (b) show one hysteresis loop despite the higher input intensity than in Fig. 3.21(b) and Fig. 3.21(c). . . . . 39
- 3.23 Stairstep simulation showing intensity over time of a cavity consisting of two 6-cell silver plasma mirrors with a Kerr material in between. The dots show the values recorded at a point of time during which the simulation has stabilized. (a) The input increases from a low value, and (b) the input decreases from an initial high value. . . . . 40
- 3.24 Simulation of a cavity consisting of two 6-cell silver plasma mirrors with a Kerr material in between. This plots the transmitted intensity (calculated to the right of the cavity and time-averaged) versus input intensity, and the plot shows one hysteresis loop. The dots correspond to the dots taken from Fig. 3.23. . . . . 41
- 3.25 Hysteresis loops for simulations with a varying duration of time. The longest simulation, 70 ps, corresponds to Fig. 3.21. A shorter simulation distorts the hysteresis loop shape. . . . . 42
- 3.26 The magnitudes of  $E_y$  and  $H_z$  oscillate during the simulation of a Kerr cavity surrounded by mirrors. (a)-(d) capture points in time showing this oscillation within the cavity. The mirror surfaces are shown as green vertical lines. The light blue vertical line is the origin. The transmitted fields maintain a constant magnitude. These snapshots occur when the input is at the maximum and held in the plateau region. . . . . 43
- 3.27 (a) The transmitted electric field  $E_y$  and (b) its Fourier transform induced by the Kerr cavity. The vertical dashed cyan lines in (b) correspond to the fundamental, third, and fifth harmonics. 43
- 3.28 Simulation setup of two 6-cell thick mirrors used to form a cavity with a Kerr/Lorentz material in between the mirrors. The pulse propagates from left to right starting at the origin. Transmitted data is saved to the right of the second mirror. . . . . 44
- 3.29 The transmitted intensity versus the number of cavity cells of the structure of Fig. 3.28 with even numbers of cavity cells simulated. The green vertical lines correspond to half wavelengths for a 500 THz signal in a material with a refractive index of 1.5. Peak transmission does not occur exactly at the predicted number of cavity cells due to the 6-cell plasma mirrors on either end the cavity and due to the effective refractive index change caused by the Kerr material. The difference in peak transmission amplitude is partially due to the granularity of the simulation. . . . . 45

- 3.30 The transmitted intensity as a function of the number of cavity cells of the structure of Fig. 3.19 compared to Fig. 3.28. The green vertical line corresponds to a half wavelength for a 500 THz signal in a material with a refractive index of 1.5. Peak transmission occurs with a cavity length of one cell less when comparing the Kerr/Lorentz cavity simulation to the Kerr-only cavity simulation. . . . . 45
- 3.31 Simulation of a cavity consisting of two 6-cell silver plasma mirrors with a Kerr/Lorentz material in between. This shows (a) the intensity over time, (b) the cavity intensity (averaged across the cavity) versus input intensity, and (c) the transmitted intensity (calculated to the right of the cavity and time-averaged) versus input intensity. Both (b) and (c) show one hysteresis loop. . . . . 46
- 3.32 Simulation of a cavity consisting of two 6-cell silver plasma mirrors with a Kerr/Lorentz material compared to a Kerr-only material in between. Each cavity between the mirrors is 223 cells. This shows (a) the transmitted intensity over time around the rising edge with the damped ringing when the Lorentz effect is included and (b) the transmitted intensity versus input intensity. Note that the number of cells that trigger the nonlinear response differs in each case due to the Lorentz characteristics affecting the effective refractive index. . . . . 46
- 3.33 Simulation of a cavity consisting of two silver plasma mirrors with a Kerr/Lorentz material in between. The input intensity is raised higher than in Fig. 3.31. This shows the (a) cavity intensity (averaged across the cavity) versus input intensity, and the (b) transmitted intensity (calculated to the right of the cavity and time-averaged) versus input intensity. Despite the higher input intensity compared to Fig. 3.31(b) and Fig. 3.31(c), both (a) and (b) show one hysteresis loop. Compared to the Kerr-only cavity in Fig. 3.22, there is significantly less ringing on the rising edge. . . . . 47
- 3.34 Stairstep simulation showing intensity over time of a cavity consisting of two 6-cell silver plasma mirrors with a Kerr/Lorentz material in between. The dots show the values recorded at a point in time during which the simulation has stabilized. (a) The input increases from a low value, and (b) the input decreases from an initial high value. . . . . 48
- 3.35 Simulation of a cavity consisting of two 6-cell silver plasma mirrors with a Kerr/Lorentz material in between. This plots the transmitted intensity versus input intensity and shows one hysteresis loop. The dots on the plot correspond to the dots taken from Fig. 3.34. . . . . 49

3.36	The magnitudes of $E_y$ and $H_z$ oscillate during the simulation of a Kerr/Lorentz cavity surrounded by mirrors. (a)-(d) capture points in time showing this oscillation within the cavity. The mirror surfaces are shown as green vertical lines. The light blue vertical line is the origin. The transmitted fields maintain a constant magnitude. These snapshots occur when the input is at the maximum and held in the plateau region. The shapes resemble those in Fig. 3.26 for the Kerr-only material. . . . .	49
3.37	(a) The transmitted $E_y$ signal and (b) its Fourier transform during the nonlinear operating region for a Kerr/Lorentz cavity surrounded by silver mirrors. The vertical dashed cyan lines in (b) correspond to the fundamental, third, and fifth harmonics. . . . .	50
3.38	Simulation of a cavity consisting of two silver plasma mirrors with a Kerr/Lorentz material in between. The transmitted intensity (calculated to the right of the cavity and time-averaged) is plotted versus the input intensity, showing hysteresis. Lorentz parameters are compared by (a) adjusting $\omega_p$ and (b) adjusting $\omega_0$ . The cavity length is held constant at 223 cells. If these parameters are adjusted much more, the ideal cavity length for peak transmission changes because the effective refractive index changes, and the simulation needs to run with an adjusted number of cavity cells to maintain hysteresis. Decreasing $\omega_p$ or increasing $\omega_0$ from the values of DR1-PMMA lead to more ringing and more optical bistability. . . . .	50
4.1	The Fabry-Perot device used in this work. . . . .	52
4.2	Transmitted intensity plotted as a function of input intensity. Once the input intensity is beyond the nonlinear threshold, the transmitted intensity varies much less than the input intensity. . . . .	53
4.3	$E_y$ phase as a function of cell location. Cells are located relative to the right edge of the problem space. . . . .	53
4.4	Filtering of the transmitted signal showing (a) the original transmitted signal, (b) the Fourier transform of the original transmitted signal, (c) the transmitted signal filtered at 500 THz, and (d) the Fourier transform of the filtered, transmitted signal. . . . .	54
4.5	Buffering device used for input generation. The input on the left of the figure is generated with a sinusoid within the envelope given by Eq. (3.1). This is input into a Fabry-Perot device. The transmitted (output) signal, after filtering and optical isolation, becomes the input to the logic gates. . . . .	56
4.6	Example of (a) an input signal to the buffering device, and (b) the corresponding transmitted signal from the input buffering device used for the inputs to logic gates. The orange dots are the locations at which the logical state is saved, so this example shows four input states. . . .	56

- 4.7 (a) Schematic of the OR gate including the input amplifiers, which amplify each signal 2.5X.  
 (b) The symbol used to represent the schematic of (a). . . . . 57
- 4.8 OR functionality corresponding to Table 4.3 with the inputs (a) A (post amplification) and  
 (b) B (post amplification) generated with input buffer devices. These inputs are used to  
 generate (c) the transmitted OR gate's signal. The orange dots correspond to the time at  
 which the values are examined for logic values. Any values above the horizontal green line are  
 considered a '1' and those below the green line are '0.' (d) The transmitted and input (post  
 amplification) intensity comparison of the OR gate, showing that the output is naturally  
 buffered compared to the input by the Fabry-Perot device. . . . . 58
- 4.9 (a) Schematic of the AND gate including the input amplifiers, which amplify each signal  
 1.5X. (b) The symbol used to represent the schematic of (a). . . . . 58
- 4.10 AND functionality corresponding to Table 4.4 with the inputs (a) A (post amplification)  
 and (b) B (post amplification) from input buffer devices. These inputs are used to generate  
 (c) the transmitted AND gate's signal. The orange dots correspond to the time at which  
 the values are examined for logic values. Any values above the horizontal green line are  
 considered a '1' and those below the green line are '0.' (d) Transmitted and input (post  
 amplification) intensity comparison of the AND gate, showing that the output is naturally  
 buffered compared to the inputs by the Fabry-Perot device. . . . . 59
- 4.11 (a) Schematic of the majority gate, including the input amplifiers, which amplify each signal  
 1.2X. (b) The symbol used to represent the schematic of (a). . . . . 60
- 4.12 Majority gate functionality corresponding to Table 4.5 with the inputs (a) A (post ampli-  
 fication), (b) B (post amplification), and (c) C (post amplification) from input buffer devices.  
 These inputs are used to generate (d) the majority gate's transmitted signal. The orange  
 dots correspond to the time at which the values are examined for logic values. Any values  
 above the horizontal green line are considered a '1' and those below the green line are '0.' . . . 61
- 4.13 The transmitted and input (post amplification) intensity comparison of the majority gate,  
 showing that the output is again naturally buffered compared to the inputs by the Fabry-Perot  
 device. . . . . 61
- 4.14 (a) Schematic of the XOR gate including the input amplifiers, which amplify each signal  
 3X. There is a 180° phase shift on one of the inputs. (b) The symbol used to represent the  
 schematic of (a). . . . . 62

- 4.15 XOR functionality corresponding to Table 4.6 with the inputs (a) A (post amplification) and (b) B (post amplification) from input buffer devices. These inputs are used to generate (c) the transmitted XOR gate's signal. The orange dots correspond to the time at which the values are examined for logic values. Any values above the horizontal green line are considered a '1' and those below the green line are '0.' (d) Transmitted and input (post amplification) intensity comparison of the XOR gate. . . . . 63
- 4.16 Transmitted  $E_y$  from the XOR device shown in Fig. 4.15(c) corresponding to the second and third orange dots. A steady reference sinusoidal wave is shown in orange to compare with the transmitted  $E_y$  shown in blue. Though the magnitude is the same in both cases, (a)  $E_y$  is out of phase with the reference signal, corresponding to input B being a '1,' and (b)  $E_y$  is in phase with the reference signal, corresponding to input A being '1.' . . . . . 63
- 4.17 (a) The phase-compensated XOR gate consists of two splitters, an OR gate, an AND gate, two amplifiers, a combiner, one Fabry-Perot device, a filter, and an optical isolator. Since the splitter shifts one output  $180^\circ$ , the phase plate of Fig. 4.14 is not necessary. This version of the XOR gate ensures the output has the same phase whether only input A or input B is a '1.' (b) The schematic used for the phase-compensated XOR gate going forward. This includes the AND and OR gates in the schematic to show how many Fabry-Perot devices are required in a schematic. The area enclosed in a rectangle in (a) is abbreviated as shown in (b). Note one input of the XOR gate expects an input phase shifted  $180^\circ$  compared to the other input. . . . . 65
- 4.18 XOR functionality corresponding to Fig. 4.17 and Table 4.7 with the same inputs A and B from Figs. 4.15(a) and (b). The intermediate outputs of (a) OR from Fig. 4.17 and (b) AND from Fig. 4.17 are fed into the single XOR gate, resulting in (c) the transmitted XOR gate's signal. The orange dots correspond to the time at which the values are examined for logic values. Any values above the horizontal green line are considered a '1' and those below the green line are '0.' . . . . . 66
- 4.19 Transmitted  $E_y$ , the intensity of which was shown in Fig. 4.18(c), generated by the output of the phase-compensated XOR in Fig. 4.17(a). A steady reference sinusoidal wave is shown in orange to compare with the transmitted  $E_y$  shown in blue. The magnitude is the same in both cases. Additionally, (a)  $E_y$  is in phase with the reference signal, corresponding to input B being a '1' at the second orange dot in Fig. 4.18(c), and (b)  $E_y$  is in phase with the reference signal, corresponding to input A being '1' at the third orange dot in Fig. 4.18(c). . . 66
- 4.20 The half-adder schematic. . . . . 67
- 4.21 The full-adder schematic. . . . . 68

4.22	Full-adder functionality corresponding to Fig. 4.21 and Table 4.9 with the outputs (transmitted intensities) of (a) the last Fabry-Perot device used to generate the SUM bit of Fig. 4.21 (XOR 2) and (b) the last Fabry-Perot device used to generate the CARRY bit from Fig. 4.21 (the majority gate). The orange dots correspond to the time at which the values are examined for logic values. . . . .	68
4.23	2-bit adder composed of one half-adder (Fig. 4.20) and one full-adder (Fig. 4.21). . . . .	69
4.24	2-bit adder functionality corresponding to Fig. 4.23 and Table 4.10 with the outputs (transmitted intensities) of (a) the last Fabry-Perot device used in the SUM 0 bit generation (XOR in Fig. 4.20), (b) the last Fabry-Perot device used in the CARRY 0 bit generation (AND in Fig. 4.20), (c) the last Fabry-Perot device used in the SUM 1 bit generation (XOR 2 in Fig. 4.21), and (d) the last Fabry-Perot device used in the CARRY 1 bit generation (the majority gate in Fig. 4.21). The orange dots correspond to the time at which the values are examined for logic values. A '1' is above the horizontal green dashed line and a '0' is below the same line. . . . .	70
4.25	(a) Schematic of the buffer including the input amplifier of 3X. (b) The symbol used to represent the schematic of (a). . . . .	71
4.26	The functionality of several devices in Fig. 4.21. The inputs to the full-adder are shown in Table 4.10. This shows (a) the input (post amplification) and (b) the output (transmitted) intensity from the Fabry-Perot device acting as OR 2; (c) the input (post amplification) and (d) the output (transmitted) intensity from the Fabry-Perot device acting as AND 2; and (e) the input (post amplification) and (f) the output (transmitted) intensity from the Fabry-Perot device acting as XOR 2 to generate the SUM bit 1 data. The orange dots correspond to the time at which the magnitudes are examined for logic values. Each value is correct, but the input intensities vary significantly when comparing the '1' values to each other or the '0' values to each other. The result of combining the signals in (b) and (d), and then amplifying them, is shown in (e), which is the input to the Fabry-Perot device representing XOR 2. The intensity at the fourth dot in (e) shows very little margin for being a '1' compared to the intensity at other times because outputs of OR 2 and AND 2 vary significantly from one another. Due to the phase differences, there is also destructive interference on the input at this location. . . . .	73
4.27	Full-adder with two buffers. . . . .	74

4.28	The functionality of several devices corresponding to Fig. 4.27. The inputs to the full-adder are shown in Table 4.10. This shows (a) the input (post amplification) and (b) the output (transmitted) intensity from the Fabry-Perot device acting as the buffer after OR 2; (c) the input (post amplification) and (d) the output (transmitted) intensity from the Fabry-Perot device acting as the buffer after AND 2; and (e) the input (post amplification) and (f) the output (transmitted) intensity from the Fabry-Perot device acting as XOR 2 to generate the SUM bit 1 data. The orange dots correspond to the time at which the magnitudes are examined for logic values. The margin in (e) is improved compared to Fig. 4.26(e), particularly when looking at location 4 (at approximately 10.5 ps). . . . .	75
4.29	The intensity transmitted from the second OR gate of the full-adder and through two subsequent series buffers. Each additional buffer causes the output ‘1’ levels to be more consistent. The intensity is recorded at the eight times indicated by dots in Fig. 4.26(b). . . . .	76
4.30	The phase versus (a) the intensity (post amplification) at the origin and (b) the intensity transmitted. There is a significant difference in phase when looking at input intensities above versus below the nonlinear threshold. The phase ranges between 1.54 and 1.68 radians when the signal is below the nonlinear threshold (representing a ‘0’) compared to between -0.27 and 0.09 radians when the signal is above the nonlinear threshold (representing a ‘1’). The difference in the phases above and below the nonlinear threshold explains why destructive interference can occur when combining signals. . . . .	76
4.31	2-bit adder CARRY 1’s path with buffers. . . . .	77
4.32	The input and transmitted intensities for the Fabry-Perot device used as a majority gate to generate the CARRY 1 signal. The inputs are the same as in Table 4.10, but each device intentionally creates a phase shift of 0.64 radians. The origin intensity (post amplification) and the cavity intensity (a) without any buffers and (b) with the buffers as shown in Fig. 4.31. The CARRY 1 output (transmitted) signal alone is shown for the circuit (c) without any buffers and (d) with the buffers as shown in Fig. 4.31. Without the buffers, the output (transmitted) signal marginally fails at the 5th and 7th locations shown in (c), but it clearly passes with the additional buffers as shown in (d). . . . .	78
4.33	Full-adder with four buffers added. Two buffers are added to each input of the second OR, which are also the inputs to the second AND gate. . . . .	79



- 4.34 The (a) the input (post amplification) to the Fabry-Perot device acting as the XOR 1 gate and (b) its corresponding output. The (c) the input (post amplification) to the Fabry-Perot device acting as the AND gate of the half-adder to generate the CARRY 0 bit and (d) its corresponding output. The outputs of (b) and (d) act as inputs to the second OR gate of the full-adder. Although the transmitted intensities can be clearly identified in (b) and (d) as ‘0’ or ‘1,’ the ‘0’ values are not at exactly zero and therefore have a phase shift associated with them. This is a simulation of the full-adder without buffers. . . . . 80
- 4.35 The input electric fields to the OR 2 gate of the full-adder without buffers given with respect to a reference signal at the time of (a) the third dot of the transmitted XOR 1 signal in Fig. 4.34(b), (b) the fourth dot of the transmitted XOR 1 signal in Fig. 4.34(b), (c) the third dot of the transmitted CARRY signal in Fig. 4.34(d), (d) the fourth dot of the transmitted CARRY signal in Fig. 4.34(d). Although the signals of (a) and (d) both represent a logic ‘0,’ these do not have amplitudes of zero. The phase shift of (d) can interact with the signal shown in (b) to reduce the combined input to the subsequent OR and AND gates. . . . . 81
- 4.36 The input intensity to the OR 2 gate of the full-adder without buffers. There is little margin at the fourth dot around 10.5 ps due to the destructive interference of the phase-shifted zero input of Fig. 4.35(d). . . . . 81
- 4.37 The input intensity to the OR 2 gate of the full-adder with two buffers as in Fig. 4.33. There is far more margin at the fourth dot around 10.5 ps compared to the fourth dot in Fig. 4.36. 82
- 4.38 Adding buffers, as in Fig. 4.33, this shows the input electric fields to the second OR gate of the full-adder, given with respect to a reference signal, at the time of (a) the third dot of the buffered XOR 1 signal in Fig. 4.34(b), (b) the fourth dot of the buffered XOR 1 signal in Fig. 4.34(b), (c) the third dot of the buffered CARRY signal in Fig. 4.34(d), (d) the fourth dot of the buffered CARRY signal signal in Fig. 4.34(d). The signals of (a) and (d) representing input 0’s are smaller than those in Fig. 4.35, creating less potential problems with destructive interference. . . . . 82
- 4.39 3-bit adder composed of one half-adder and two full-adders. . . . . 83
- 4.40 3-bit adder functionality corresponding to Fig. 4.39 and Table 4.11 with the outputs of (a) the SUM 2 bit and (b) the CARRY 2 bit. The orange dots correspond to the time at which the values are examined for logic values. A ‘1’ is above the horizontal green dashed line and a ‘0’ is below the same line. The outputs for S0, S1, C0, and C1 were shown in Fig. 4.24, with C1 being an input to the third stage of the adder. . . . . 84
- 4.41 4-bit adder composed of one half-adder and three full-adders. . . . . 85

4.42 4-bit adder functionality corresponding to Fig. 4.41 and Table 4.12 with the outputs of (a) the SUM 3 bit, (b) the CARRY 3 bit. The orange dots correspond to the time at which the values are examined for logic values. A ‘1’ is above the horizontal green dashed line and a ‘0’ is below the same line. The outputs for S0, S1, C0, and C1 were shown in Fig. 4.24, and S2 and C2 were shown in Fig. 4.40, with C2 being an input to the fourth stage of the adder. . . . 86

A.1 (a) Comparisons of a sine wave cubed of 500 THz compared with the two estimation methods in Eq. (A.1) and Eq. (A.2), where  $x[n]$  is the sine wave at a particular time step. All three methods appear indistinguishable. (b) The difference between each estimation method and the actual sine wave cubed. The method of Eq. (A.1) is much more accurate, though both methods show small errors. . . . . 94

A.2 Comparisons of a sine wave cubed compared with the two estimation methods in Eq. (A.1) and Eq. (A.2), where  $x[n]$  is the sine wave at a particular time step. (a) The sine wave is 1500 THz and (b) the sine wave is 2500 THz. The errors for both methods are small, though for 2500 THz, the error using Eq. (A.1) is less than 5% of the error using Eq. (A.2). . . . . 94

A.3 (a) Plot of a sine wave with components at 500 THz, 1500 THz, and 2500 THz. (b) Comparison of the two estimation methods of Eq. (A.1) and Eq. (A.2) to the sine wave cubed. The errors for both methods are small, but the error using Eq. (A.1) is less than 3.5% of the error using Eq. (A.2). . . . . 95

A.4 Setup for the Kerr cavity simulation. . . . . 95

A.5 Using the method of Eq. (A.1), (a) the transmitted wave from Fig. A.4 for a cavity with  $\chi^{(3)} = 1 \times 10^{-5} \frac{cm^3}{erg}$  and (b) the corresponding spatial Fourier transform. Using the method of Eq. (A.2), (c) the transmitted wave from Fig. A.4 for a cavity with  $\chi^{(3)} = 1 \times 10^{-5} \frac{cm^3}{erg}$  and (d) the corresponding spatial Fourier transform. Both results are similar. . . . . 96

A.6 Using the method of Eq. (A.1), (a) the transmitted wave from Fig. A.4 for a cavity with  $\chi^{(3)} = 5 \times 10^{-4} \frac{cm^3}{erg}$  and (b) the corresponding spatial Fourier transform. Using the method of Eq. (A.2), (c) the transmitted wave from Fig. A.4 for a cavity with  $\chi^{(3)} = 5 \times 10^{-4} \frac{cm^3}{erg}$  and (d) the corresponding spatial Fourier transform. Equation (A.1) results in more high frequency components. . . . . 97

A.7 Comparison of the two approximation methods of Eq. (A.1) and Eq. (A.2) when looking at the intensity versus input intensity for (a) the cavity, and (b) to the right of the cavity (transmitted). There is a small difference when looking at the falling edge of the transmitted signal. . . . . 98

B.1 Comparison of the coefficients defined in Eq. (B.11) and Eq. (B.15). The values are identical given that  $\Delta t \cdot \beta$  and  $\Delta t \cdot \gamma/2$  are small, with  $\beta$  related to  $\gamma$  and  $\omega_0$  in Eq. (B.14b). . . . . 104

C.1 The electric field at various times within the simulation space with a wave inserted at the origin moving right. (a-c) The right PML of eight cells absorbs the signal, and (d) eventually the entire signal has been absorbed. . . . . 110

D.1 An input to an FDTD simulation with a simple input sinusoid added to  $E_y$ , in the manner of Eqs. (D.1), at the center of the simulation space, represented by the vertical green line. . . . . 113

D.2 An input to an FDTD simulation with a single-directional input sinusoid added to  $E_y$  at the center of the simulation space, represented by the vertical green line. The input is defined by Eqs. (D.4) and (D.5). . . . . 114

## CHAPTER 1: INTRODUCTION

The idea of optical computing has existed since at least the 1960s [1]. Optical computers have promise in high-bandwidth, high-speed, and high efficiency though there are numerous challenges associated with this technology [2, 3].

Traditional electronic computing systems are running into a range of challenges due to shrinking form-factors. For Moore's law to continue to hold, it is necessary to innovate with new technologies instead of simply continuing to reduce transistor sizes [4, 5, 6, 7]. When decreasing device sizes, tradeoffs must be evaluated related to power consumption, transistor leakage, and speed [4, 6]. The energy loss in the form of heat generation becomes problematic. Light can move much more quickly since photons do not interact whereas electrons do interact due to the capacitance experienced. Further, using light, the transmission of information with wavelength division multiplexing becomes possible as well as inherent parallel processing capabilities [8]. The inherent advantages of light are particularly interesting in the fields of artificial intelligence [9] and image processing [10, 11].

There has been extensive research on optoelectronic devices [12]. These have the advantage of integrating with traditional electronic devices on a single chip, and many designs make use of existing silicon technologies to leverage current manufacturing knowledge [13]. Examples of the technologies being investigated are silicon-on-insulator and silicon nitride [12]. However, the conversion between electricity and light can be inefficient [11]. Methods of improving those connections are being investigated [14, 15].

This work focuses purely on optical computing, specifically on digital optical functions. There are many types of photonic logic, many of which use nonlinear optical effects. Some of the categories of optical logic gates include semiconductor optical amplifiers [16], plasmonics [17, 18, 19, 20], linear photonic crystals [21], nonlinear photonic crystals [22, 23, 24, 25, 26, 27, 28, 29, 30, 31], Mach-Zehnder interferometers [32], and multi-mode interference couplers [33]. Basic logic gates have been designed, including OR, AND, XOR, NOR, and NAND, as well as other components such as multiplexers. Further, many half and full-adders have been developed [17, 34, 35, 36, 37, 38, 39], and 2-bit adders have also been designed [40]. Adders are an essential part of an Arithmetic-Logic Unit (ALU) in processors.

In particular, there are many papers being published on photonic crystals [22, 23, 24, 25, 26, 27, 28, 29, 30, 31, 34, 37, 39, 40, 41]. Photonic crystals consist of a lattice of vertical silicon dielectric rods. Certain rods are omitted to create waveguides. Cavities and resonators are often created in a similar manner [22, 26, 27, 29, 34, 37, 39, 40]. Additionally, a nonlinear material, typically with Kerr characteristics, is used within the lattice to provide nonlinear effects for nonlinear devices. The arrangement, size, and rod material will affect the photonic band gap, controlling the frequencies of light

transmitted [22, 26, 29, 34, 37]. As light moves through the waveguides of a device, the input signals interact for the desired logic effect. These devices are typically simulated using the Finite-Difference Time-Domain (FDTD) method. Some of the advantages of these devices include small size, on the order of one wavelength, low power consumption, fast speeds, and the ability to leverage silicon fabrication processes when the photonic crystals are silicon-based. However, there are potential disadvantages, including the need for precise phase and wavelength control, with more than one wavelength sometimes being output at different ports leading to cascading issues in certain designs [37]. There are also physical challenges to creating the structures, with models typically representing infinitely high rods [2].

Several surveys of photonic logic have been published comparing many of these technologies [2, 12]. These surveys show the variety and creative solutions being proposed for optical logic. At this point no single technology is clearly dominating the field. Many of the adders in the literature are still in the simulation phase of design. Manufacturing capabilities have generally not caught up with the designs, though some photonic devices can be manufactured [42]. Much of the work on optical adders has presented problems with the ability to cascade devices. Some of the previously proposed designs are prohibitively large for use in an ALU.

This work explores using Fabry-Perot devices to create a 4-bit all-optical adder. Simulations have demonstrated these devices are suited for digital optical functions due to being optically bistable. A single frequency of light is used throughout the adder with the results matching the intended functions of a 4-bit adder. Several potential designs are explored, and these provide flexibility for future design improvements. This full-adder has very fast switching times that do not require additional phase shifts.

These devices require input-output isolation and amplifiers between stages. As a result, the footprint of these devices is much larger to that of traditional CMOS transistors. Additionally, fanout will be a potential challenge. However, despite these limitations, the inherent advantages of light for certain applications necessitate the development of all-optical processors. Fabry-Perot devices provide an alternate technology to those already proposed.

This work utilizes the FDTD in 1D space method for simulations. The FDTD method is commonly used for evaluating optical logic gates [21, 22, 24, 26, 28, 29, 34, 39]. The FDTD method allows the direct implementation of Maxwell's equations using complex material. In the Fabry-Perot devices, three types of media/phenomena will be simulated. Highly reflective silver plasma will be used as a coating on each end of the Fabry-Perot device. The device's characteristics will be modeled on Disperse Red 1 (DR1) dye doped in poly(methyl methacrylate) (PMMA). PMMA is a transparent plastic used to create optical fibers. DR1 has nonlinear properties, causing PMMA doped with DR1 (DR1-PMMA) to also have nonlinear properties, controllable by the DR1 concentration. DR1-PMMA's Lorentz characteristics will be modeled, as well as the nonlinear Kerr effect, which is the primary source of the device's

desired behavior. DR1-PMMA has been used as a waveguide in optical switching and photomechanical applications [43, 44, 45, 46, 47, 48]. This work will focus on the purely optical effects.

The nonlinear Kerr effect is a third order effect that induces an intensity-dependent change in the refractive index and creates harmonics of the fundamental. The intensity-dependent refractive index is the basis of the optical switch, while the generated harmonics both create noise and deplete energy from the beam, and thus must be mitigated through filtering and amplification. The Kerr effect can be caused by several different mechanisms, including electronic, reorientation, electrostriction, saturated absorption, and photo-thermal heating [49]. The result is an effective change in the refractive index based on the electric field intensity, making devices based on them optically bistable. The generality of the FDTD method takes into account any of these mechanisms through the constitutive equation. As such, the significance of this dissertation lies both in its generality and ability to explore ways to mitigate problems, providing guidance in the design of devices and logic circuits.

## CHAPTER 2: THE FDTD METHOD

This chapter will detail the Finite-Difference Time-Domain (FDTD) formulation used for this project. This will be divided into two sections. The first section will provide a general explanation of the FDTD method using Maxwell's equations. The second section will focus on material FDTD models, providing a general explanation of the FDTD method and the derivation of the equations used in this work without delving into a particular construction or specific material parameters.

### 2.1 MAXWELL'S EQUATIONS

This section explains the general FDTD implementation of Maxwell's equations, along with general FDTD setup and use. The method used here is based on the Yee algorithm [50], which employs the interleaved form of Maxwell's equations that is generally used in FDTD. This form, as opposed to the wave equation, provides more robust solutions, enables the simultaneous solving of both the electric and magnetic field intensities, allows boundary conditions for both fields to be enforced, and models unique features of each field [51].

#### 2.1.1 MAXWELL'S EQUATIONS IN FREE SPACE

The complete set of Maxwell's equations in differential form using SI units is [52]

$$\nabla \times \mathbf{H} = \mathbf{J}_i + \mathbf{J}_c + \frac{\partial \mathbf{D}}{\partial t} \quad (2.1a)$$

$$\nabla \times \mathbf{E} = -\mathbf{M}_i - \frac{\partial \mathbf{B}}{\partial t} \quad (2.1b)$$

$$\nabla \cdot \mathbf{D} = \rho_e \quad (2.1c)$$

$$\nabla \cdot \mathbf{B} = \rho_m, \quad (2.1d)$$

where  $\mathbf{H}$  is the magnetic field intensity,  $\mathbf{E}$  is the electric field intensity,  $\mathbf{D}$  is the electric flux density, and  $\mathbf{B}$  is the magnetic flux density. In this work, there will be no sources for the electric current density ( $\mathbf{J}_i$ ) or for the magnetic current density ( $\mathbf{M}_i$ ). To begin with, assume there is no conduction electric current density ( $\mathbf{J}_c$ ), no electric charge density ( $\rho_e$ ), and no magnetic charge density ( $\rho_m$ ). This allows

for significant simplification, resulting in

$$\nabla \times \mathbf{H} = \frac{\partial \mathbf{D}}{\partial t} \quad (2.2a)$$

$$\nabla \times \mathbf{E} = -\frac{\partial \mathbf{B}}{\partial t} \quad (2.2b)$$

$$\nabla \cdot \mathbf{D} = 0 \quad (2.2c)$$

$$\nabla \cdot \mathbf{B} = 0, \quad (2.2d)$$

in this particular situation. The constitutive relations are given by [53]

$$\mathbf{D} = \hat{\varepsilon} * \mathbf{E} \quad (2.3a)$$

$$\mathbf{B} = \hat{\mu} * \mathbf{H}, \quad (2.3b)$$

where  $\hat{\varepsilon}$  is the permittivity of the medium,  $\hat{\mu}$  is the permeability of the medium and  $*$  indicates convolution. Although  $\hat{\varepsilon}$  and  $\hat{\mu}$  are most generally defined in tensor form, in this work the media are isotropic and not a function of the direction of the applied field. The convolution of Eqs. (2.3) can be simplified for free space to simple multiplication, with the permittivity replaced with that of free space ( $\varepsilon_0 = 8.854 \times 10^{-12} F/m$ ) and the permeability replaced with that of free space ( $\mu_0 = 4\pi \times 10^{-7} H/m$ ).

Now substituting in Eqs. (2.3) into Eq. (2.2a) and Eq. (2.2b) allows the time-dependent Maxwell's curl equations in free space to be rewritten as

$$\nabla \times \mathbf{H} = \varepsilon_0 \frac{\partial \mathbf{E}}{\partial t} \quad (2.4a)$$

$$\nabla \times \mathbf{E} = -\mu_0 \frac{\partial \mathbf{H}}{\partial t}, \quad (2.4b)$$

which can be rearranged to [54]

$$\frac{\partial \mathbf{E}}{\partial t} = \frac{1}{\varepsilon_0} \nabla \times \mathbf{H} \quad (2.5a)$$

$$\frac{\partial \mathbf{H}}{\partial t} = -\frac{1}{\mu_0} \nabla \times \mathbf{E} \quad (2.5b)$$

in order to place time derivatives on the left side of the equation. The  $\mathbf{E}$  and  $\mathbf{H}$  fields are all in three dimensions. Because the permittivity and permeability are on such different scales in Eqs. (2.5), it is more convenient to normalize the units using the ratio of the permittivity to permeability [54]. This is achieved by substituting

$$\tilde{\mathbf{E}} = \sqrt{\frac{\varepsilon_0}{\mu_0}} \mathbf{E}, \quad (2.6)$$



which results in Eqs. (2.5) being written as

$$\frac{\partial \tilde{\mathbf{E}}}{\partial t} = \frac{1}{\sqrt{\epsilon_0 \mu_0}} \nabla \times \mathbf{H} \quad (2.7a)$$

$$\frac{\partial \mathbf{H}}{\partial t} = -\frac{1}{\sqrt{\epsilon_0 \mu_0}} \nabla \times \tilde{\mathbf{E}}. \quad (2.7b)$$

The speed of light in free space ( $c_0$ ) is related to the permittivity and permeability as

$$c_0 = \frac{1}{\sqrt{\epsilon_0 \mu_0}} \quad (2.8)$$

allowing Eqs. (2.7) to be written as

$$\frac{\partial \tilde{\mathbf{E}}}{\partial t} = c_0 \nabla \times \mathbf{H} \quad (2.9a)$$

$$\frac{\partial \mathbf{H}}{\partial t} = -c_0 \nabla \times \tilde{\mathbf{E}}. \quad (2.9b)$$

This form is the same as Maxwell's equations in Gaussian units [49]. Going forward, Gaussian units will be used. The electric field will be denoted as  $\mathbf{E}$ , dropping the  $\tilde{\mathbf{E}}$  notation.

### 2.1.2 ONE-DIMENSIONAL FDTD FORMULATION IN FREE SPACE

Maxwell's equations in Eqs. (2.9) use  $\mathbf{E}$  and  $\mathbf{H}$  fields defined in 3-dimensional space, as well as time, meaning each field has a value at each point in space at a particular time. The FDTD method typically utilizes the Yee cell to define the physical location, breaking up space into individual cubes [50, 51, 54]. This utilizes a model in which the  $\mathbf{E}$  and  $\mathbf{H}$  fields are physically offset by half a unit cell in each direction. Each directional  $\mathbf{E}$  field location is surrounded in one plane by four  $\mathbf{H}$  field components, and each directional  $\mathbf{H}$  field location is surrounded in one plane by four  $\mathbf{E}$  field components. The version of the Yee cell used in this work is shown in Fig. 2.1. The green dashed line shows the one-dimensional simulation direction used in this work. This can be referred to as an x-directed, y-polarized TEM wave and only utilizes  $E_y$  and  $H_z$  [51].

The one-dimensional equivalents of Eqs. (2.9) in the chosen single dimension are

$$\frac{\partial E_y(x, t)}{\partial t} = -c_0 \frac{\partial H_z(x, t)}{\partial x} \quad (2.10a)$$

$$\frac{\partial H_z(x, t)}{\partial t} = -c_0 \frac{\partial E_y(x, t)}{\partial x}. \quad (2.10b)$$

Note the simplification on the right side of the equation is possible because the single dimension being used for the traveling wave is in the x-direction, and the only relevant terms will be partial derivatives

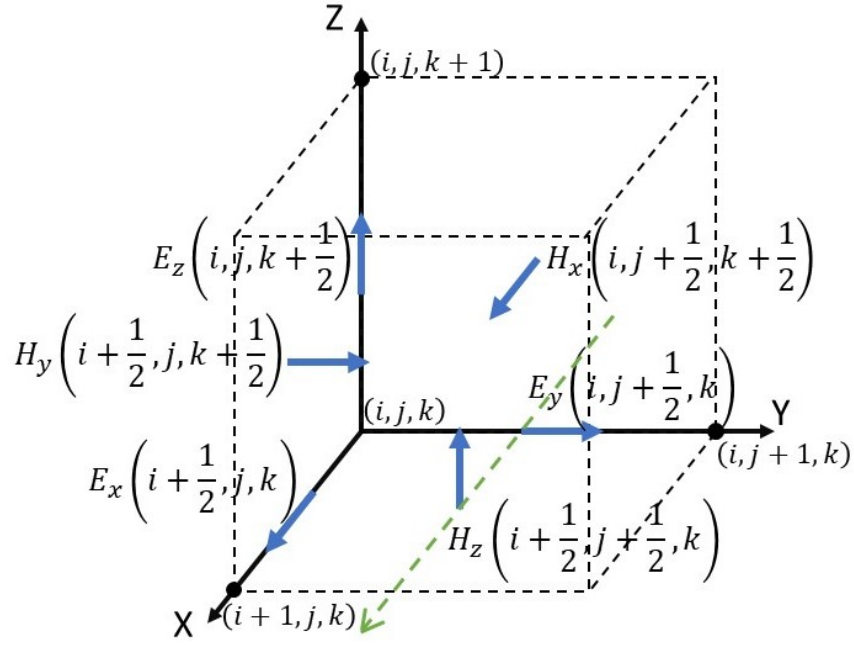


Figure 2.1: Yee cell used in this work. The green dashed line shows the simulation propagation direction being used.

in the x-direction. To approximate the time derivative in the FDTD method, there are several possible approaches. The approximation is necessary because the simulation discretizes time and space. The first derivative is defined as

$$\frac{\partial F(t)}{\partial t} = \lim_{\Delta t \rightarrow 0} \frac{F(t + \Delta t) - F(t)}{\Delta t}. \quad (2.11)$$

In this work,  $n$  represents an integer number of time steps. The first derivative is then simply approximated as

$$\frac{\partial F(t)}{\partial t} \cong \frac{F((n+1) \cdot \Delta t) - F(n \cdot \Delta t)}{\Delta t} \quad (2.12)$$

where  $\Delta t$  is the amount of time each time step represents. Time is defined as  $t = n \cdot \Delta t$ . Substituting the first derivative with respect to time approximation of Eq. (2.12) into Eqs. (2.10) results in

$$\frac{E_y(x, (n+1) \cdot \Delta t) - E_y(x, n \cdot \Delta t)}{\Delta t} = -c_0 \frac{\partial H_z(x, n \cdot \Delta t)}{\partial x} \quad (2.13a)$$

$$\frac{H_z(x, (n+1) \cdot \Delta t) - H_z(x, n \cdot \Delta t)}{\Delta t} = -c_0 \frac{\partial E_y(x, n \cdot \Delta t)}{\partial x}. \quad (2.13b)$$

All fields are real. The time step,  $n$ , will be moved to a superscript as in

$$\frac{E_y^{n+1}(x) - E_y^n(x)}{\Delta t} = -c_0 \frac{\partial H_z^n(x)}{\partial x} \quad (2.14a)$$

$$\frac{H_z^{n+1}(x) - H_z^n(x)}{\Delta t} = -c_0 \frac{\partial E_y^n(x)}{\partial x} \quad (2.14b)$$

to create a more concise notation. This notation drops the  $\Delta t$  in the superscripts, again for conciseness, i.e.  $E_y^{((n+1) \cdot \Delta t)}$  was replaced with  $E_y^{n+1}$ . The superscript does not indicate the fields being raised to a power. Using the derivative approximation of Eq. (2.12), but modifying it to take the partial derivatives with respect to space instead of time, allows Eqs. (2.14) to be expanded to

$$\frac{E_y^{n+1}(i) - E_y^n(i)}{\Delta t} = -c_0 \frac{H_z^n(i + \frac{1}{2}) - H_z^n(i - \frac{1}{2})}{\Delta x} \quad (2.15a)$$

$$\frac{H_z^{n+1}(i + \frac{1}{2}) - H_z^n(i + \frac{1}{2})}{\Delta t} = -c_0 \frac{E_y^n(i + 1) - E_y^n(i)}{\Delta x}, \quad (2.15b)$$

where  $i$  represents the discretized physical location of a cell. The physical locations correspond to those in Fig. 2.1, with the  $E$  and  $H$  fields offset by half a cell from each other. The length each cell represents is  $\Delta x$ . The equations can be rearranged as

$$E_y^{n+1}(i) = E_y^n(i) + \frac{c_0 \Delta t}{\Delta x} \left[ H_z^n\left(i - \frac{1}{2}\right) - H_z^n\left(i + \frac{1}{2}\right) \right] \quad (2.16a)$$

$$H_z^{n+1}\left(i + \frac{1}{2}\right) = H_z^n\left(i + \frac{1}{2}\right) + \frac{c_0 \Delta t}{\Delta x} [E_y^n(i) - E_y^n(i + 1)], \quad (2.16b)$$

allowing the fields at the next time step to be calculated based on the fields at the previous time steps. The stability factor is defined as the quantity

$$S = \frac{c_0 \Delta t}{\Delta x}, \quad (2.17)$$

which is of the same form as the Courant condition. This stability factor allows Eqs. (2.16) to be further simplified to

$$E_y^{n+1}(i) = E_y^n(i) + S \left[ H_z^n\left(i - \frac{1}{2}\right) - H_z^n\left(i + \frac{1}{2}\right) \right] \quad (2.18a)$$

$$H_z^{n+1}\left(i + \frac{1}{2}\right) = H_z^n\left(i + \frac{1}{2}\right) + S [E_y^n(i) - E_y^n(i + 1)]. \quad (2.18b)$$

For each time step, a new value of  $E_y$  will be calculated based on the current values of  $E_y$  and  $H_z$ . Next, the new value of  $H_z$  will be calculated based on the current value of  $H_z$  and the newly calculated value of  $E_y$ . One final modification is made to the time steps to demonstrate the interleaving nature of the

implementation by offsetting the  $E_y$  time step by one half, using

$$E_y^{n+\frac{1}{2}}(i) = E_y^{n-\frac{1}{2}}(i) + S \left[ H_z^n \left( i - \frac{1}{2} \right) - H_z^n \left( i + \frac{1}{2} \right) \right] \quad (2.19a)$$

$$H_z^{n+1} \left( i + \frac{1}{2} \right) = H_z^n \left( i + \frac{1}{2} \right) + S \left[ E_y^{n+\frac{1}{2}}(i) - E_y^{n+\frac{1}{2}}(i+1) \right]. \quad (2.19b)$$

This is the basic one-dimensional FDTD formulation in free space. The interleaved nature of calculating  $E_y$  and  $H_z$  has several advantages including clarity, allowing the central-difference time derivatives to be second-order accurate, and preventing spurious decay of numerical wave modes [51].

### 2.1.3 STABILITY FACTOR

The stability factor must be set such that the wave propagation speed does not exceed the speed of light, meaning that in free space the time step size is limited to

$$\Delta t \leq \frac{\Delta x}{c_0}, \quad (2.20)$$

which is  $S \leq 1$  from Eq. (2.17). Therefore, the stability parameter of Eq. (2.17) must not exceed 1. It is essential that the information does not travel over more than one cell in a time step  $\Delta t$  which would allow data to skip over cells in the array. In media other than free space, this will be affected by the properties of the material as in [54]

$$\Delta t \leq \frac{n\Delta x}{c_0}, \quad (2.21)$$

since the refractive index  $n$  reduces the speed of the traveling electromagnetic wave.

### 2.1.4 BOUNDARY CONDITIONS

FDTD simulations represent a limited amount of physical space. This means there is a boundary at the edge of the simulation space. Without any modifications to the FDTD algorithm, a wave will hit those boundaries and bounce back into the simulation space, disrupting the simulation results. This is because there will be cells at the boundary unable to be modified with the FDTD algorithm. Examining Eqs. (2.19) at the lower bound with  $i = 0$  shows

$$E_y^{n+\frac{1}{2}}(0) = E_y^{n-\frac{1}{2}}(0) + S \left[ H_z^n \left( -\frac{1}{2} \right) - H_z^n \left( \frac{1}{2} \right) \right] \quad (2.22a)$$

$$H_z^{n+1} \left( \frac{1}{2} \right) = H_z^n \left( \frac{1}{2} \right) + S \left[ E_y^{n+\frac{1}{2}}(0) - E_y^{n+\frac{1}{2}}(1) \right], \quad (2.22b)$$

meaning  $E_y$  cannot be solved for since there is no value at  $H_z^n(-\frac{1}{2})$ . If the lower bound is instead set to  $i = 1$ , Eqs. (2.19) become

$$E_y^{n+\frac{1}{2}}(1) = E_y^{n-\frac{1}{2}}(1) + S \left[ H_z^n \left( \frac{1}{2} \right) - H_z^n \left( 1\frac{1}{2} \right) \right] \quad (2.23a)$$

$$H_z^{n+1} \left( 1\frac{1}{2} \right) = H_z^n \left( 1\frac{1}{2} \right) + S \left[ E_y^{n+\frac{1}{2}}(1) - E_y^{n+\frac{1}{2}}(2) \right], \quad (2.23b)$$

which contain only valid array references. However,  $E_y$  is calculated using  $H_z^n(\frac{1}{2})$ , a cell location that is not updated with  $i = 1$  as a minimum bound. Because the cell representing  $H_z^n(\frac{1}{2})$  will not be updated and is typically initialized at zero, this represents a perfect conductor. Therefore, boundary conditions that absorb any outgoing waves must be imposed.

There are several possibilities for boundary conditions. The simplest form of a boundary condition makes use of the fact that the electromagnetic wave traveling in free space will traverse a predictable number of cells in a certain amount of time based on the stability parameter of Eq. (2.17). In free space, this means the wave will travel a distance of [54]

$$\text{distance (per time step)} = c_0 \Delta t \quad (2.24)$$

in one time step. From Eq. (2.17), the time step can be written in terms of the stability parameter, the speed of light, and the cell size, allowing Eq. (2.24) to be replaced with

$$\text{distance (per time step)} = c_0 \frac{S \Delta x}{c_0} = S \Delta x. \quad (2.25)$$

The value of  $S$  must not exceed one. If  $S = 0.5$ , that means the wave will travel the distance of one cell in two time steps. This can be seen clearly by converting *distance* in Eq. (2.25) to a distance measured in number of cells, as in

$$\text{cells (per time step)} = \frac{S \Delta x}{\Delta x} = S. \quad (2.26)$$

The reciprocal of this is the number of time steps it takes to travel the distance of one cell,  $\Delta x$ :

$$\text{time steps (per cell)} = \frac{1}{\text{cells (per time step)}} = \frac{1}{S}. \quad (2.27)$$

For a simple absorbing boundary condition, it is essential that the number of time steps in Eq. (2.27) is a whole number. The FDTD method utilizes the values of the surrounding  $E$  and  $H$  fields in the calculations. As already demonstrated when at the edge of the array, the surrounding values are not directly available. However, they can still be used by saving values at the array boundaries and using

them at a time step corresponding to when those values would have been at the desired cell. So, with  $S = 0.5$ , the value computed at the lower edge of the array  $H_z(1\frac{1}{2})$ , as shown in Eq. (2.23), will be saved at time step  $n$ . Then that value will be used at time step  $n + 2$  for the adjacent cell  $H_z(\frac{1}{2})$ . A similar procedure is used at the opposite end of the array.

There are variations in the absorbing boundary conditions from above such as the Mur boundary conditions. These utilize the same principles as the simple absorbing boundary conditions. A more complete, robust set of boundary conditions is implemented by using a Perfectly Matched Layer (PML), originally developed by Berenger [55]. The PML is able to absorb outgoing waves for higher dimensional simulations and when the edge of the simulation space is not free space. This allows a higher degree of flexibility in running simulations. The simulations in this work all contain free space at the edges of the arrays and are one-dimensional so simple absorbing boundary conditions are sufficient. However, the PML was used for maximum flexibility in experimenting with the simulations. Details regarding the PML are in Appendix C.

## 2.2 MATERIAL MODELS IN FDTD

This section describes how the FDTD method is used to model complex materials including plasma, the Lorentz effect, and the Kerr effect.

### 2.2.1 ONE-DIMENSIONAL FDTD FORMULATION IN COMPLEX MATERIALS

The FDTD implementation described will now need to be formulated to include the electric flux density. Equations (2.5) were simplified to replace the electric flux density with a simple multiplication by  $\epsilon_0$ . To include the electric flux density and return to Maxwell's equations, Eqs. (2.2) can be rewritten in the one-dimensional formulation as [56]

$$\frac{\partial D_y(x, t)}{\partial t} = -c_0 \frac{\partial H_z(x, t)}{\partial x} \quad (2.28a)$$

$$D_y(x, t) = \epsilon_r(x)E_y(x, t) + 4\pi P_L(x, t) + 4\pi P_{NL}(x, t) \quad (2.28b)$$

$$\frac{\partial H_z(x, t)}{\partial t} = -c_0 \frac{\partial E_y(x, t)}{\partial x}. \quad (2.28c)$$

This was given in Gaussian units as was previously described as in Eqs. (2.10). This breaks the  $D_y(x, t)$  contribution into three parts: a simple permittivity  $\epsilon_r(x)$ , a linear polarization  $P_L(x, t)$ , and a nonlinear polarization  $P_{NL}(x, t)$ . The individual contributions from  $P_L(x, t)$  and  $P_{NL}(x, t)$  will be discussed in future sections. This is broken up in this manner to allow the modeling of a guest-host polymer. The contribution from the host polymer, assumed to be simple and linear, will be  $\epsilon_r(x)$ . The guest molecule will be modeled with the linear polarization  $P_L(x, t)$  and the nonlinear polarization  $P_{NL}(x, t)$ . The

FDTD formulation of Eq. (2.28a) and Eq. (2.28c) is nearly identical to that previously described. The only difference is  $D_y$  is now included in Eq. (2.28a) instead of  $E_y$ . Following the same procedure as described for free space in Ch. 2.1.2 results in

$$D_y^{n+\frac{1}{2}}(i) = D_y^{n-\frac{1}{2}}(i) + S \left[ H_z^n \left( i - \frac{1}{2} \right) - H_z^n \left( i + \frac{1}{2} \right) \right] \quad (2.29a)$$

$$H_z^{n+1} \left( i + \frac{1}{2} \right) = H_z^n \left( i + \frac{1}{2} \right) + S \left[ E_y^{n+\frac{1}{2}}(i) - E_y^{n+\frac{1}{2}}(i+1) \right] \quad (2.29b)$$

instead of Eqs. (2.19). The material properties are contained in Eq. (2.28b). This means Eqs. (2.29) will not change as the material changes. When changing materials, Eq. (2.28b) must be derived. Specific derivations for various materials follow in subsequent sections.

### 2.2.2 PLASMA

For plasma, the permittivity will be frequency dependent. Equation (2.28b) can be rewritten to include only plasma in the frequency domain in one-dimension as

$$D_y(x, \omega) = \varepsilon_r(x)E_y(x, \omega) + P_p(x, \omega). \quad (2.30)$$

Equation (2.30) includes the linear component  $P_p = 4\pi P_L(x, \omega)$ , renamed to indicate plasma, and  $\varepsilon_r(x)$ .

When dealing with unmagnetized plasma, Eq. (2.30) can be replaced with [54, 57]

$$D_y(x, \omega) = \left( 1 + \frac{\omega_p^2(x)}{\omega(j\nu_c(x) - \omega)} \right) E_y(x, \omega) = \varepsilon_r^*(x, \omega)E_y(x, \omega), \quad (2.31)$$

where  $\omega_p(x)$  (rad/s) is the plasma frequency,  $j = \sqrt{-1}$ , and  $\nu_c(x)$  (rad/s) is the electron collision frequency. The parameter  $\varepsilon_r^*(x, \omega)$  is defined as

$$\varepsilon_r^*(x, \omega) = 1 + \frac{\omega_p^2(x)}{\omega(j\nu_c(x) - \omega)} \quad (2.32)$$

and does not represent a complex conjugate. The \* in the superscript is used to indicate the value may be complex.

In order to move the formulation from the frequency domain to the time domain, the Z-transform can be used. The unilateral Laplace transform is defined as

$$X(s) = \int_0^{\infty} x(t)e^{-st}dt. \quad (2.33)$$

The Z-transform, used for discrete signals and analogous to the Laplace transform for continuous func-

Table 2.1: Z-Transforms relating the frequency, sampled time, and Z domain [54].  
 $\delta(t)$  is the Dirac delta function and  $u(t)$  is the unit step function.

Time Domain	Frequency Domain	Z Domain	Sampled Time Domain
$\delta(t)$	1	$\frac{1}{\Delta t}$	$\delta[n]$
$u(t)$	$\frac{1}{j\omega}$	$\frac{1}{1-z^{-1}}$	$u[n]$
$e^{-\alpha t}u(t)$	$\frac{1}{j\omega+\alpha}$	$\frac{1}{1-e^{-\alpha\Delta t}z^{-1}}$	$e^{-\alpha n\Delta t}u[n]$
$e^{-\alpha t} \sin(\beta t)u(t)$	$\frac{\beta}{(\alpha^2+\beta^2)+j\omega 2\alpha-\omega^2}$	$\frac{e^{-\alpha\Delta t} \sin(\beta\Delta t)z^{-1}}{1-2e^{-\alpha\Delta t} \cos(\beta\Delta t)z^{-1}+e^{-2\alpha\Delta t}z^{-2}}$	$e^{-\alpha n\Delta t} \sin(\beta n\Delta t)u[n]$

tions, is described by [54]

$$X(z) = \sum_{n=0}^{\infty} x[n]z^{-n} = x[0] + x[1]z^{-1} + \dots, \quad (2.34)$$

which is the single-sided version of the Z-transform with  $z$  representing the Z-domain parameter and not a physical location in the  $z$ -direction. The first step in using the Z-transform is to use partial fraction expansion to write  $\varepsilon_r^*$  in Eq. (2.32) with simple denominators as

$$\varepsilon_r^*(x, \omega) = 1 + \frac{\omega_p^2(x)/v_c(x)}{j\omega} - \frac{\omega_p^2(x)/v_c(x)}{v_c(x) + j\omega}. \quad (2.35)$$

Note  $x$  is the physical location in the  $x$ -direction. This format allows Z-transform tables to easily be used in the conversion. Table 2.1 lists some of the Z-transforms including the relationships between the time domain, the sampled time domain, the frequency domain and the Z domain.

Using the Table 2.1 transform conversions on Eq. (2.35) results in the Z-domain equation

$$\varepsilon_r^*(x, z) = \frac{1}{\Delta t} + \frac{\omega_p^2(x)/v_c(x)}{1-z^{-1}} - \frac{\omega_p^2(x)/v_c(x)}{1-e^{-v_c(x)\Delta t}z^{-1}}. \quad (2.36)$$

Again, note the  $z$  in the above equations refers to the Z-transform and not a coordinate. The Z-transform of Eq. (2.31) is simply [54]

$$D_y(x, z) = \varepsilon_r^*(x, z)E_y(x, z)\Delta t \quad (2.37)$$

by the convolution theorem. Using  $\varepsilon_r^*$  of Eq. (2.36) in Eq. (2.37) results in

$$D_y(x, z) = \left( \frac{1}{\Delta t} + \frac{\omega_p^2(x)/v_c(x)}{1-z^{-1}} - \frac{\omega_p^2(x)/v_c(x)}{1-e^{-v_c(x)\Delta t}z^{-1}} \right) E_y(x, z)\Delta t. \quad (2.38)$$

This can be expanded and rearranged to

$$D_y(x, z) = E_y(x, z) + \frac{\omega_p^2(x)\Delta t}{v_c(x)} \left( \frac{(1-e^{-v_c(x)\Delta t})z^{-1}}{1-(1+e^{-v_c(x)\Delta t})z^{-1}+e^{-v_c(x)\Delta t}z^{-2}} \right) E_y(x, z) \quad (2.39)$$



and the second term on the right can be separated and defined as

$$S_p(x, z) = \frac{\omega_p^2(x)\Delta t}{v_c(x)} \left( \frac{1 - e^{-v_c(x)\Delta t}}{1 - (1 + e^{-v_c(x)\Delta t})z^{-1} + e^{-v_c(x)\Delta t}z^{-2}} \right) E_y(x, z), \quad (2.40)$$

noting that the  $z^{-1}$  in the numerator within the parenthesis was removed. This allows Eq. (2.39) to be rewritten with the substitution of Eq. (2.40) and, solving for  $E_y(x, z)$ , this results in

$$E_y(x, z) = D_y(x, z) - S_p(x, z)z^{-1}, \quad (2.41)$$

which is able to be directly implemented into FDTD.  $z^{-1}$  references the value saved one time step earlier. This is due to the time delay property. For a Z-transform,

$$x(n - k) \leftrightarrow z^{-k}X(z) \quad (2.42)$$

and substituting  $k = 1$  to indicate a single time step results in

$$x(n - 1) \leftrightarrow z^{-1}X(z). \quad (2.43)$$

A variable will save the value of  $S_p(x, z)$  from the previous iteration in Eq. (2.41) for use in finding  $E_y(x, z)$ , so calculating  $S_p(x, z)$  will require an additional array to be saved. Rearranging Eq. (2.40) to place  $S_p(x, z)$  at the current time step on the left side of the equation results in

$$S_p(x, z) = (1 + e^{-v_c(x)\Delta t})S_p(x, z)z^{-1} - e^{-v_c(x)\Delta t}S_p(x, z)z^{-2} + \frac{\omega_p^2(x)\Delta t}{v_c(x)}(1 - e^{-v_c(x)\Delta t})E_y(x, z). \quad (2.44)$$

This shows that calculating  $S_p(x, z)$  will require the  $S_p(x, z)$  value from the previous two time steps (to account for the terms with  $z^{-1}$  and  $z^{-2}$ ) as well as the current data from  $E_y(x, z)$ . As long as  $E_y(x, z)$  is calculated prior to  $S_p(x, z)$  within an FDTD algorithm, this will implement the plasma correctly. Eq. (2.41) and Eq. (2.44) can be written in the same format as Eqs. (2.29), including discretizing the x-dimension  $x$  into integer locations  $i$ , as

$$E_y^{n+\frac{1}{2}}(i) = D_y^{n+\frac{1}{2}}(i) - S_p^{n-\frac{1}{2}}(i) \quad (2.45a)$$

$$S_p^{n+\frac{1}{2}}(i) = (1 + e^{-v_c(i)\Delta t})S_p^{n-\frac{1}{2}}(i) - e^{-v_c(i)\Delta t}S_p^{n-\frac{3}{2}}(i) + \frac{\omega_p^2(i)\Delta t}{v_c(i)}(1 - e^{-v_c(i)\Delta t})E_y^{n+\frac{1}{2}}(i) \quad (2.45b)$$

to describe the FDTD implementation explicitly.

### 2.2.3 KERR EFFECT

The nonlinear Kerr effect can be included in a simulation by including  $\varepsilon_r$  and the nonlinear component of Eq. (2.28b) as

$$D_y(x, t) = \varepsilon_r(x)E_y(x, t) + 4\pi P_{NL}(x, t). \quad (2.46)$$

The linear polarization term  $P_L(x, t)$  is not included in Eq. (2.46). The nonlinear polarization  $P_{NL}(x, t)$  is given by [58]

$$P_{NL}(x, t) = \chi^{(3)}(x)E_y^3(x, t), \quad (2.47)$$

where the  $\chi^{(3)}(x)$  represents the nonlinear Kerr effects of a given material. This work uses the local approximation for the Kerr effect, given in Eq. (2.47), to show potential applications for devices created with a Kerr material. This approximation does not necessarily capture the full scope of the device's behavior at high frequencies in the range of Terahertz. A more accurate Kerr representation will be included in future works. For the FDTD formulation given the local approximation,  $E_y(x, t)$  must be given in terms of  $D_y(x, t)$  meaning an approximation is necessary for  $E_y^3(x, t)$ . The Taylor series expansion provides one method of approximation [58]

$$\begin{aligned} E_y^3(x, t_n) &\approx E_y^3(x, t_{n-1}) + \left( \frac{d}{dt} E_y^3(x, t_{n-1}) \right) (t_n - t_{n-1}) \\ &= E_y^3(x, t_{n-1}) + 3E_y^2(x, t_{n-1}) \left( \frac{d}{dt} E_y(x, t_{n-1}) \right) (t_n - t_{n-1}) \\ &\approx E_y^3(x, t_{n-1}) + 3E_y^2(x, t_{n-1}) \frac{E_y(x, t_n) - E_y(x, t_{n-1})}{t_n - t_{n-1}} (t_n - t_{n-1}) \\ &= 3E_y^2(x, t_{n-1})E_y(x, t_n) - 2E_y^3(x, t_{n-1}) \end{aligned} \quad (2.48)$$

when evaluated at the point  $t = t_n$  around the point  $t_{n-1}$ . This leads to the FDTD formulation for the approximation as

$$(E_y^{n+\frac{1}{2}}(i))^3 \cong 3(E_y^{n-\frac{1}{2}}(i))^2 E_y^{n+\frac{1}{2}}(i) - 2(E_y^{n-\frac{1}{2}}(i))^3, \quad (2.49)$$

which now only requires the value of  $E_y^{n+\frac{1}{2}}(i)$ ,  $E_y$  at the current time step, in one term. This allows the substitution of the approximation in Eq. (2.49) to be used in Eq. (2.47) giving

$$P_{NL}^{n+\frac{1}{2}}(i) = \chi^{(3)}(i) \left[ 3(E_y^{n-\frac{1}{2}}(i))^2 E_y^{n+\frac{1}{2}}(i) - 2(E_y^{n-\frac{1}{2}}(i))^3 \right] \quad (2.50)$$

as the nonlinear Kerr polarization. Using that formulation of  $P_{NL}^n$  with Eq. (2.46) results in

$$D_y^{n+\frac{1}{2}}(i) = \varepsilon_r(i)E_y^{n+\frac{1}{2}}(i) + 4\pi\chi^{(3)}(i) \left[ 3(E_y^{n-\frac{1}{2}}(i))^2 E_y^{n+\frac{1}{2}}(i) - 2(E_y^{n-\frac{1}{2}}(i))^3 \right], \quad (2.51)$$

and rearranging to solve for  $E_y^{n+\frac{1}{2}}(i)$  results in

$$E_y^{n+\frac{1}{2}}(i) = \frac{D_y^{n+\frac{1}{2}}(i) + 8\pi\chi^{(3)}(i)(E_y^{n-\frac{1}{2}}(i))^3}{\varepsilon_r(i) + 12\pi\chi^{(3)}(i)\left(E_y^{n-\frac{1}{2}}(i)\right)^2}, \quad (2.52)$$

which is able to be directly implemented in FDTD. An alternate Kerr formulation is described in Appendix A and compared to the method described here.

#### 2.2.4 LORENTZ FORMULATION

There are a few possibilities for deriving the Lorentz formulation in FDTD. The Z-transform is one possible method [58]. Equation (2.28b) can be rewritten to exclude the nonlinear polarization as

$$D_y(x, t) = \varepsilon_r(x)E_y(x, t) + 4\pi P_L(x, t), \quad (2.53)$$

where  $P_L(x, t)$  is the linear polarization. The linear polarization can be described as a convolution

$$P_L(x, t) = \int_0^t \chi^{(1)}(x, t - \tau)E_y(x, \tau) d\tau. \quad (2.54)$$

The susceptibility function,  $\chi^{(1)}(x, t)$ , is a Lorentz function and can be described as [49, 54, 58]

$$\chi^{(1)}(x, \omega) = \frac{1}{4\pi} \left( \frac{\varepsilon_1(x)}{1 + j2\delta_0(x) \left( \frac{\omega}{\omega_0(x)} \right) - \left( \frac{\omega}{\omega_0(x)} \right)^2} \right) \quad (2.55)$$

in the frequency domain where  $\omega_0$  (rad/s) is the natural frequency and  $\delta_0$  is the damping constant. Similar to the FDTD formulation of the plasma, the Z-transform will be used to formulate the Lorentz FDTD implementation. The linear susceptibility will be rearranged to

$$\chi^{(1)}(x, \omega) = \frac{1}{4\pi} \left( \frac{\omega_0^2(x)\varepsilon_1(x)}{\omega_0^2(x) + j2\delta_0(x)\omega_0(x)\omega - \omega^2} \right). \quad (2.56)$$

Then, setting  $\omega_p^2(x) = \omega_0^2(x)\varepsilon_1(x)$  to write it in terms of the plasma frequency and setting  $\gamma(x) = 2\delta_0(x)\omega_0(x)$  for simplicity, results in

$$\chi^{(1)}(x, \omega) = \frac{1}{4\pi} \left( \frac{\omega_p^2(x)}{\omega_0^2(x) + j\gamma(x)\omega - \omega^2} \right). \quad (2.57)$$

The linear polarization of Eq. (2.57) resembles the final entry in Table 2.1. The following are then set to convert Eq. (2.57) to the same format as the final entry in Table 2.1:

$$\gamma(x) = 2\alpha(x) \quad (2.58a)$$

$$\omega_0(x) = \sqrt{\beta^2(x) + \left(\frac{\gamma(x)}{2}\right)^2} = \sqrt{\beta^2(x) + \alpha^2(x)}. \quad (2.58b)$$

Making the substitutions of Eqs. (2.58) into Eq. (2.57) results in

$$\chi^{(1)}(x, \omega) = \frac{\omega_p^2(x)}{4\pi\beta(x)} \left( \frac{\beta(x)}{\beta^2(x) + \alpha^2(x) + j2\alpha(x)\omega - \omega^2} \right), \quad (2.59)$$

in which the term in parenthesis is in the exact same format as in Table 2.1. Using the Z-transform from the last entry of Table 2.1 on Eq. (2.59) results in

$$\chi^{(1)}(x, z) = \frac{\omega_p^2(x)}{4\pi\beta(x)} \left( \frac{e^{-\alpha(x)\Delta t} \sin(\beta(x)\Delta t) z^{-1}}{1 - 2e^{-\alpha(x)\Delta t} \cos(\beta(x)\Delta t) z^{-1} + e^{-2\alpha(x)\Delta t} z^{-2}} \right). \quad (2.60)$$

Remembering that the convolution of Eq. (2.54) will be a multiplication in the Z-domain domain, Eq. (2.54) can be rewritten as

$$P_L(x, z) = \chi^{(1)}(x, z) E_y(x, z) \Delta t \quad (2.61)$$

in the Z-domain, similar to Eq. (2.37). Again,  $x$  refers to the location in the x-direction and  $z$  refers to the Z-Domain parameter. Finally, Eq. (2.60) can be used with Eq. (2.61) and plugged into the Z-domain version of Eq. (2.53) resulting in [56, 59]

$$P_L(x, z) = \frac{1}{4\pi} \frac{\omega_p^2(x)}{\beta(x)} \left( \frac{e^{-\alpha(x)\Delta t} \sin(\beta(x)\Delta t) z^{-1}}{1 - 2e^{-\alpha(x)\Delta t} \cos(\beta(x)\Delta t) z^{-1} + e^{-2\alpha(x)\Delta t} z^{-2}} \right) E_y(x, z) \Delta t. \quad (2.62)$$

In a manner similar to how the plasma was handled, various variables will be pulled out of Eq. (2.62) to simplify the expression. Setting

$$\gamma_1(x) = \frac{\omega_p^2(x)}{\beta(x)} \quad (2.63a)$$

$$c_1(x) = 2e^{-\alpha(x)\Delta t} \cos(\beta(x)\Delta t) \quad (2.63b)$$

$$c_2(x) = e^{-2\alpha(x)\Delta t} \quad (2.63c)$$

$$c_3(x) = \gamma_1(x) \Delta t e^{-\alpha(x)\Delta t} \sin(\beta(x)\Delta t) \quad (2.63d)$$

and substituting those values into Eq. (2.62) results in

$$P_L(x, z) = \frac{1}{4\pi} \left( \frac{c_3(x)z^{-1}}{1 - c_1(x)z^{-1} + c_2(x)z^{-2}} \right) E_y(x, z). \quad (2.64)$$

If a new variable is defined as

$$S_L(x, z) = \frac{c_3(x)}{1 - c_1(x)z^{-1} + c_2(x)z^{-2}} E_y(x, z), \quad (2.65)$$

then Eq. (2.64) can be rewritten as

$$P_L(x, z) = \frac{1}{4\pi} S_L(x, z) z^{-1}. \quad (2.66)$$

Next Eq. (2.65) can be rearranged to find  $S_L(x, z)$  at the current time step [56]

$$S_L(x, z) = c_1(x)z^{-1}S_L(x, z) - c_2(x)z^{-2}S_L(x, z) + c_3(x)E_y(x, z), \quad (2.67)$$

which is in terms of  $E_y(x, z)$  at the current time step and  $S_L(x, z)$  at previous time steps. Then Eq. (2.66) and Eq. (2.67) can be discretized and written in terms of time steps in the same way the plasma formulation was done in Ch. 2.2.2;  $z^{-1}$  refers to one time step in the past and  $z^{-2}$  refers to two time steps in the past. This means Eq. (2.66) and Eq. (2.67) become

$$P_L^{n+\frac{1}{2}}(i) = \frac{1}{4\pi} S_L^{n-\frac{1}{2}}(i) \quad (2.68a)$$

$$S_L^{n+\frac{1}{2}}(i) = c_1(i)S_L^{n-\frac{1}{2}}(i) - c_2(i)S_L^{n-\frac{3}{2}}(i) + c_3(i)E_y^{n+\frac{1}{2}}(i). \quad (2.68b)$$

The discretized version of Eq. (2.53) is

$$D_y^{n+\frac{1}{2}}(i) = \varepsilon_r(i)E_y^{n+\frac{1}{2}}(i) + 4\pi P_L^{n+\frac{1}{2}}(i). \quad (2.69)$$

Finally, rearranging Eq. (2.69) to solve in terms of  $E_y(x, z)$  and substituting in Eq. (2.68a) results in

$$E_y^{n+\frac{1}{2}}(i) = \frac{D_y^{n+\frac{1}{2}}(i) - S_L^{n-\frac{1}{2}}(i)}{\varepsilon_r(i)}. \quad (2.70)$$

Writing Eq. (2.70) and Eq. (2.68b) together gives

$$E_y^{n+\frac{1}{2}}(i) = \frac{D_y^{n+\frac{1}{2}}(i) - S_L^{n-\frac{1}{2}}(i)}{\varepsilon_r(i)} \quad (2.71a)$$

$$S_L^{n+\frac{1}{2}}(i) = c_1(i)S_L^{n-\frac{1}{2}}(i) - c_2(i)S_L^{n-\frac{3}{2}}(i) + c_3(i)E_y^{n+\frac{1}{2}}(i), \quad (2.71b)$$

which can be implemented between Eq. (2.29a) and Eq. (2.29b). An alternate method of developing the FDTD implementation for Lorentz materials is described in Appendix B. A comparison of the two methods is also given.

### 2.2.5 LORENTZ AND KERR COMBINED FORMULATION

Now that the plasma, Lorentz, and Kerr components of the FDTD simulation have been derived, the components can be combined for a full, complex formulation. This is still done with purely the electric flux density of Eq. (2.28b). The polarizations were defined in the previous sections. Converting Eq. (2.28b) to FDTD notation results in

$$D_y^{n+\frac{1}{2}}(i) = \varepsilon_r(i)E_y^{n+\frac{1}{2}}(i) + 4\pi P_{NL}^{n+\frac{1}{2}}(i) + 4\pi P_L^{n+\frac{1}{2}}(i) \quad (2.72)$$

using the same methods used throughout this chapter. It was shown in Eq. (2.50) that

$$P_{NL}^{n+\frac{1}{2}}(i) = \chi^{(3)}(i) \left( 3 \left( E_y^{n-\frac{1}{2}}(i) \right)^2 E_y^{n+\frac{1}{2}}(i) - 2 \left( E_y^{n-\frac{1}{2}}(i) \right)^3 \right) \quad (2.73)$$

and in Eq. (2.68a) that

$$P_L^{n+\frac{1}{2}}(i) = \frac{1}{4\pi} S_L^{n-\frac{1}{2}}(i). \quad (2.74)$$

Combining Eq. (2.73) and Eq. (2.74) with Eq. (2.72) results in

$$D_y^{n+\frac{1}{2}}(i) = \varepsilon_r(i)E_y^{n+\frac{1}{2}}(i) + 4\pi\chi^{(3)}(i) \left( 3 \left( E_y^{n-\frac{1}{2}}(i) \right)^2 E_y^{n+\frac{1}{2}}(i) - 2 \left( E_y^{n-\frac{1}{2}}(i) \right)^3 \right) + S_L^{n-\frac{1}{2}}(i). \quad (2.75)$$

Rearranging Eq. (2.75) to solve for  $E_y^{n+\frac{1}{2}}(i)$  results in

$$E_y^{n+\frac{1}{2}}(i) = \frac{D_y^{n+\frac{1}{2}}(i) + 8\pi\chi^{(3)}(i) \left( E_y^{n-\frac{1}{2}}(i) \right)^3 - S_L^{n-\frac{1}{2}}(i)}{\varepsilon_r(i) + 12\pi\chi^{(3)}(i) \left( E_y^{n-\frac{1}{2}}(i) \right)^2}, \quad (2.76)$$

given  $S_L$  updating with Eq. (2.71b) as before. Comparing Eq. (2.76) to Eq. (2.71a) shows the additional terms related to Kerr effect included in a similar manner to that shown in Eq. (2.52). If the coefficients of Eqs. (2.63) are set to zero, the Lorentz term will fall out of Eq. (2.76). Similarly, if  $\chi^{(3)}(i)$  is set to

zero, the material will not have any Kerr effects.

### 2.2.6 PLASMA, LORENTZ, AND KERR FORMULATION

The combined plasma formulation of Eq. (2.45a) with a Kerr/Lorentz material adjusts Eq. (2.76) to

$$E_y^{n+\frac{1}{2}}(i) = \frac{D_y^{n+\frac{1}{2}}(i) - S_P^{n-\frac{1}{2}}(i) + 8\pi\chi^{(3)}(i) \left(E_y^{n-\frac{1}{2}}(i)\right)^3 - S_L^{n-\frac{1}{2}}(i)}{\varepsilon_r(i) + 12\pi\chi^{(3)}(i) \left(E_y^{n-\frac{1}{2}}(i)\right)^2} \quad (2.77)$$

with Eq. (2.45b) used to calculate  $S_P^{n+\frac{1}{2}}(i)$ . Note that only the plasma or the Kerr/Lorentz effects will occur on a particular cell; the other effect will be set to zero using the various associated constants.

# CHAPTER 3: FABRY-PEROT DEVICE IN FDTD SIMULATION

This chapter will explore a Fabry-Perot device using the FDTD formulation developed in Ch. 2. Specific parameters will be chosen, and the corresponding characteristics of this device will be investigated. All simulations were coded in Python throughout this work.

## 3.1 INPUT

The input used in this project will generally be a sinusoidal signal within an envelope. The envelope will include a gradual rise followed by plateauing for a certain amount of time, followed by a gradual decline that mirrors the rise. The envelope has a similar profile to a Hanning window with a plateau region, but the function used here is [60]

$$f(x) = \frac{a}{\pi} \sin\left(\frac{\pi}{2a}\right) \left( \frac{1}{1 + (x - x_c)^{2a}} \right), \quad (3.1)$$

where  $a$  is a constant controlling the width of the plateau region and  $x_c$  is the center of the pulse.

Equation (3.1) can be compared to a normal Hanning window with a central plateau region of the form

$$f(x) = \frac{1}{2} \left( 1 - \cos\left(\frac{2\pi x}{(N - n_{plateau})}\right) \right), \quad x < x_c - \frac{n_{plateau}}{2}, \quad (3.2a)$$

$$f(x) = 1, \quad x_c - \frac{n_{plateau}}{2} \leq x < x_c + \frac{n_{plateau}}{2}, \quad (3.2b)$$

$$f(x) = \frac{1}{2} \left( 1 - \cos\left(\frac{2\pi(x - n_{plateau})}{(N - n_{plateau})}\right) \right), \quad x_c + \frac{n_{plateau}}{2} \leq x, \quad (3.2c)$$

where  $n_{plateau}$  is the width of the plateau, and  $N$  is the total length of the function. The advantage of using the envelope described in Eq. (3.1) is that the first and second derivatives are smooth, continuous functions, as shown in Fig. 3.1. This plateau function is normalized by dividing  $f(x)$  by the maximum value of  $f(x)$ , which occurs at  $x_c$ .



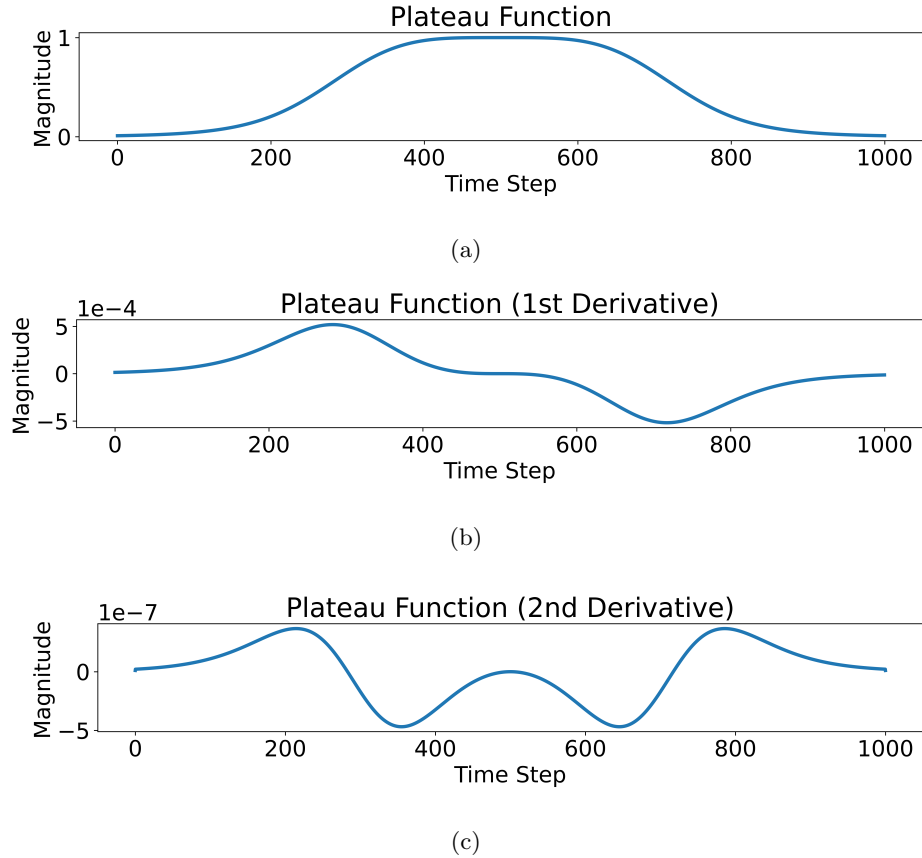


Figure 3.1: Plateau function of Eq. (3.1) with  $a = 4$  showing (a) the function itself, (b) the function's first derivative, and (c) the function's second derivative. There are no discontinuities.

If a Hanning window with a plateau region of the form described in Eq. (3.2) is used instead, the first derivative will be continuous but not smooth. There are discontinuities in the second derivative, as shown in Fig. 3.2. Therefore, unless otherwise specified, the envelope used in this work will be of the form described in Eq. (3.1).

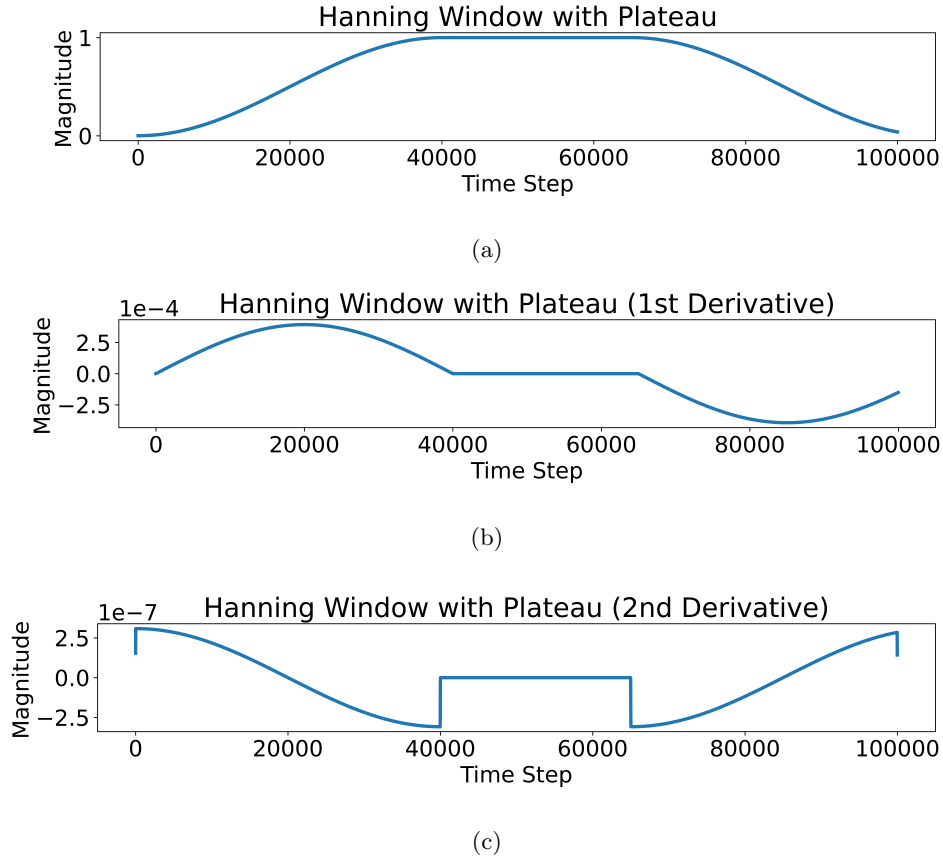


Figure 3.2: Hanning window plus plateau function of Eq. (3.2) showing (a) the function itself, (b) the function's first derivative, and (c) the function's second derivative. There are discontinuities in the second derivative. The function is normalized.

## 3.2 FREE SPACE SIMULATION

The simulation space will be 625 cells, including eight cells dedicated to the PML at each end of the space. The reasoning behind the choice of this exact number of cells will be explained in detail in subsequent sections, and the number of cells comprising the simulation space will vary in other simulations. The input, as described in the previous section, will be a sinusoidal wave with a frequency of 500 THz contained within an envelope described by Eq. (3.1). An example of the input signal contained within a relatively short envelope is shown in Fig. 3.3.

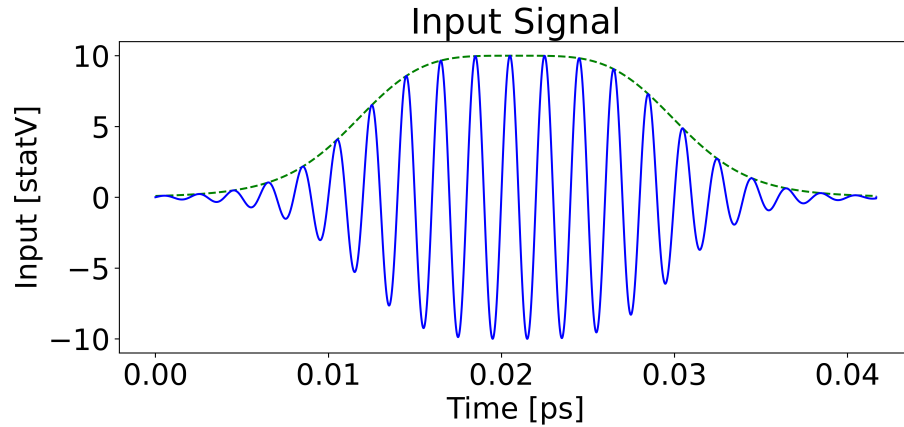


Figure 3.3: Example of a sinusoidal input contained within the envelope of Eq. (3.1). The simulations will typically use a much longer input consisting of more sinusoidal cycles.

The frequency of 500 THz determines the minimum time step size and the minimum cell size required for the simulation. The cell size was chosen to be  $\Delta x = 5.0 \times 10^{-7}$  cm, and the time step size was chosen to be  $\Delta t = 2.1 \times 10^{-18}$  s. These values correspond to a stability factor of 0.125, which was calculated using Eq. (2.17). Since this stability factor is less than 1.0, these values are valid. The motivations behind these choices are to ensure adequate resolution when simulating higher frequencies generated by the inclusion of the Kerr effect.

The input will be near the left side of the simulation space, as depicted in Fig. 3.4. This shows the eight cells on either end of the array that will be used as a PML. The remaining parameters of the simulation space will correspond to those of free space.



Figure 3.4: Simulation space of 625 cells with free space and the PML. The input travels from the origin to the right.

As shown in Fig. 3.4, the input signal is generated in a single direction. This is achieved by inputting the signal using the total field/scattered field method, which is described in Appendix D. Fig. 3.5 depicts the input signal from Fig. 3.3 using a soft source, which is also described in Appendix D, at various points in time within the simulation space depicted in Fig. 3.4. The input signal propagates from left

to right and eventually dissipates at the boundary, as expected.

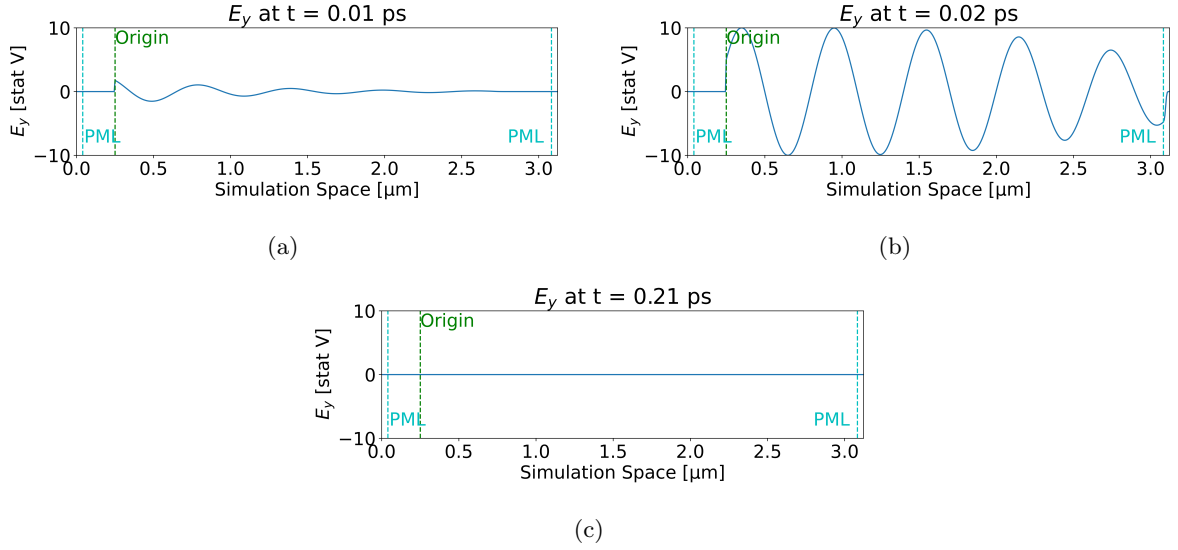


Figure 3.5: Simulation space captured at (a) 0.01 ps, (b) 0.02 ps, and (c) 0.21 ps showing the input of Fig. 3.3 moving left to right and dissipating to the right of the PML. By 0.21 ps, the signal has dissipated entirely. The input pulse is wide in (b) to demonstrate the effectiveness of the PML and shows the signal quickly decaying to zero on the right side of the figure within the PML.

### 3.3 SILVER MIRRORS

The simulation space will now include a cavity defined by two partial reflectors made from silver using the plasma formulation derived in Ch. 2.2.2. First, the plasma mirror will be examined by itself. The plasma model for silver is defined by the collision frequency  $\nu_c = 57 \times 10^{12}$  rad/s and the plasma frequency  $\omega_p = 2 \times 10^{15} \cdot 2\pi$  rad/s [54, 57]. The accuracy of this model can be compared with experimental values [61], as shown in Fig. 3.6.

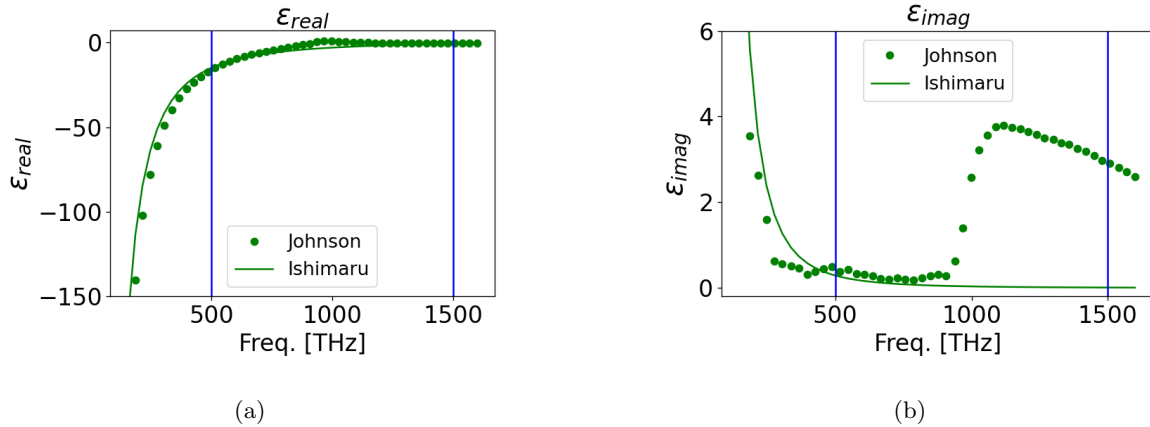


Figure 3.6: A comparison of the (a) real and (b) imaginary permittivity ( $\epsilon$ ) of silver plasma across a range of frequencies from the Ishimaru model and the experimental values from Johnson. The vertical blue lines indicate the fundamental frequency of 500 THz and the third harmonic of 1500 THz. The Ishimaru model is used in these simulations.

The simulation to verify the parameters is set up with a single pulse moving from left to right. Plasma is defined for cells at the center of the simulation space. When the pulse hits the plasma, the signal will be reflected, absorbed, transmitted or a combination of the three depending on the plasma's thickness and the frequency of the signal. Fig. 3.7 shows a 6-cell thick plasma with a 500 THz signal striking the plasma.

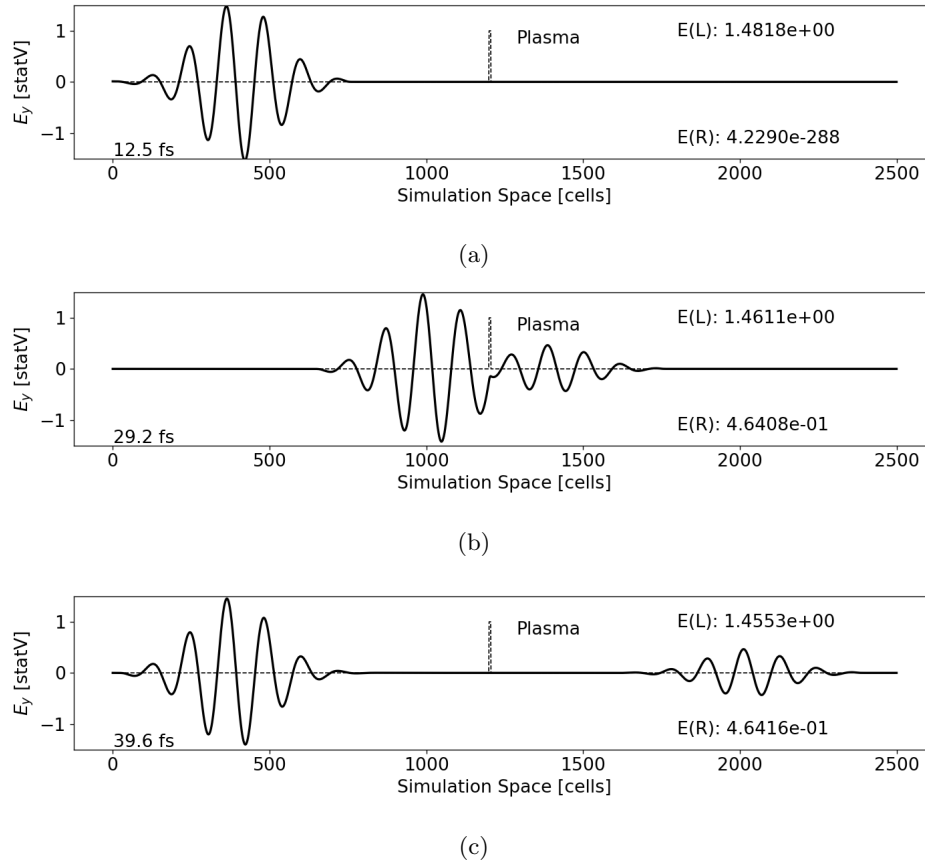


Figure 3.7: Simulation showing the progression of an electric field pulse of 500 THz interacting with a silver plasma mirror. The pulse (a) moves to the right, (b) hits the plasma mirror, which is six cells wide, splitting, and (c) moves away from the mirror. The peak electric field strengths are displayed on the right of each plot showing the peak to the left of the plasma mirror ( $E(L)$ ) and to the right of the plasma mirror ( $E(R)$ ).

The Fourier transform of the signals in Fig. 3.7 more accurately describes the reflection compared to the transmission at the fundamental frequency of 500 THz. This is shown in Fig. 3.8.

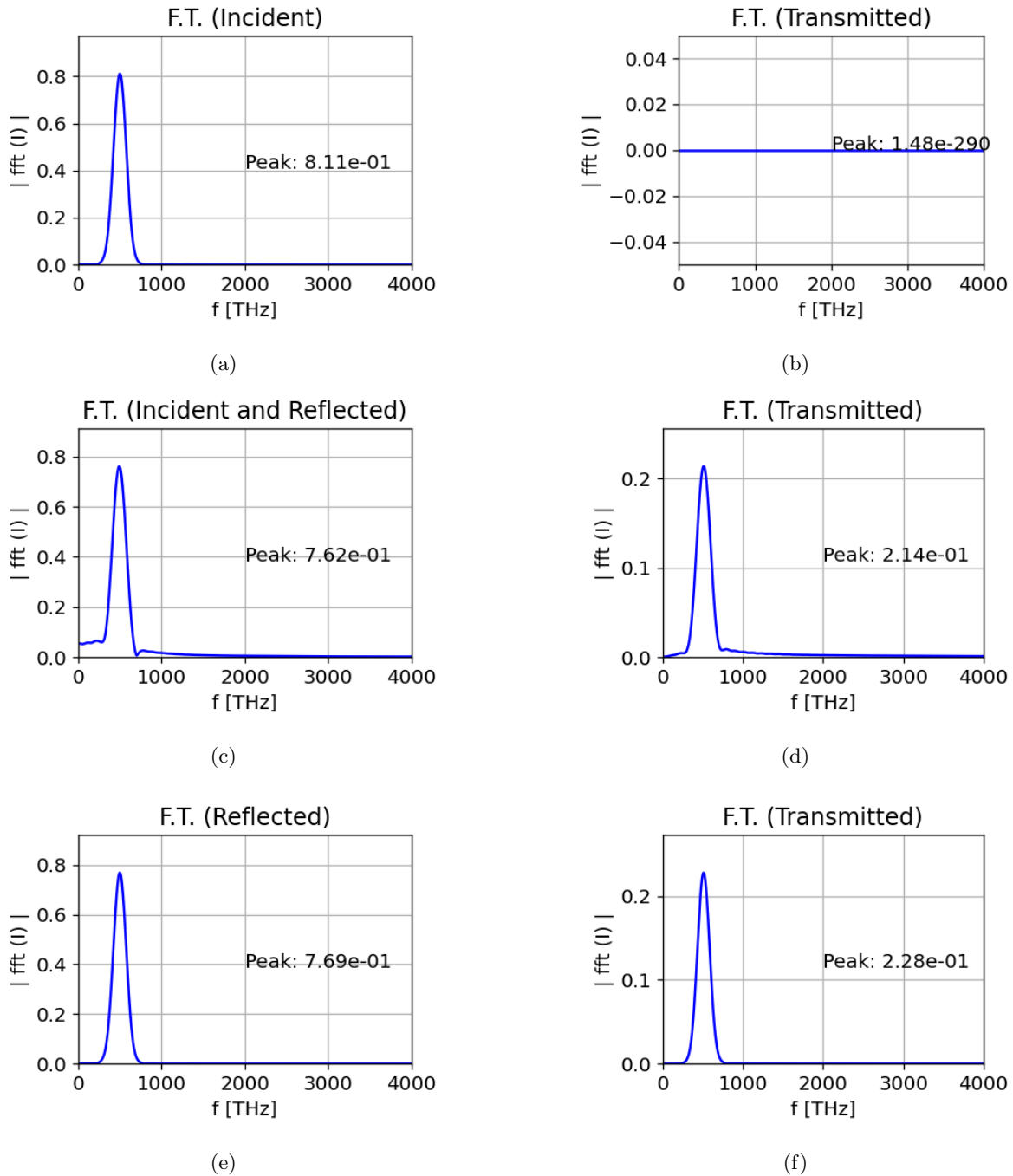


Figure 3.8: Fourier transforms of the signals corresponding to Fig. 3.7 of (a) the incident wave to the left of the plasma, (b) the initial state to the right of the plasma showing no signal, (c) the reflected signal as the incident signal is still interacting with the plasma, (d) the transmitted signal as the incident signal is still interacting with the plasma, (e) the reflected signal after the incident signal stops interacting with the plasma, and (f) the transmitted signal after the incident signal stops interacting with the plasma. The reflection is obtained by dividing the reflected value at 500 THz in (e) by the incident value at 500 THz in (a). For a 6-cell mirror, the reflection is 94.7%.

The plasma frequency, as previously stated, is 2,000 THz. If the frequency of the simulation is

increased to 10,000 THz, well above the plasma frequency, almost the entire signal is transmitted through the plasma, as expected. This is shown in Fig. 3.9.

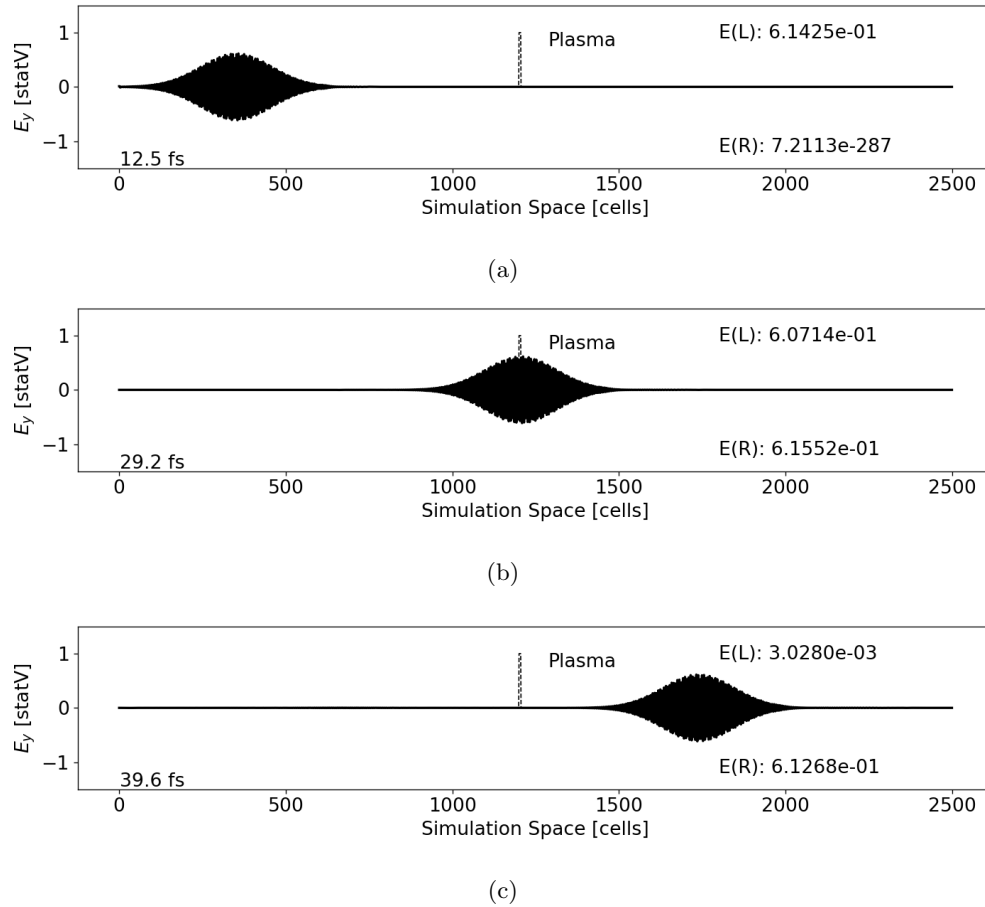


Figure 3.9: Simulation showing the progression of an electric field pulse of 10,000 THz interacting with a silver plasma mirror. The pulse (a) moves to the right, (b) hits a mirror six cells wide, and (c) moves away from the mirror. The peak electric field strengths are displayed on the right of each plot showing the peak to the left of the plasma ( $E(L)$ ) and to the right of the plasma ( $E(R)$ ). Almost the entire signal is transmitted since the signal is well above the plasma frequency.

The frequency of interest in this work is 500 THz. Looking at the reflection, as measured by the Fourier transform as described in Fig. 3.8, it is possible to vary the reflection based on the mirror thickness. A 6-cell thickness was chosen due to the high reflectivity. A comparison of mirror thickness and the corresponding reflectivity is shown in Fig. 3.10. The intensity absorption is shown in Fig. 3.11.



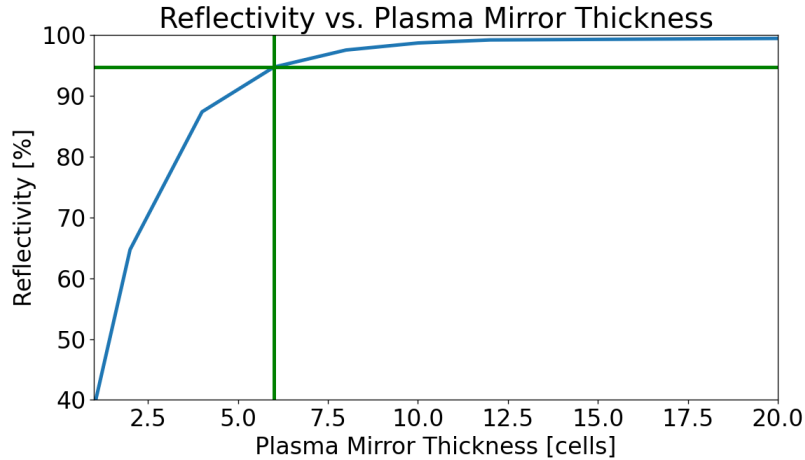


Figure 3.10: Reflectivity as a function of the plasma mirror thickness, measured in number of cells. The green vertical line is the chosen thickness of six cells, and the green horizontal line is the corresponding reflectivity (simulated in Fig. 3.7 and Fig. 3.8). A thicker plasma mirror is more reflective.

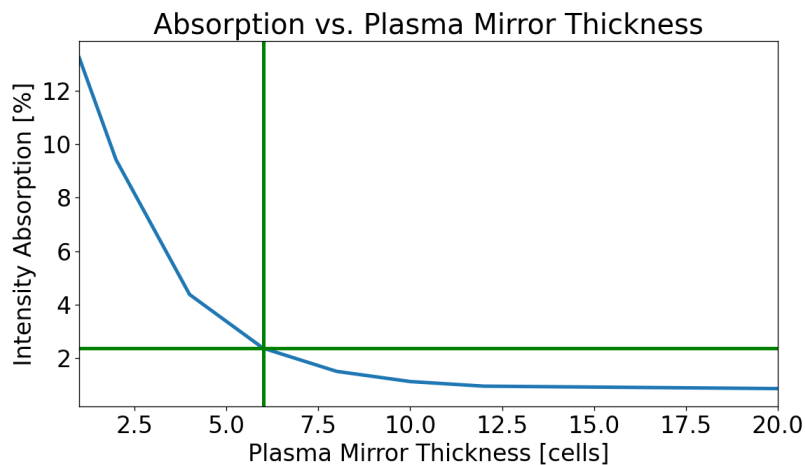


Figure 3.11: Intensity absorption as a function of the plasma mirror thickness, measured in number of cells. The green vertical line is the chosen thickness of six cells, and the green horizontal line is the corresponding absorption (simulated in Fig. 3.7 and Fig. 3.8). As expected, there is less loss with a thicker plasma mirror because there is less signal moving through the lossy plasma mirror.

### 3.4 CAVITY OF MIRRORS

Two 6-cell thick mirrors will now be used to create a cavity. An example of the simulation setup is shown in Fig. 3.12.

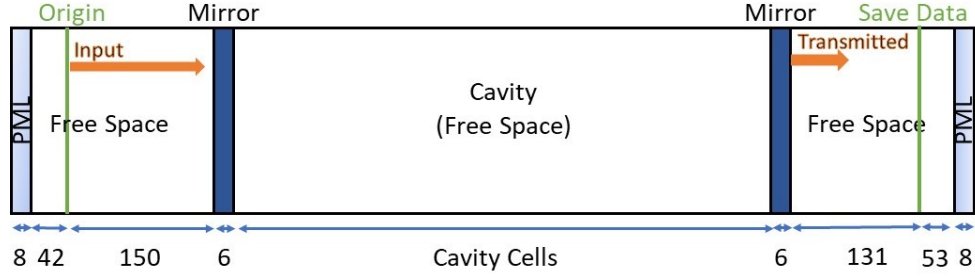


Figure 3.12: Simulation setup of two 6-cell thick mirrors used to form a cavity. The pulse moves from left to right starting at the origin. Transmitted data is saved to the right of the second mirror. Each mirror is six cells thick, and there are a varying number of cells comprising the cavity.

The intensity is calculated as

$$I = \frac{1}{T} \frac{cn}{4\pi} \int_0^T E_y(t) \times H_z(t) dt, \quad (3.3)$$

where  $c$  is the speed of light,  $n$  is the refractive index, and  $T$  is the period. In the case of transmitted signals, the intensity will be calculated at a cell to the right of the cavity. When calculating the intensity inside the cavity, the intensity is averaged over every cell of the cavity. For a 500 THz signal, one period of the waveform will span 120 cells using

$$n_{cells} = \frac{(c/f)}{\Delta x}, \quad (3.4)$$

where  $c$  is the speed of light,  $f$  is the frequency, and  $\Delta x$  is the distance each cell represents. The parameters  $f = 500$  THz and  $\Delta x = 5.0 \times 10^{-7}$  cm are chosen as before. There should be higher transmission when the free space between the mirrors corresponds to a half wavelength. The ideal cavity lengths for transmission will be slightly lower than those corresponding to integer numbers of half wavelengths due to the phase shift induced by the plasma. This can be seen in Fig. 3.13.

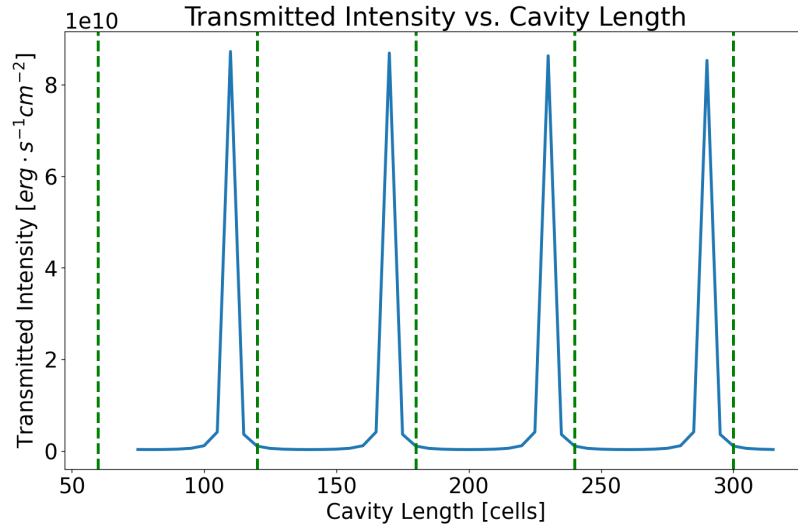


Figure 3.13: Transmitted intensity compared to the number of cavity cells. The green vertical lines correspond to half wavelengths for a 500 THz signal. Peak transmission is slightly offset from each of the lines due to the 6-cell plasma mirrors on either end of the cavity.

For a cavity length of approximately 2.5 wavelengths, the maximum transmission occurs with a cavity of 290 cells. The transmission and input over time are shown in Fig. 3.14(a) for the 290-cell cavity. The transmitted intensity is nearly the same as the input intensity in this case, with the intensity within the cavity building up significantly higher than the intensity at the input. The cavity intensity versus the input intensity and the transmitted intensity versus the input intensity are also shown in Fig. 3.14.

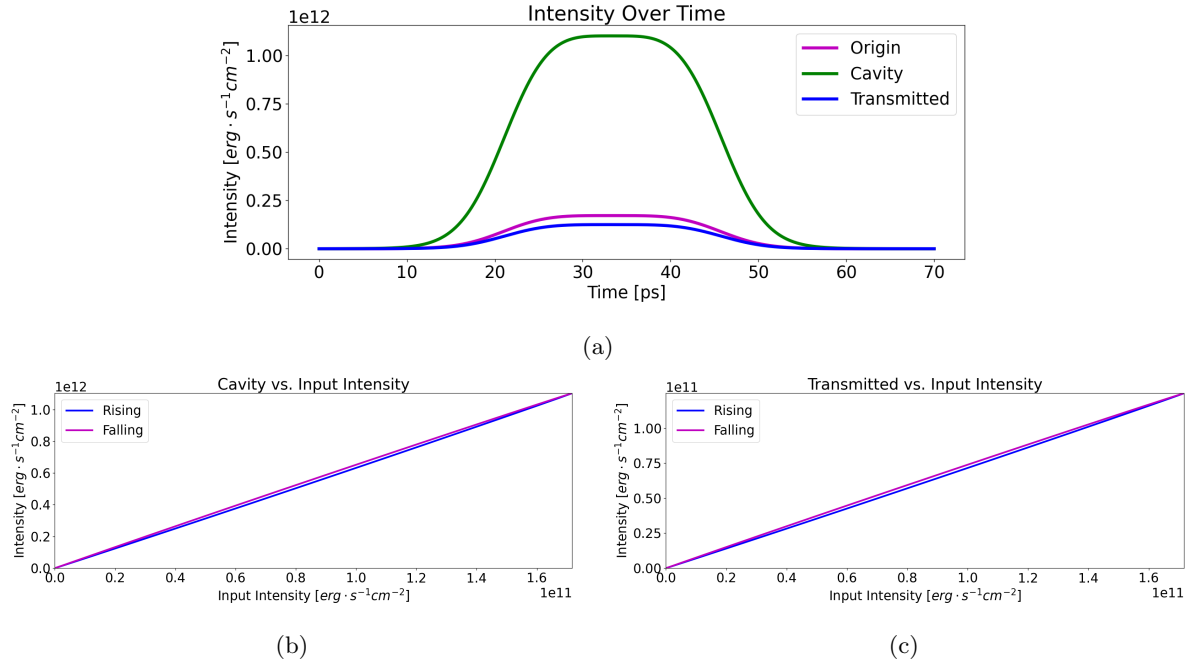


Figure 3.14: This shows the maximum transmission based on a 2.5-wavelength cavity composed of two silver mirrors. The cavity is 290 cells. (a) The intensity-over-time plot, (b) the cavity intensity versus the input intensity, and (c) the transmitted intensity versus the input intensity.

This ideal cavity length for maximum transmission was based on six mirror cells. Changing the number of mirror cells will adjust the ideal cavity length for maximum transmission as shown in Fig. 3.15. This is because some signal will interact with and be absorbed within each of the plasma mirrors. This supports the given reason that the peak transmission is not exactly what would be predicted in Fig. 3.13.

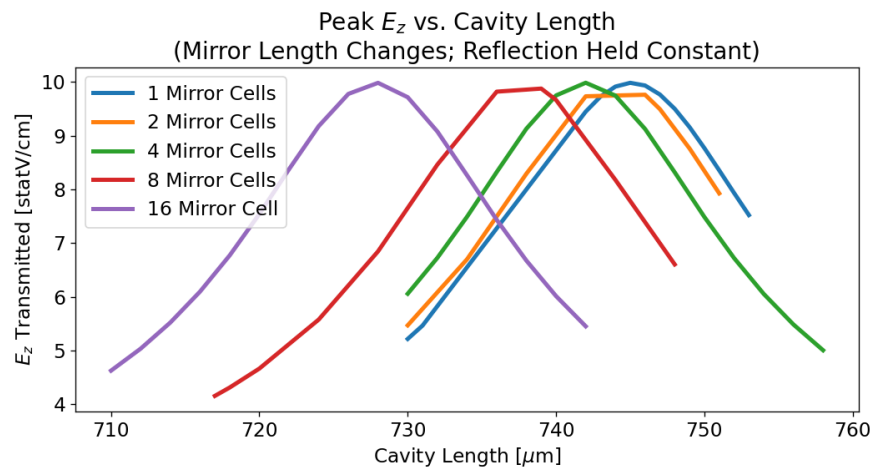


Figure 3.15: Peak  $E_z$  transmitted through the cavity versus cavity length for different mirror thicknesses while the reflection is held constant. The ideal cavity length is affected by the amount of signal absorbed in each mirror, as well as the complex interaction of the signal with the mirrors.

The cavity length corresponding to peak transmission does not change if the cell size is decreased while keeping the mirror thickness the same by increasing the number of mirror cells. However, transmission does decrease slightly pointing to the less than ideal transmission of Fig. 3.14 being caused by absorption. Figure 3.16 shows transmission in two simulations with identical reflection, mirror thickness and cavity length. The only difference is one simulation uses cells half the length of the other simulation. This means the number of cells, computational time, and memory usage double. The ideal cavity length in the two cases is identical, as expected.

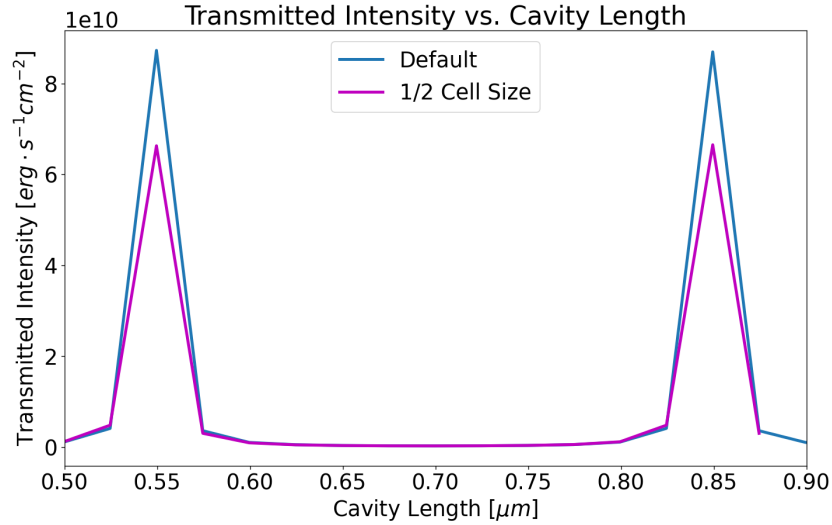


Figure 3.16: Transmission based on cavity length with the mirror thickness and reflection held constant for two different cell sizes. This shows consistency in the cavity lengths associated with peak transmission.

The analytical equation for calculating the transmitted intensity is [49]

$$I_z(\text{transmitted}) = \frac{I_z(\text{in})}{1 + \left(\frac{2r}{1-r^2}\right) \sin^2(\delta)} \quad (3.5)$$

where

$$\delta = \frac{2\pi l n}{\lambda} \quad (3.6)$$

with  $I_z$  being the incident intensity,  $r$  the reflectivity of the mirror,  $n$  the refractive index,  $l$  the cavity length, and  $\lambda$  the wavelength. This is plotted in Fig. 3.17, showing good alignment with the data.

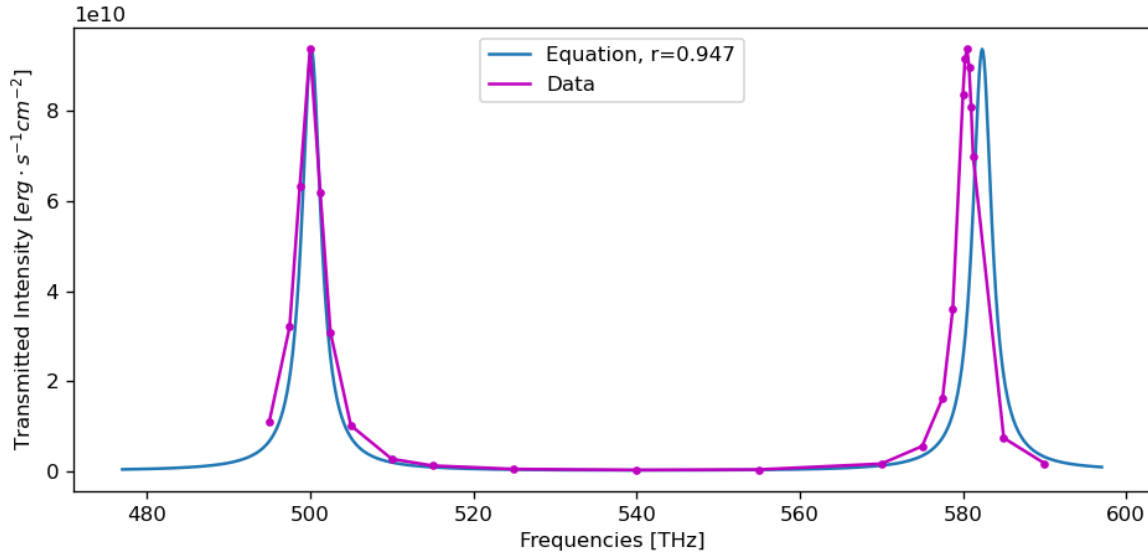


Figure 3.17: Intensity versus frequency for the FDTD simulation data and using Eq. (3.5). There is a manual adjustment to move the peak transmission of the equation to 500 THz to account for the mirrors. This shows that a constant separation of mirrors will allow peak transmission at frequencies that align generally with Eq. (3.5).

### 3.5 WAVEFORMS BETWEEN THE MIRRORS

The waveforms across the entire simulation space are shown in Fig. 3.18, in which  $E_y$  and  $H_z$  are saved at various points in time. Fig. 3.18 shows the waveforms given a cavity length of approximately 2.5 wavelengths. As expected,  $E_y$  and  $H_z$  are 90 degrees out of phase within the cavity. Each mirror is represented by two green vertical lines. The  $E_y$  signal approaches zero at each mirror surface, as expected [53]. Fig. 3.18 also shows how the two fields change over time and oscillate in magnitude. The  $E_y$  and  $H_z$  fields return to the same state after 2 fs, as expected based on the period associated with a 500 THz signal.

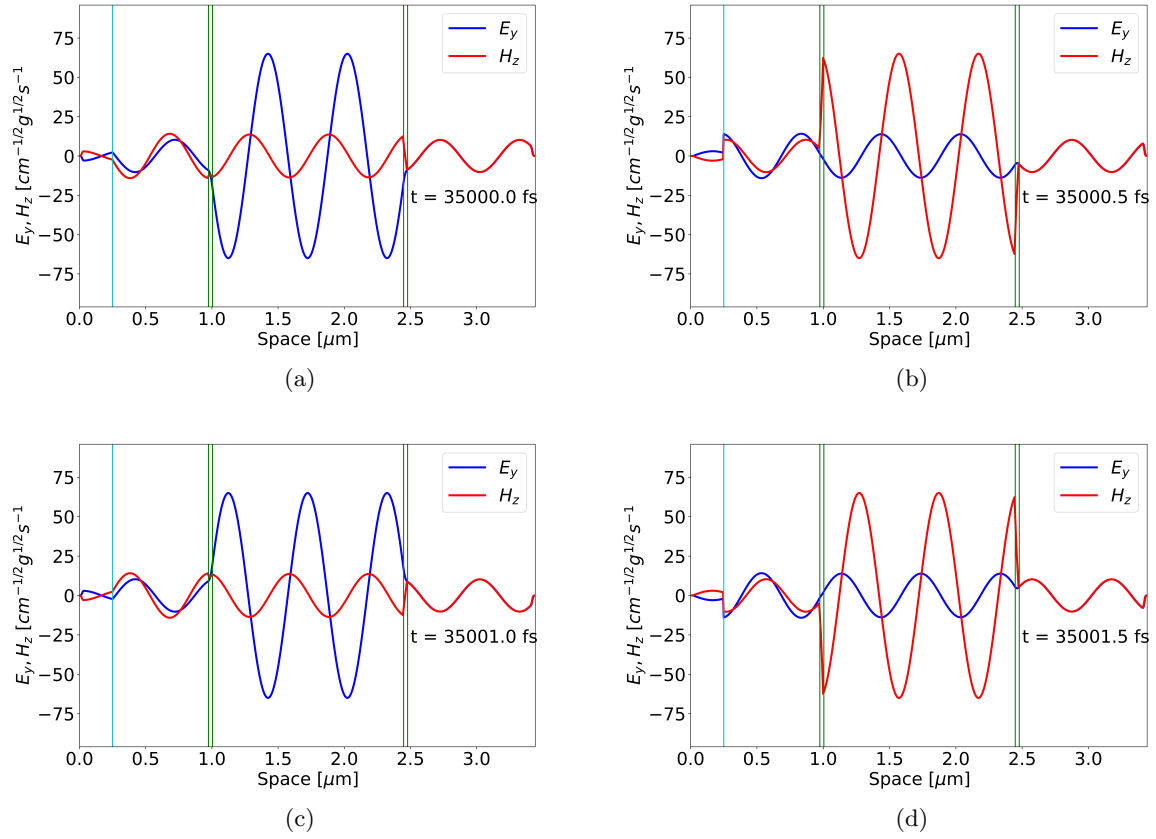


Figure 3.18: The magnitudes of  $E_y$  and  $H_z$  oscillate during the simulation. (a)-(d) capture points in time showing this oscillation within the cavity. The mirror surfaces are shown as green vertical lines. The light blue vertical line is the origin. The transmitted fields remain constant in magnitude. These snapshots occur when the input is at the maximum and held in the plateau region.

### 3.6 KERR EFFECT

The FDTD implementation of the Kerr effect was described in Ch. 2.2.3. The Kerr effect will be simulated by including it in the cavity between the mirrors as described Ch. 3.4. An example of the simulation setup is shown in Fig. 3.19.

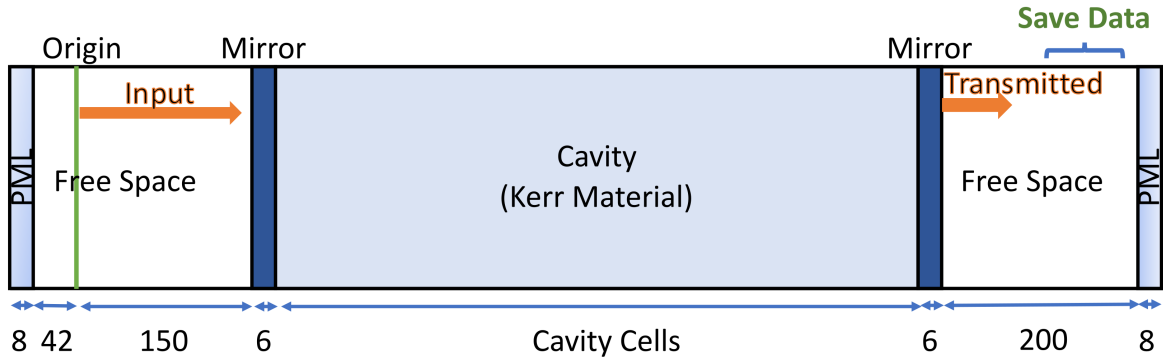


Figure 3.19: Simulation setup of two 6-cell thick mirrors used to form a cavity with a Kerr material in between the mirrors. The data moves from left to right starting at the origin. Transmitted data is saved to the right of the second mirror.

Given an input within an envelope of the shape of Fig. 3.3 and described by Eq. (3.1), the permittivity will be set to  $\epsilon_r^2 = 1.5$ , and the Kerr effect will be set at  $\chi^{(3)} = \frac{0.001 \text{ cm}^3}{4\pi \text{ erg}}$  [62, 63]. The number of cavity cells is varied in the same way as it was done in Fig. 3.13 to obtain the optimal cavity length for transmission, as shown in Fig. 3.20.

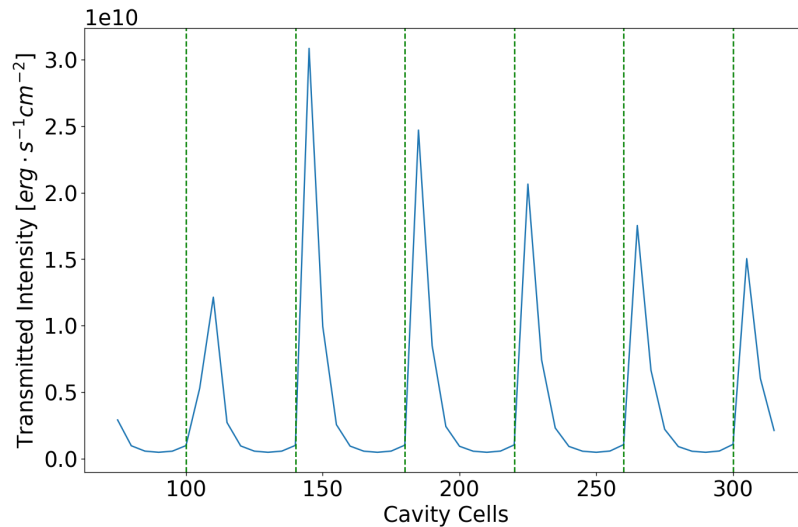


Figure 3.20: Transmitted intensity compared to the number of cavity cells of the structure of Fig. 3.19 simulating every even cavity length. The green vertical lines correspond to half wavelengths for a 500 THz signal (a cavity with a length of  $\lambda$ ,  $3\lambda/2$ ,  $2\lambda$ , etc.) in a material with a refractive index of 1.5. Peak transmission does not occur exactly at the predicted cavity lengths due to the 6-cell plasma mirrors on either end of the cavity, and because the Kerr effect will alter the effective refractive index. However, the peaks are half an integer wavelength offset from each other, as expected. The difference in peak transmission intensities is partially due to the granularity of the simulation. Some peaks show higher transmission than others since the ideal cavity length for transmission is not precisely met in this discrete system.



Because the Kerr effect is greater with a higher input intensity, the effective length of the cavity changes. Using the optimal cavity length for maximum transmission for a cavity of three wavelengths found from Fig. 3.20, which is 224 cells, the intensities over time are plotted in Fig. 3.21. The figure also shows the cavity intensity versus the input intensity and the transmitted intensity versus the input intensity. The cavity intensity is averaged over the entire cavity and then time-averaged over each period of the input 500 THz signal. The transmitted intensity is recorded at cell 50 from the right boundary and time-averaged over each period of the input 500 THz signal. Similar plots result from choosing other cavity lengths corresponding to the peaks shown in Fig. 3.20. The cavity was chosen to be approximately three wavelengths long, as opposed to a smaller number of wavelengths long, to more clearly illustrate the waveforms within the cavity in future sections.

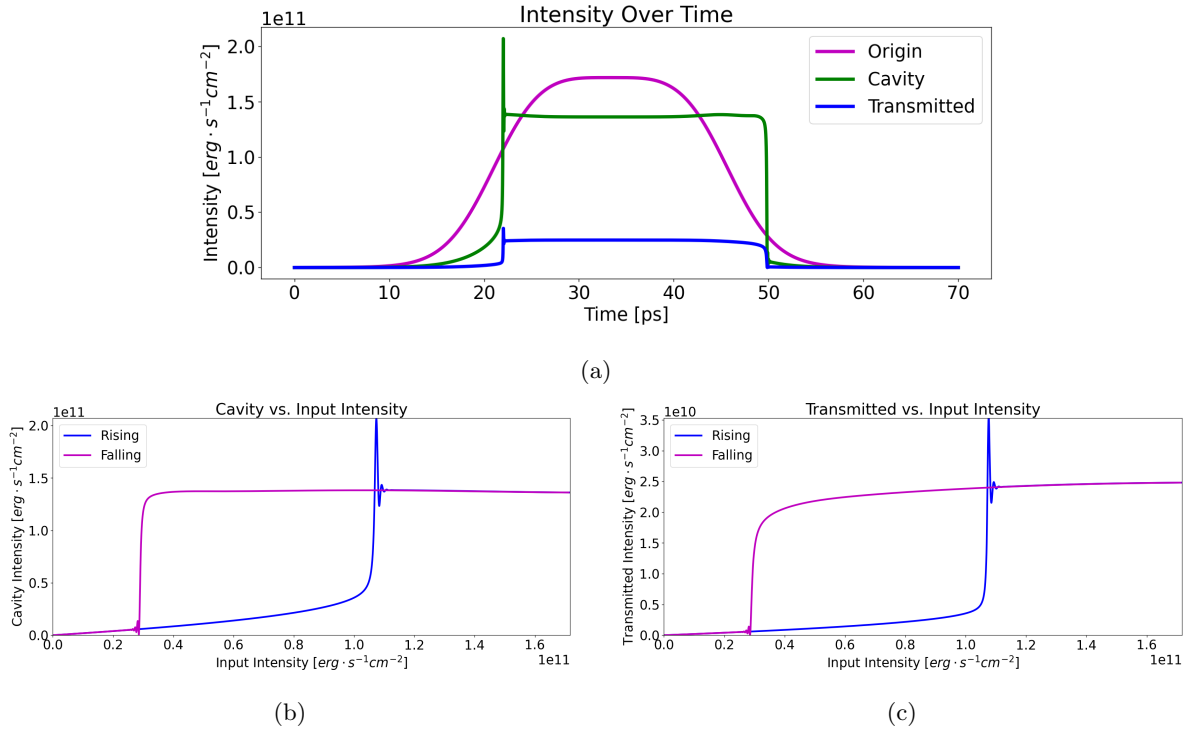
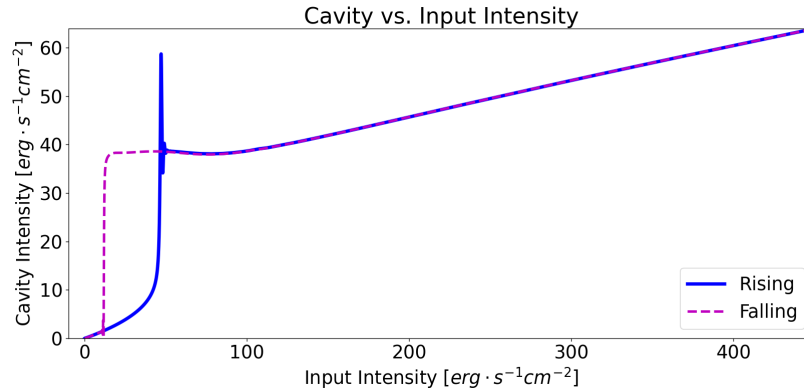


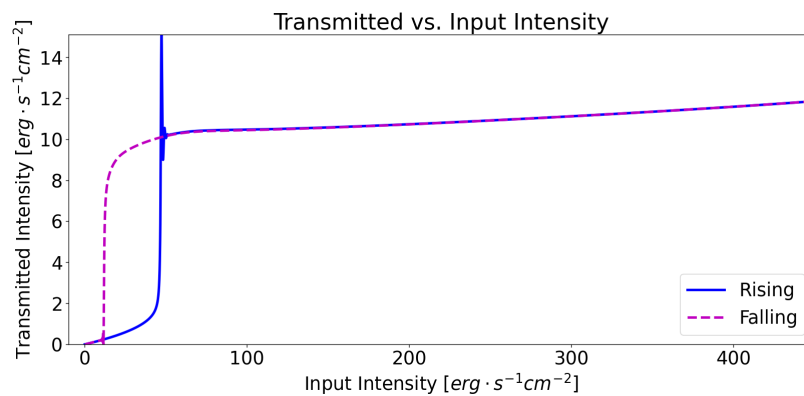
Figure 3.21: Simulation of a cavity consisting of two 6-cell silver plasma mirrors with a Kerr material in between. This shows the (a) intensities over time, (b) cavity intensity (averaged across the cavity) versus input intensity, and (c) transmitted intensity (calculated to the right of the cavity and time-averaged) versus input intensity. Both (b) and (c) show one hysteresis loop.

The relatively sharp increase in transmitted intensity around an input intensity of  $1.05 \times 10^{11} \text{ erg} \cdot \text{s}^{-1} \text{ cm}^{-2}$  is because the Kerr effect creates an effective cavity length that results in maximum transmission at that input intensity. Similarly, the effective length results in maximum transmission on the falling edge until the input drops too low to maintain a sufficient cavity intensity. This causes the hysteresis loops seen in Fig. 3.21(b) and Fig. 3.21(c). For many of the input intensities in Fig. 3.21(b)

and Fig. 3.21(c), changing the input has little effect on the transmitted intensity. Further increasing the input intensity beyond the level shown in Fig. 3.21(b) and Fig. 3.21(c) will have very little effect, as seen in Fig. 3.22.



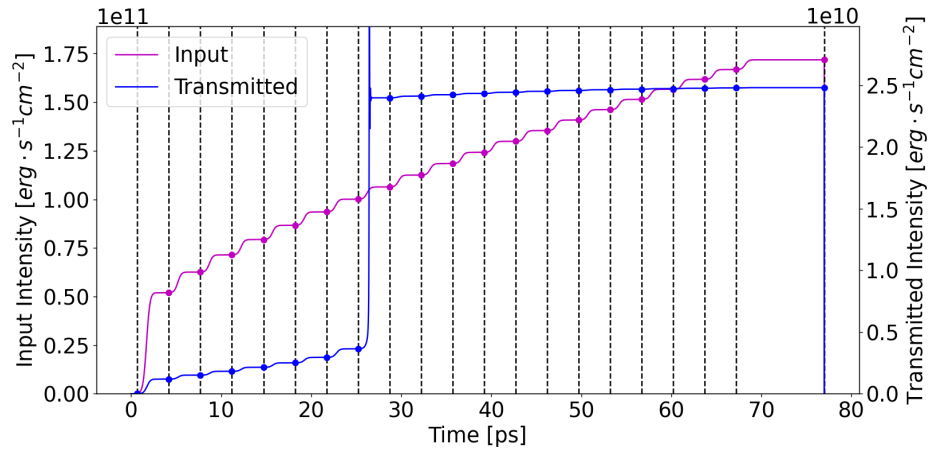
(a)



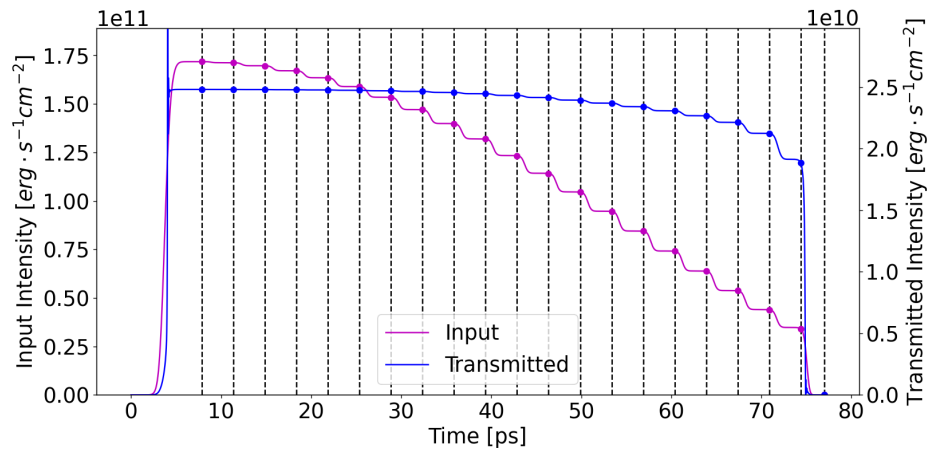
(b)

Figure 3.22: Simulation of a cavity consisting of two silver plasma mirrors with a Kerr material in between. The input intensity is raised higher than in Fig. 3.21. This shows (a) the cavity intensity (averaged across the cavity) versus input intensity, and (b) the transmitted intensity (calculated to the right of the cavity and time-averaged) versus input intensity. Both (a) and (b) show one hysteresis loop despite the higher input intensity than in Fig. 3.21(b) and Fig. 3.21(c).

The hysteresis is due to the fact that for one input intensity, there are two stable transmitted intensity states. The hysteresis is not simply caused by a time delay. To verify this, the input intensity can be raised in a staircase manner, allowing adequate time for the transmitted intensity to stabilize before being raised again. The input and transmitted intensities from the staircase simulation are shown in Fig. 3.23. In Fig. 3.24, the values indicated by dots in Fig. 3.23 are overlaid with the smooth plots of Fig. 3.21(c) showing the hysteresis loops remain identical.



(a)



(b)

Figure 3.23: Stairstep simulation showing intensity over time of a cavity consisting of two 6-cell silver plasma mirrors with a Kerr material in between. The dots show the values recorded at a point of time during which the simulation has stabilized. (a) The input increases from a low value, and (b) the input decreases from an initial high value.

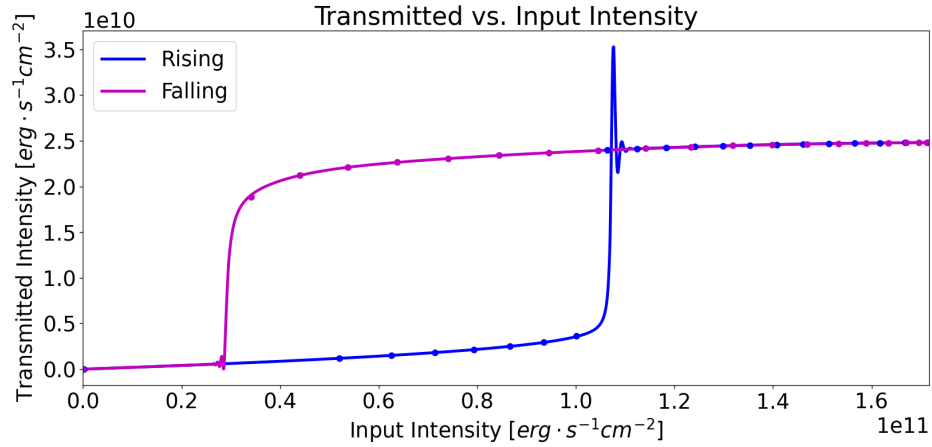


Figure 3.24: Simulation of a cavity consisting of two 6-cell silver plasma mirrors with a Kerr material in between. This plots the transmitted intensity (calculated to the right of the cavity and time-averaged) versus input intensity, and the plot shows one hysteresis loop. The dots correspond to the dots taken from Fig. 3.23.

Since there is a time delay between the input and the transmitted signal responding, it is important to run the simulation for enough time to get an accurate mapping of input to transmitted intensities. It was shown in Fig. 3.24 that this was the case for a 70 ps simulation since the dots after each staircase in Fig. 3.23 correspond to the smooth hysteresis plot in Fig. 3.24. If the simulation is run for a shorter amount of time, it distorts the hysteresis loop as shown in Fig. 3.25. Though the device settles at the same transmitted intensity in all cases, plotting the transmitted intensity compared to input intensity shows significant differences. Running a long simulation is more accurate than simply adding in a time delay because of the complex interactions of the signals within the cavity. Fig. 3.25 shows that not only the transmitted intensity compared to input intensity values differ, but also the hysteresis loop shape differs.

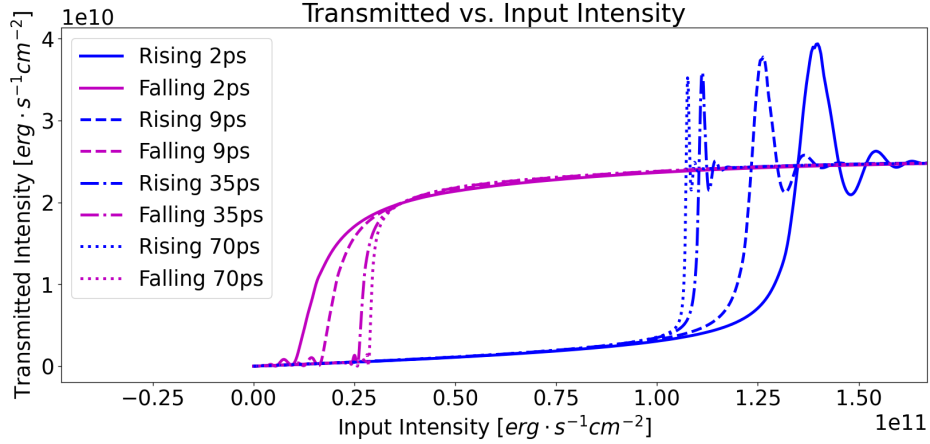


Figure 3.25: Hysteresis loops for simulations with a varying duration of time. The longest simulation, 70 ps, corresponds to Fig. 3.21. A shorter simulation distorts the hysteresis loop shape.

The waveforms when the device is in the nonlinear region of operation show signals with multiple frequency components, as shown in Fig. 3.26. The frequency components transmitted can be viewed using a Fourier transform. A majority of the signal remains at the fundamental frequency of 500 THz, although the third and fifth harmonics are also quite significant as shown in Fig. 3.27, as expected. The reason for the higher frequency components can easily be seen when looking at an electromagnetic signal in exponential form,

$$E = \frac{1}{2}A^\omega e^{-j\omega t} + \frac{1}{2}A^{-\omega} e^{j\omega t}, \quad (3.7)$$

where  $A^\omega$  and  $A^{-\omega}$  are constants related to the electric field's magnitude. Cubing the electric field of Eq. 3.7, yields

$$E^3 = \frac{1}{8}(A^\omega)^3 e^{-3j\omega t} + \frac{3}{8}(A^\omega)^2 A^{-\omega} e^{-j\omega t} + \frac{1}{8}(A^{-\omega})^3 e^{3j\omega t} + \frac{3}{8}(A^{-\omega})^2 A^\omega e^{j\omega t}, \quad (3.8)$$

which clearly has the third harmonic component [49]. Once the fundamental frequency and the third harmonic frequency begin interacting in a Kerr material, higher order frequency components begin to appear, including the fifth harmonic, the seventh harmonic, etc.

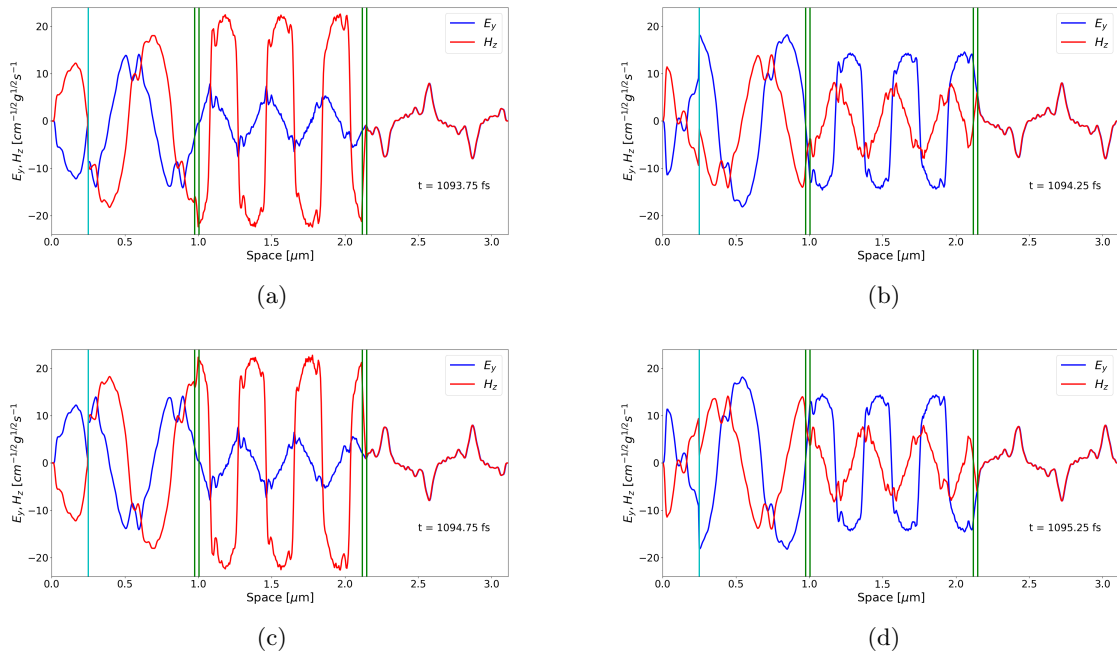


Figure 3.26: The magnitudes of  $E_y$  and  $H_z$  oscillate during the simulation of a Kerr cavity surrounded by mirrors. (a)-(d) capture points in time showing this oscillation within the cavity. The mirror surfaces are shown as green vertical lines. The light blue vertical line is the origin. The transmitted fields maintain a constant magnitude. These snapshots occur when the input is at the maximum and held in the plateau region.

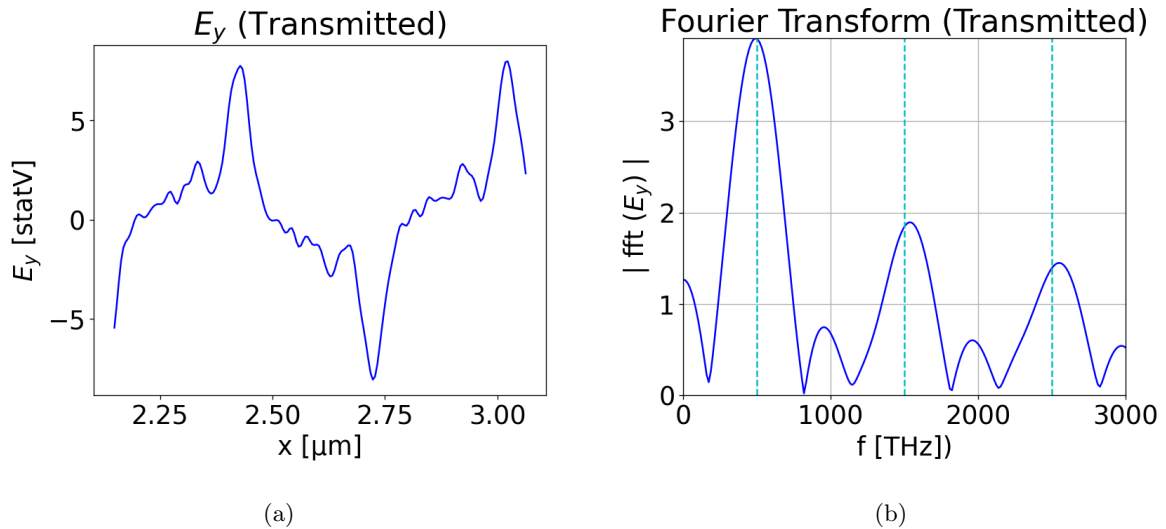


Figure 3.27: (a) The transmitted electric field  $E_y$  and (b) its Fourier transform induced by the Kerr cavity. The vertical dashed cyan lines in (b) correspond to the fundamental, third, and fifth harmonics.

### 3.7 LORENTZ FORMULATION

The Lorentz formulation in FDTD that was described in Ch. 2 will be used to simulate a cavity with both Kerr and Lorentz characteristics as shown in Fig. 3.28.

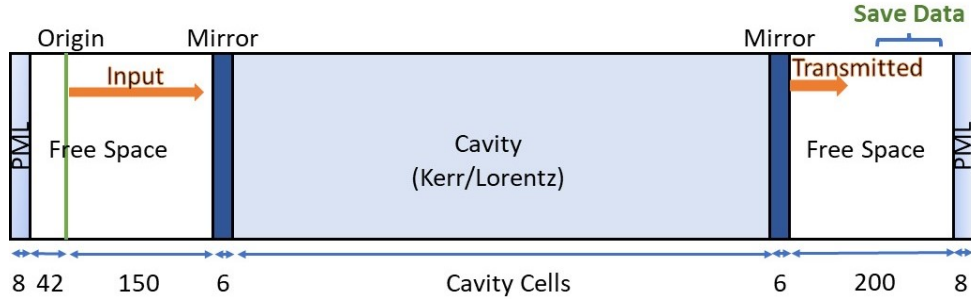


Figure 3.28: Simulation setup of two 6-cell thick mirrors used to form a cavity with a Kerr/Lorentz material in between the mirrors. The pulse propagates from left to right starting at the origin. Transmitted data is saved to the right of the second mirror.

The Lorentz characteristics chosen are  $\omega_p = 3.82 \times 10^{14}$  rad/s,  $\omega_0 = 3.887 \times 10^{15}$  rad/s, and  $\gamma = 9.7 \times 10^{14}$  rad/s. These were set to the values of DR1-PMMA [62, 63, 64] and are controllable for real materials by doping polymers with various dyes. Further details regarding the effects of  $\omega_0$  and  $\omega_p$  will be explored later in this section.

The transmission as a function of cavity length is shown in Fig. 3.29. These can be compared to Fig. 3.20 for the Kerr-plus-mirrors simulation. The addition of the Lorentz characteristics to the cavity slightly adjusts the cavity length that results in maximum transmission. With the Lorentz characteristics, transmission is higher with 223 cavity cells compared to 224 cavity cells, as seen in Fig. 3.30.

Fig. 3.30 shows the transmission for a Kerr-only material when the cavity is 224 cells. Previously, a cavity length of 224 cells was chosen when the cavity filled with the Kerr material. The 224 cells were chosen for the shape and characteristics of the hysteresis loops. A cavity length of 223 cells is evaluated here for the Kerr/Lorentz cavity.

Using a cavity length of 223 cells from Fig. 3.29, the intensity over time is plotted in Fig. 3.31. The general shapes are quite similar to the Kerr-only cavity in Fig. 3.21. The difference in the hysteresis loops is a combination of the Lorentz material and the difference in cavity length for maximum transmission, with the change in cavity length having the largest effect on the overall mapping of transmitted to input intensities. Fig. 3.32 compares a 223-cell cavity with and without the Lorentz material.

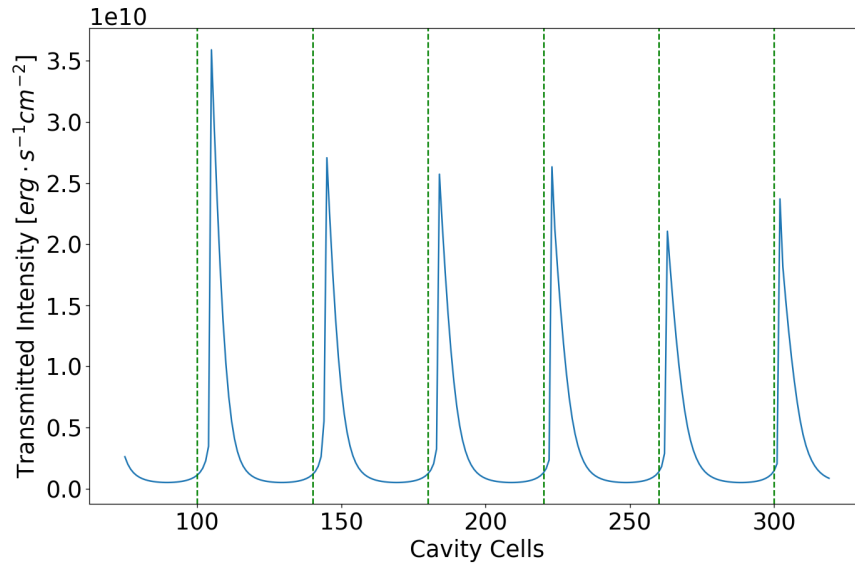


Figure 3.29: The transmitted intensity versus the number of cavity cells of the structure of Fig. 3.28 with even numbers of cavity cells simulated. The green vertical lines correspond to half wavelengths for a 500 THz signal in a material with a refractive index of 1.5. Peak transmission does not occur exactly at the predicted number of cavity cells due to the 6-cell plasma mirrors on either end the cavity and due to the effective refractive index change caused by the Kerr material. The difference in peak transmission amplitude is partially due to the granularity of the simulation.

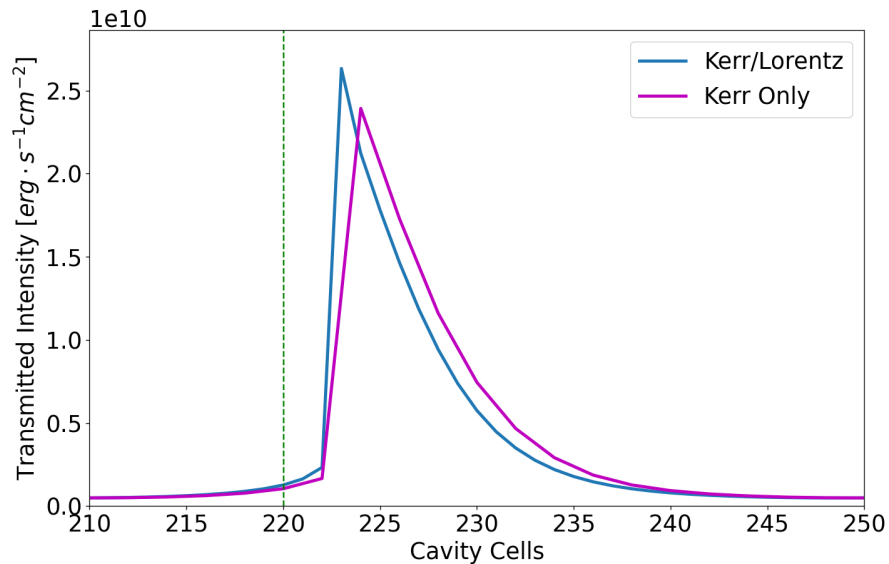


Figure 3.30: The transmitted intensity as a function of the number of cavity cells of the structure of Fig. 3.19 compared to Fig. 3.28. The green vertical line corresponds to a half wavelength for a 500 THz signal in a material with a refractive index of 1.5. Peak transmission occurs with a cavity length of one cell less when comparing the Kerr/Lorentz cavity simulation to the Kerr-only cavity simulation.



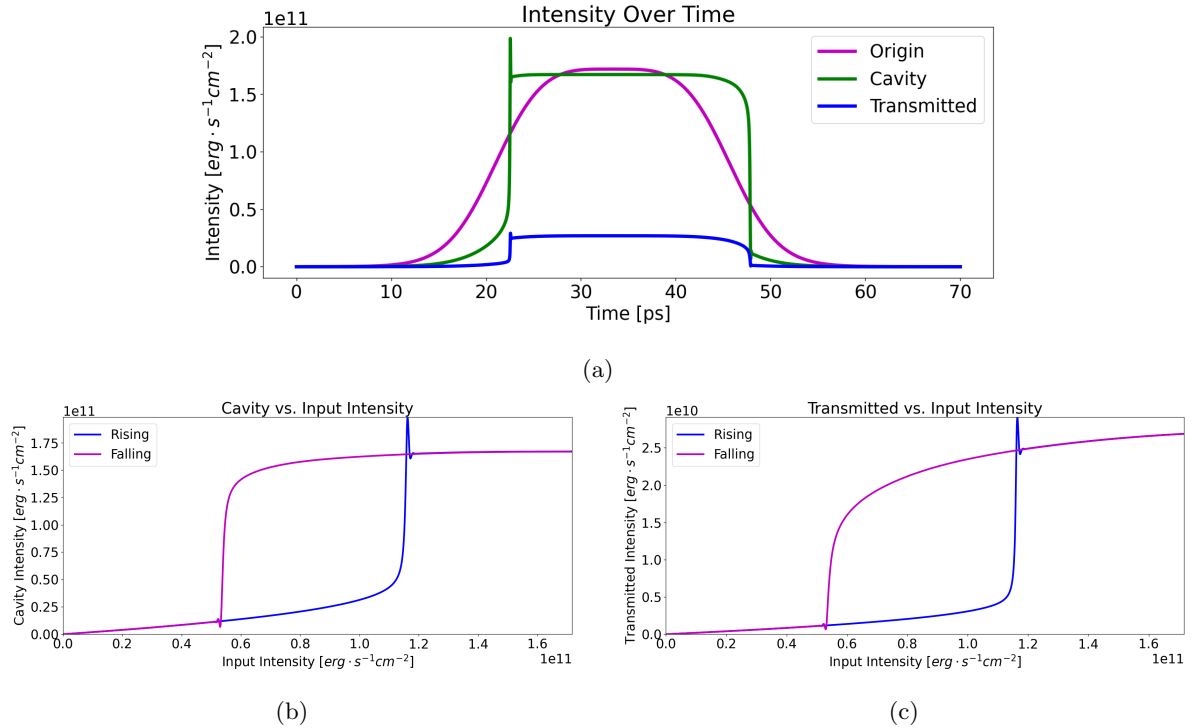


Figure 3.31: Simulation of a cavity consisting of two 6-cell silver plasma mirrors with a Kerr/Lorentz material in between. This shows (a) the intensity over time, (b) the cavity intensity (averaged across the cavity) versus input intensity, and (c) the transmitted intensity (calculated to the right of the cavity and time-averaged) versus input intensity. Both (b) and (c) show one hysteresis loop.

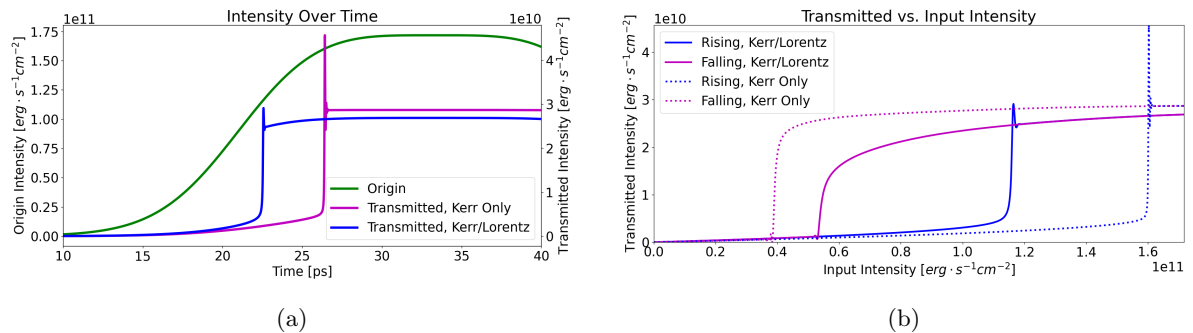
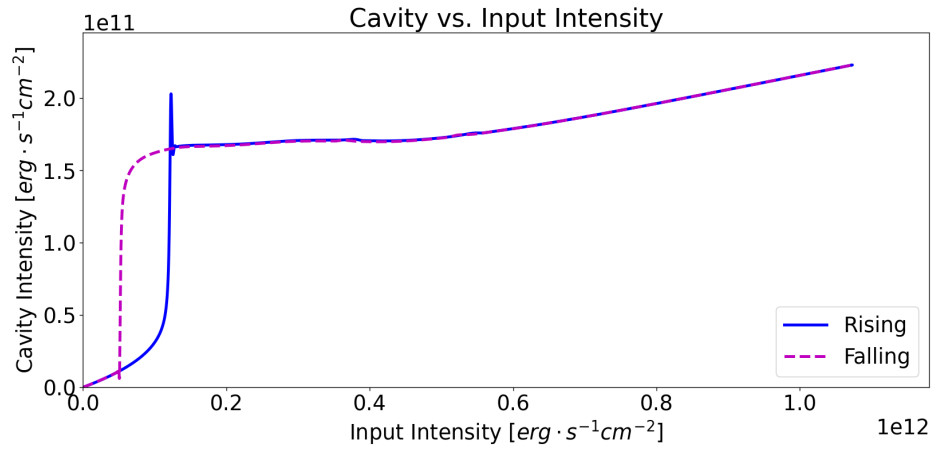
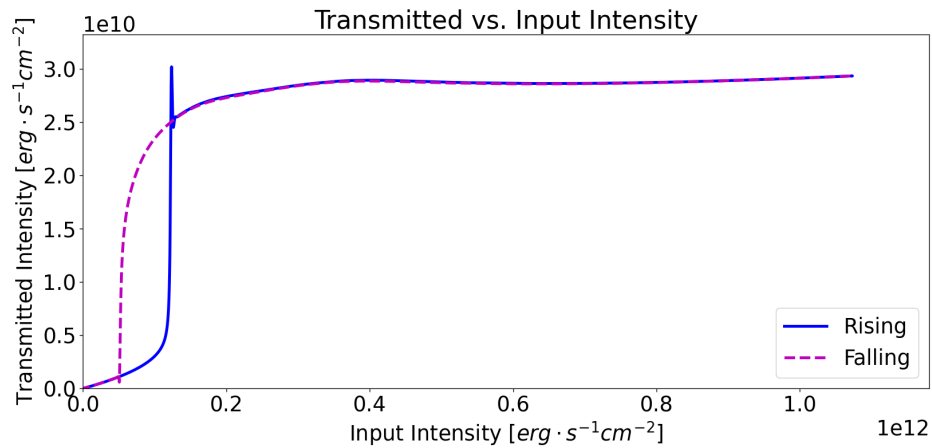


Figure 3.32: Simulation of a cavity consisting of two 6-cell silver plasma mirrors with a Kerr/Lorentz material compared to a Kerr-only material in between. Each cavity between the mirrors is 223 cells. This shows (a) the transmitted intensity over time around the rising edge with the damped ringing when the Lorentz effect is included and (b) the transmitted intensity versus input intensity. Note that the number of cells that trigger the nonlinear response differs in each case due to the Lorentz characteristics affecting the effective refractive index.

Similar to the cavity with only the Kerr material, only one hysteresis loop is present even with a much larger input intensity. The transmitted intensity continues to be relatively optically bistable as seen in Fig. 3.33.



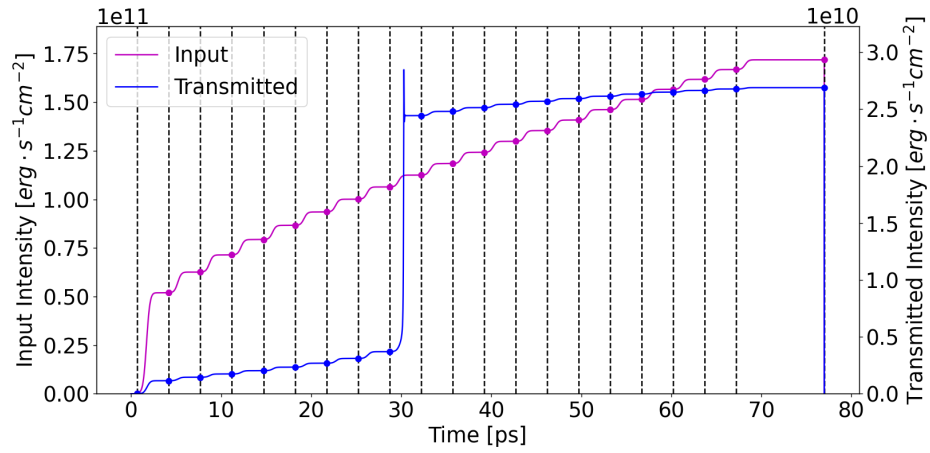
(a)



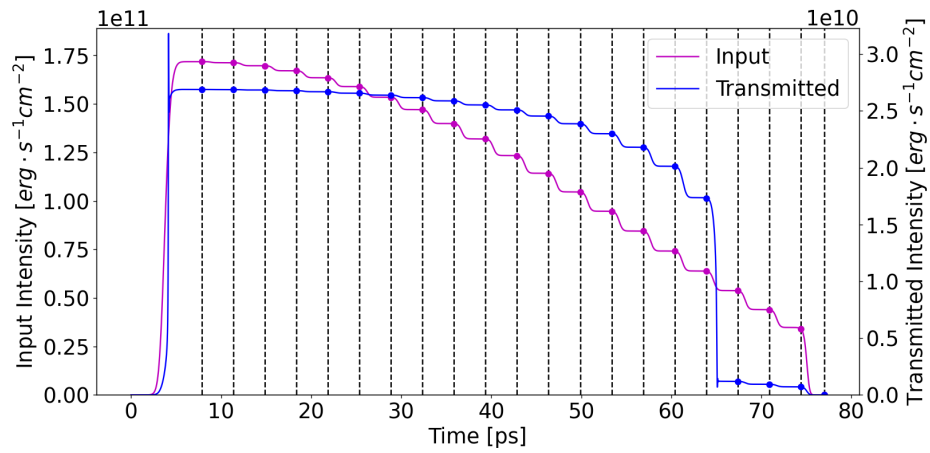
(b)

Figure 3.33: Simulation of a cavity consisting of two silver plasma mirrors with a Kerr/Lorentz material in between. The input intensity is raised higher than in Fig. 3.31. This shows the (a) cavity intensity (averaged across the cavity) versus input intensity, and the (b) transmitted intensity (calculated to the right of the cavity and time-averaged) versus input intensity. Despite the higher input intensity compared to Fig. 3.31(b) and Fig. 3.31(c), both (a) and (b) show one hysteresis loop. Compared to the Kerr-only cavity in Fig. 3.22, there is significantly less ringing on the rising edge.

The input and transmitted intensity staircase simulation is repeated for the Kerr/Lorentz material in Fig. 3.34 to give the system time to equilibrate before each intensity change. The simulation is long enough to accurately map the input intensity to the corresponding transmitted intensity, as shown in Fig. 3.35.



(a)



(b)

Figure 3.34: Stairstep simulation showing intensity over time of a cavity consisting of two 6-cell silver plasma mirrors with a Kerr/Lorentz material in between. The dots show the values recorded at a point in time during which the simulation has stabilized. (a) The input increases from a low value, and (b) the input decreases from an initial high value.

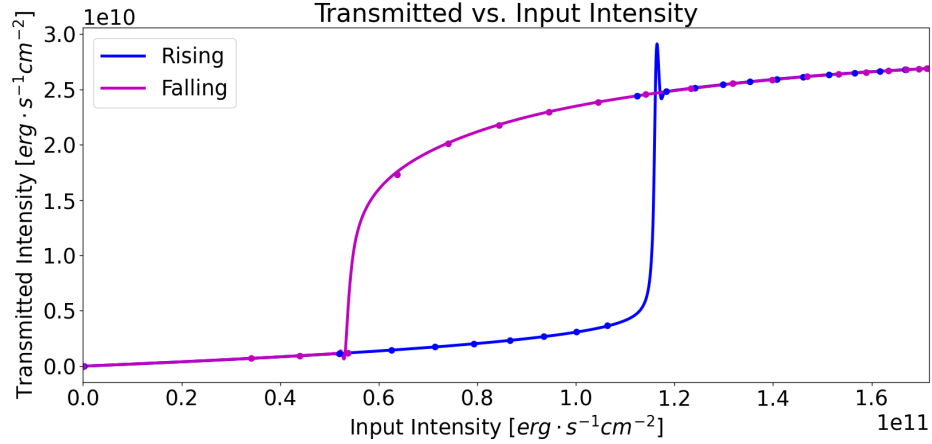


Figure 3.35: Simulation of a cavity consisting of two 6-cell silver plasma mirrors with a Kerr/Lorentz material in between. This plots the transmitted intensity versus input intensity and shows one hysteresis loop. The dots on the plot correspond to the dots taken from Fig. 3.34.

The waveforms when the input generates a nonlinear response are shown in Fig. 3.36. These are generally similar to the waveforms with the Kerr-only cavity.

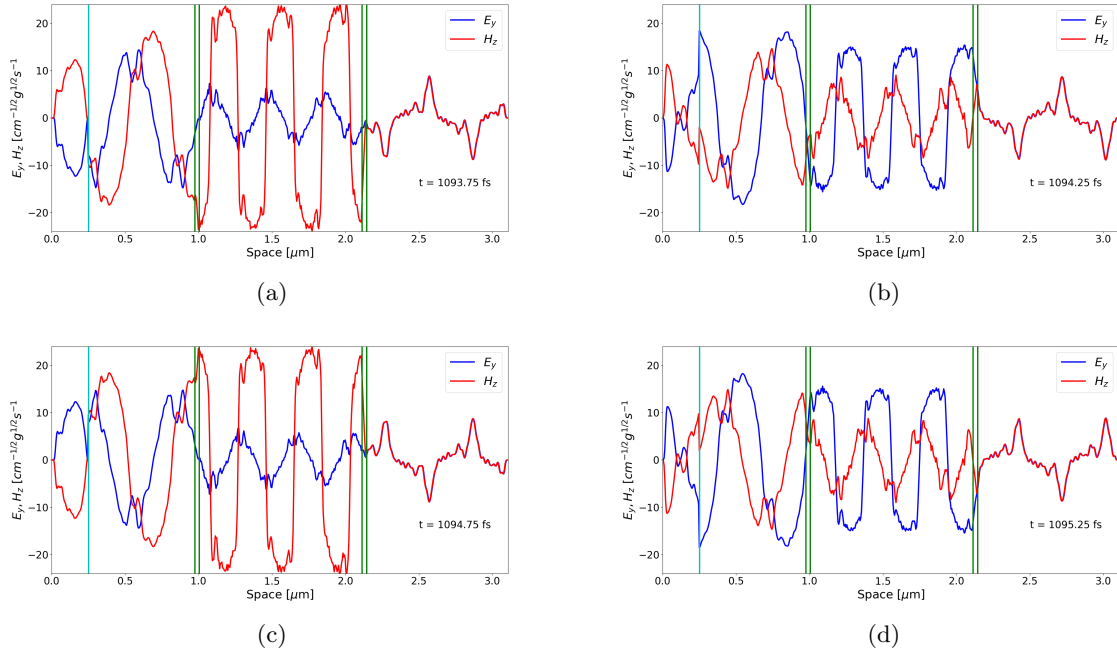


Figure 3.36: The magnitudes of  $E_y$  and  $H_z$  oscillate during the simulation of a Kerr/Lorentz cavity surrounded by mirrors. (a)-(d) capture points in time showing this oscillation within the cavity. The mirror surfaces are shown as green vertical lines. The light blue vertical line is the origin. The transmitted fields maintain a constant magnitude. These snapshots occur when the input is at the maximum and held in the plateau region. The shapes resemble those in Fig. 3.26 for the Kerr-only material.

The frequency components transmitted are again primarily at the fundamental frequency of 500 THz, with the third and fifth harmonics also present as shown in Fig. 3.37.

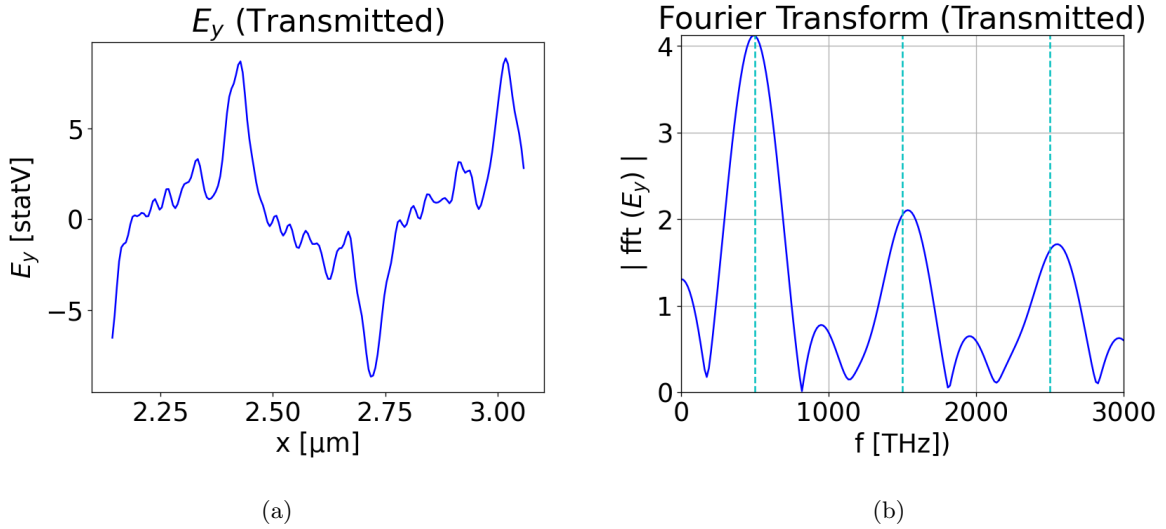


Figure 3.37: (a) The transmitted  $E_y$  signal and (b) its Fourier transform during the nonlinear operating region for a Kerr/Lorentz cavity surrounded by silver mirrors. The vertical dashed cyan lines in (b) correspond to the fundamental, third, and fifth harmonics.

As previously mentioned, the Lorentz parameters chosen correspond to DR1-PMMA. Adjusting the parameters affects the effective refractive index, which will have an effect on the shape of the hysteresis loop. It also has an effect on the amount of ringing. Figure 3.38 shows adjustments to  $\omega_p$  and  $\omega_0$  and the corresponding effects on the hysteresis loops.

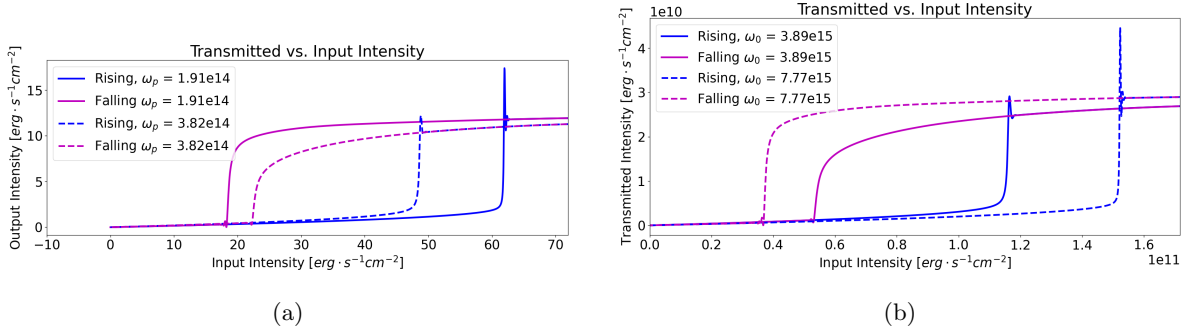


Figure 3.38: Simulation of a cavity consisting of two silver plasma mirrors with a Kerr/Lorentz material in between. The transmitted intensity (calculated to the right of the cavity and time-averaged) is plotted versus the input intensity, showing hysteresis. Lorentz parameters are compared by (a) adjusting  $\omega_p$  and (b) adjusting  $\omega_0$ . The cavity length is held constant at 223 cells. If these parameters are adjusted much more, the ideal cavity length for peak transmission changes because the effective refractive index changes, and the simulation needs to run with an adjusted number of cavity cells to maintain hysteresis. Decreasing  $\omega_p$  or increasing  $\omega_0$  from the values of DR1-PMMA lead to more ringing and more optical bistability.

# CHAPTER 4: LOGIC GATES COMPOSED OF FABRY-PEROT DEVICES

In this chapter, the Fabry-Perot device from Ch. 3 will be used to create logic gates. The behavior of these devices, particularly the bistability, makes them well-suited for logic operations. This chapter will be divided into four main sections. The first will explain how logic gates are created using the Fabry-Perot device. Then, the logic gates will be combined to implement more complicated functionality. Next, some potential challenges with the technology are addressed along with proposed solutions. Finally, a 3-bit and a 4-bit adder are presented using some of the strategies discussed for addressing challenges.

## 4.1 BASIC LOGIC GATE DESIGN

This section describes the basic operation of the Fabry-Perot device used in this work, including detailed simulation inputs. Then each of the basic logic gates (OR, AND, majority, and XOR) is described.

### 4.1.1 BASIC OPERATION

The structure of the device used in this chapter is illustrated in Fig. 4.1. It consists of a total simulation space of 629 cells. There is an eight-cell Perfectly Matched Layer (PML) on either end of the space. The origin is located 50 cells to the right of the left boundary. The input is generated in free space and travels right towards the device. A 6-cell silver plasma mirror borders a cavity, with Kerr and Lorentz characteristics, on both sides. To the right of the device is additional free space where the transmission data is recorded.

The cavity itself is 225 cells long, corresponding to approximately three wavelengths of a 500 THz signal within the material. Although there is slightly higher transmission with 223 cells, which was observed in Ch. 3.7, this specific number of cavity cells was chosen to create more margin below the lower input intensity threshold. In future work, it may be possible to demonstrate the higher transmission using 223 cavity cells, and the resulting characteristics, including a more steady transmission above the rising threshold, may outweigh the superior lower margin provided with the 225 cavity cells. The specific parameters used for the cavity material are summarized in Table 4.1.

The device's primary feature is its optical bistability, as shown in Fig. 4.2. As long as the input intensity remains below a certain threshold, indicated by the green line, the transmitted intensity will remain below a certain value. If the input intensity is above a different threshold, shown by the orange line, the transmitted intensity will be above a certain value. The device operates well as long as the

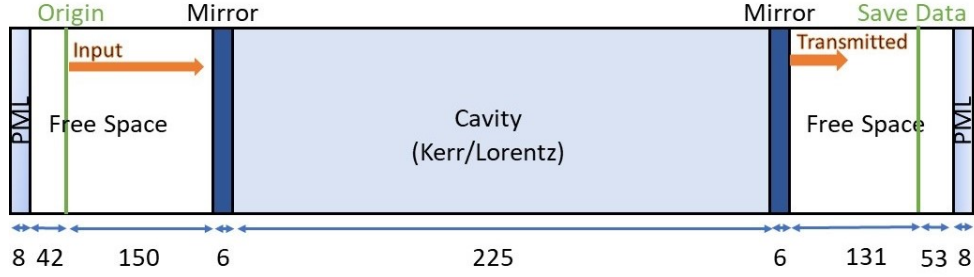


Figure 4.1: The Fabry-Perot device used in this work.

Table 4.1: Summary of Fabry-Perot Device Characteristics based on DR1-PMMA

Component	Characteristic	Value	Reference
Mirrors	$\nu_c$	$57 \times 10^{12}$ rad/s	Ch. 3.3
Mirrors	$\omega_p$	$2 \times 10^{15} \cdot 2\pi$ rad/s	Ch. 3.3
Cavity	$\chi^{(3)}$	$\frac{0.001}{4\pi} \frac{cm^3}{erg}$	Ch. 3.6
Cavity	$\varepsilon^2$	1.5	Ch. 3.6
Cavity	$\omega_p$	$3.82 \times 10^{14}$ rad/s	Ch. 3.7
Cavity	$\omega_0$	$3.887 \times 10^{15}$ rad/s	Ch. 3.7
Cavity	$\gamma$	$9.7 \times 10^{14}$ rad/s	Ch. 3.7

input intensity is not between those two threshold values. Between the two thresholds, the transmitted intensity will depend on the history of the input intensity due to the bistable nature of the device.

The input to the device will be a 500 THz sinusoidal signal within the plateau function envelope previously described in Ch. 3.1, and the operation of the device will depend on amplitude. Because logic gates often involve more than one signal, phase will also play an important role.

These devices cannot simply be placed in series. As seen earlier, two mirrors with free space between them will affect transmission. In order to isolate these devices to prevent interference between them, optical isolators are necessary. Optical isolators are commercially available and only allow light to move in one direction. In FDTD simulation, this is done simply by saving the state of the transmitted signal over time at a given cell to the right of the device. The location at which the data is saved controls the phase of the signal as seen in Fig. 4.3.

Due to the highly reflective mirrors being used, which are lossy, and the loss associated with the Lorentz material, the transmitted signal's intensity is less than the intensity at the origin. An amplifier will be used between devices to adjust the transmitted signal's amplitude to the desired value. Optical amplifiers are also commercially available. These amplifiers will also provide control for logic operations.

The devices are designed to be highly nonlinear, causing components of the transmitted signal to be

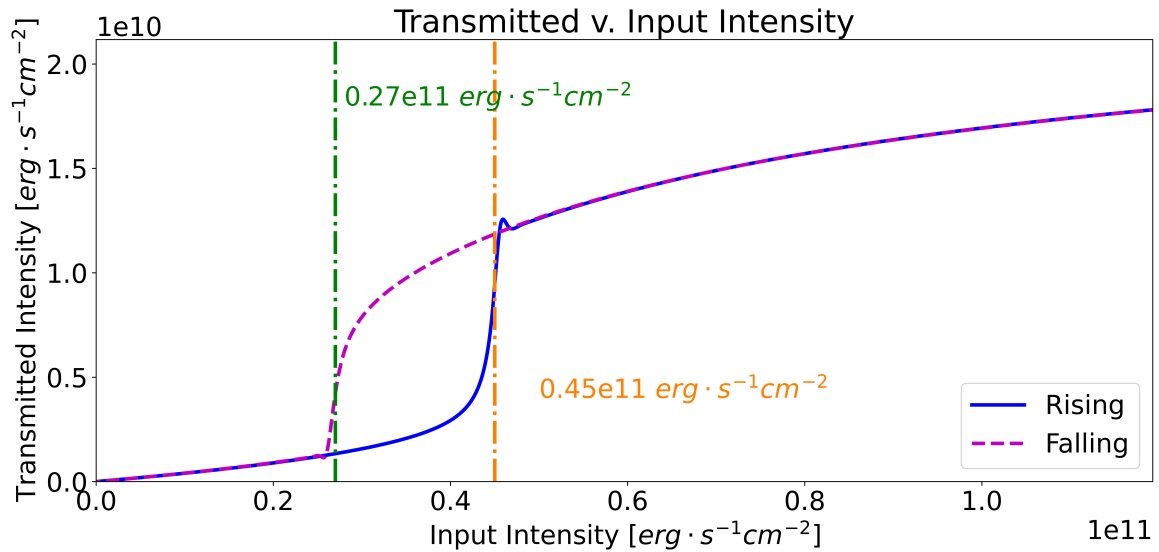


Figure 4.2: Transmitted intensity plotted as a function of input intensity. Once the input intensity is beyond the nonlinear threshold, the transmitted intensity varies much less than the input intensity.

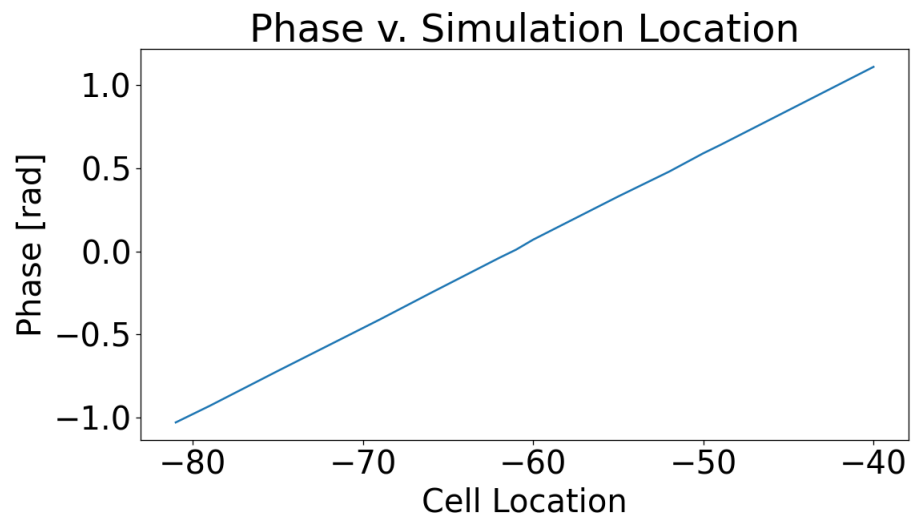


Figure 4.3:  $E_y$  phase as a function of cell location. Cells are located relative to the right edge of the problem space.



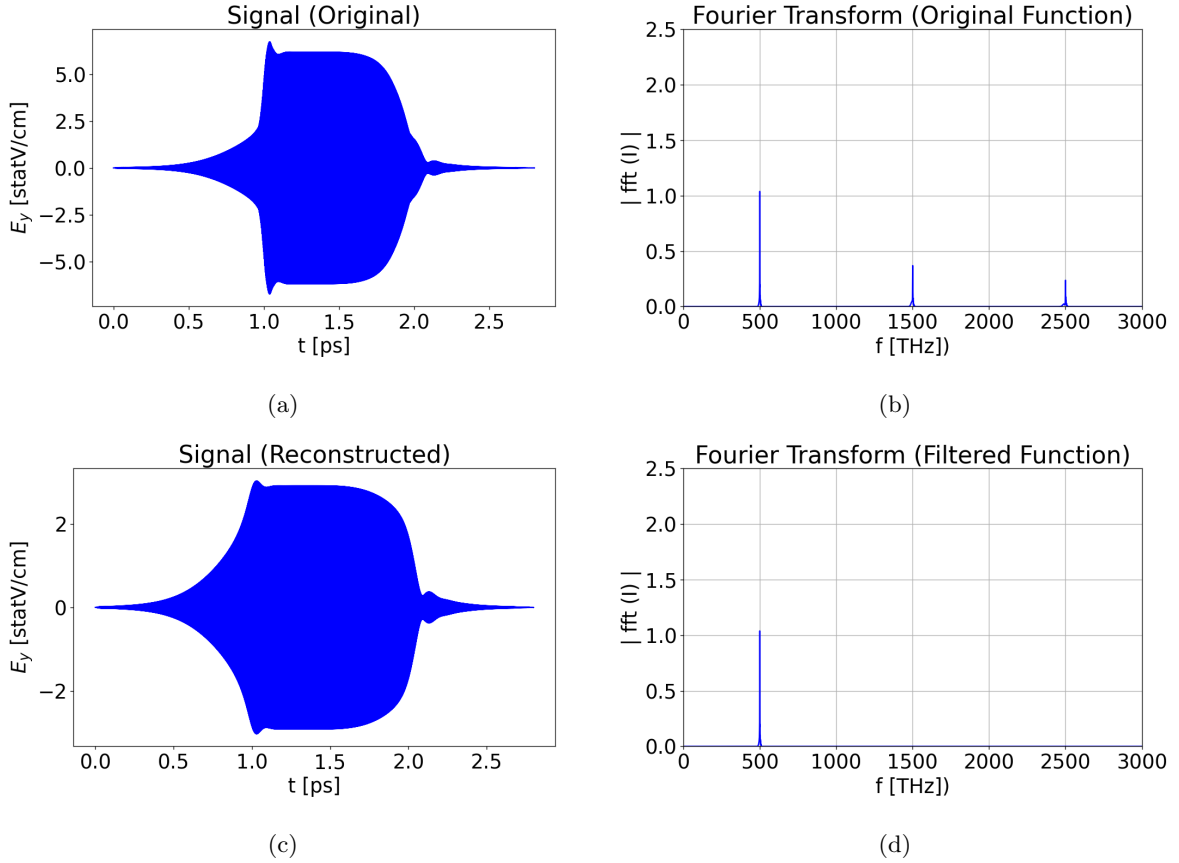


Figure 4.4: Filtering of the transmitted signal showing (a) the original transmitted signal, (b) the Fourier transform of the original transmitted signal, (c) the transmitted signal filtered at 500 THz, and (d) the Fourier transform of the filtered, transmitted signal.

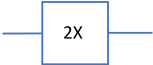


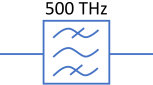
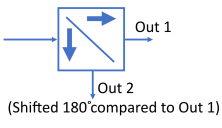
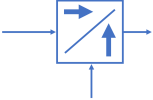
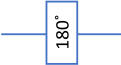
generated at frequencies other than the applied 500 THz signal. In order to send the transmitted signal to the next device, filtering will be required. In FDTD, this can be accomplished with a Fourier transform to isolate the 500 THz frequency component. In practice, notch filters can be used. An example of the  $E_y$  signal with and without filtering is shown in Fig. 4.4, along with the associated Fourier transform data.

In summary, three operations will be performed between devices:

1. Optical isolation
2. Filtering
3. Amplification

All three operations are possible in physical devices and implemented in the FDTD simulation. The symbols for the components used to implement those operations, along with some additional optical components, are given in Table 4.2.

Table 4.2: Optical Components

Component	Symbol	Notes
Amplifier		Includes multiplicative factor applied to each the $E_y$ and $H_z$ fields
Fabry-Perot Device		Configuration shown in Fig. 4.1
Optical Isolator		Light is only allowed to move in the direction indicated
Filter		Only the indicated frequency passes through
Splitter		Splits light into two beams. The beam leaving the bottom will have a $180^\circ$ phase shift compared to the beam leaving the right.
Combiner		Combines light from two beams into one
Phase Plate		Phase is shifted the amount indicated

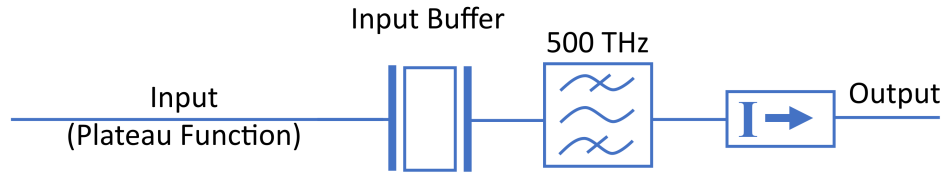


Figure 4.5: Buffering device used for input generation. The input on the left of the figure is generated with a sinusoid within the envelope given by Eq. (3.1). This is input into a Fabry-Perot device. The transmitted (output) signal, after filtering and optical isolation, becomes the input to the logic gates.

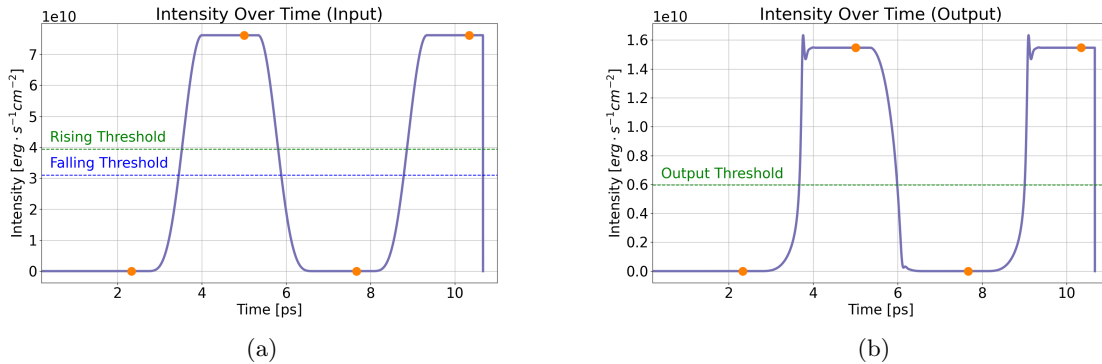


Figure 4.6: Example of (a) an input signal to the buffering device, and (b) the corresponding transmitted signal from the input buffering device used for the inputs to logic gates. The orange dots are the locations at which the logical state is saved, so this example shows four input states.

#### 4.1.2 OPTICAL LOGIC INPUTS

Inputs will be sinusoids within the envelope created using the function described in Ch. 3.1. These inputs are fed into a Fabry-Perot device used as a buffer, as shown in Fig. 4.5. The purpose of buffering the inputs is to create inputs with a realistic shape to be used in the design of logic gates, as opposed to designing the gates with an ideal input envelope. Each pulse is 2.67 ps long. Figure 4.6 shows an example of the input used for the input buffering device and the corresponding output.

#### 4.1.3 OR GATE

The digital OR gate, shown in Fig. 4.7, performs the function described in Table 4.3. This gate can easily be implemented using the Fabry-Perot device by amplifying each of the input signals to a sufficient level to trigger the nonlinear response in the OR gate. Each of the input  $E_y$  and  $H_z$  signals is amplified by 2.5X. If both inputs are a logic ‘1’ and have matching phases, the input amplitude will be far higher than the triggering threshold, but the corresponding transmitted signal will not vary significantly due to the relatively flat output of the Fabry-Perot device.

Figure 4.8 shows the results of the OR operation using inputs generated by the method in Fig. 4.5.

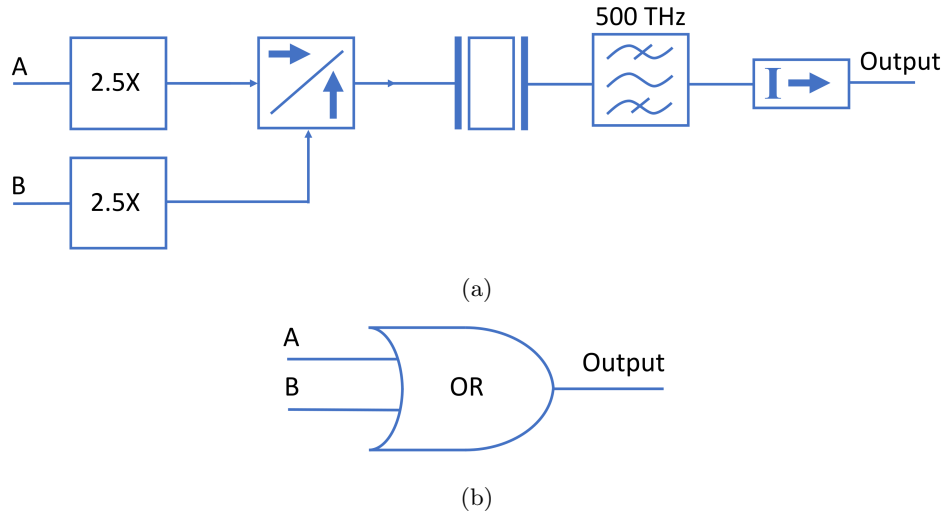


Figure 4.7: (a) Schematic of the OR gate including the input amplifiers, which amplify each signal 2.5X. (b) The symbol used to represent the schematic of (a).

Table 4.3: OR Gate Functionality

Input A	Input B	Output
0	0	0
0	1	1
1	0	1
1	1	1

The output of the OR gate is filtered at 500 THz and optically isolated to prepare it as an input to subsequent devices. The results show the expected output according to Table 4.3.

#### 4.1.4 AND GATE

The digital AND gate, shown in Fig. 4.7, performs the function described in Table 4.4. This gate can be implemented in a similar manner to that used in the OR gate by amplifying each of the input signals less than in the OR gate. In this case, the nonlinear response is triggered only if both input signals are logic '1' and have matching phases. Each of the input  $E_y$  and  $H_z$  signals is amplified by 1.5X.

Fig. 4.10 shows the results of the AND operation using inputs generated in the method of Fig. 4.5. Each of the outputs of the AND gate is filtered at 500 THz and optically isolated to prepare it to be an input to subsequent devices. The results show the expected output according to Table 4.4.

#### 4.1.5 MAJORITY GATE

The same principles used in the AND gate can be adjusted to obtain majority gate of Fig. 4.11. Each input  $E_y$  and  $H_z$  signal is multiplied by 1.2, with the results matching the expected results of Table 4.5,

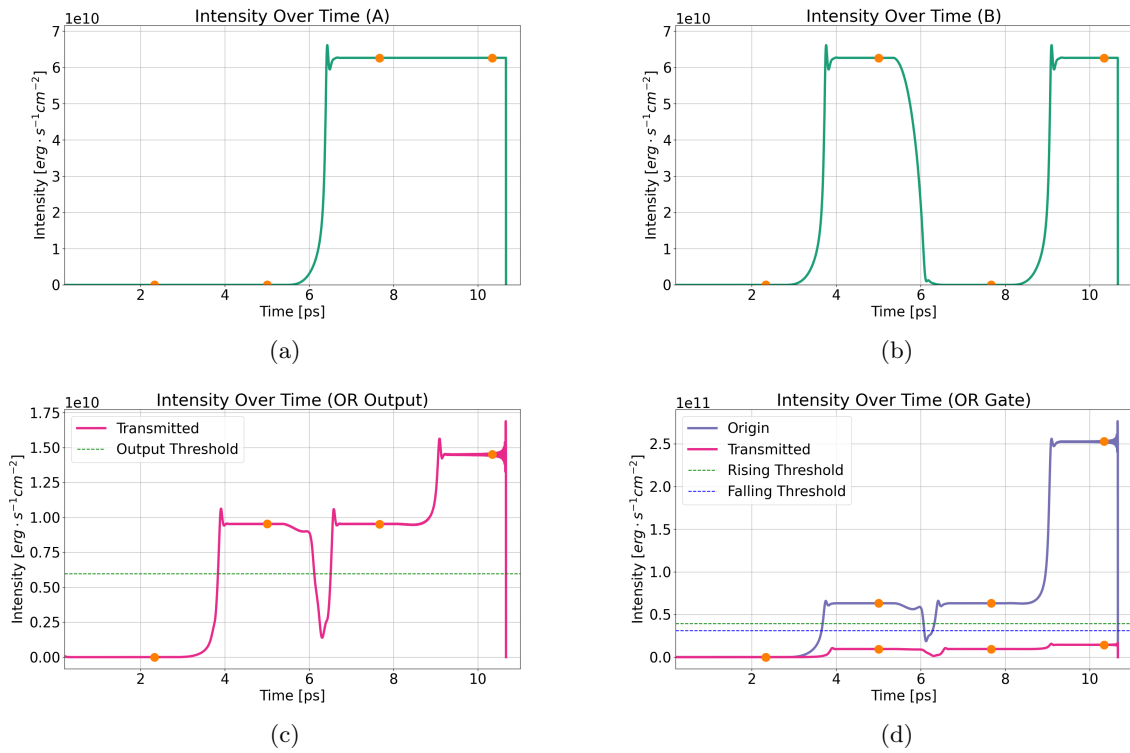


Figure 4.8: OR functionality corresponding to Table 4.3 with the inputs (a) A (post amplification) and (b) B (post amplification) generated with input buffer devices. These inputs are used to generate (c) the transmitted OR gate's signal. The orange dots correspond to the time at which the values are examined for logic values. Any values above the horizontal green line are considered a '1' and those below the green line are '0.' (d) The transmitted and input (post amplification) intensity comparison of the OR gate, showing that the output is naturally buffered compared to the input by the Fabry-Perot device.

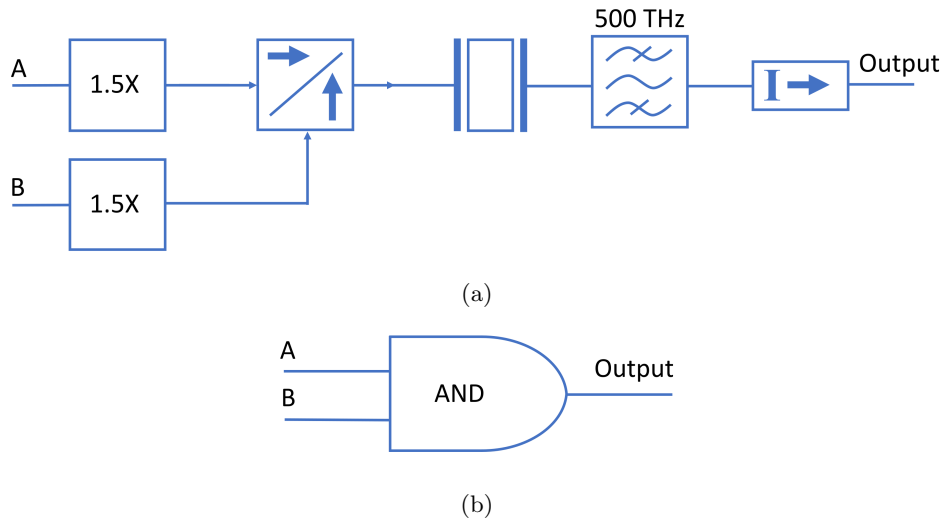


Figure 4.9: (a) Schematic of the AND gate including the input amplifiers, which amplify each signal 1.5X. (b) The symbol used to represent the schematic of (a).

Table 4.4: AND Gate Functionality

Input A	Input B	Output
0	0	0
0	1	0
1	0	0
1	1	1

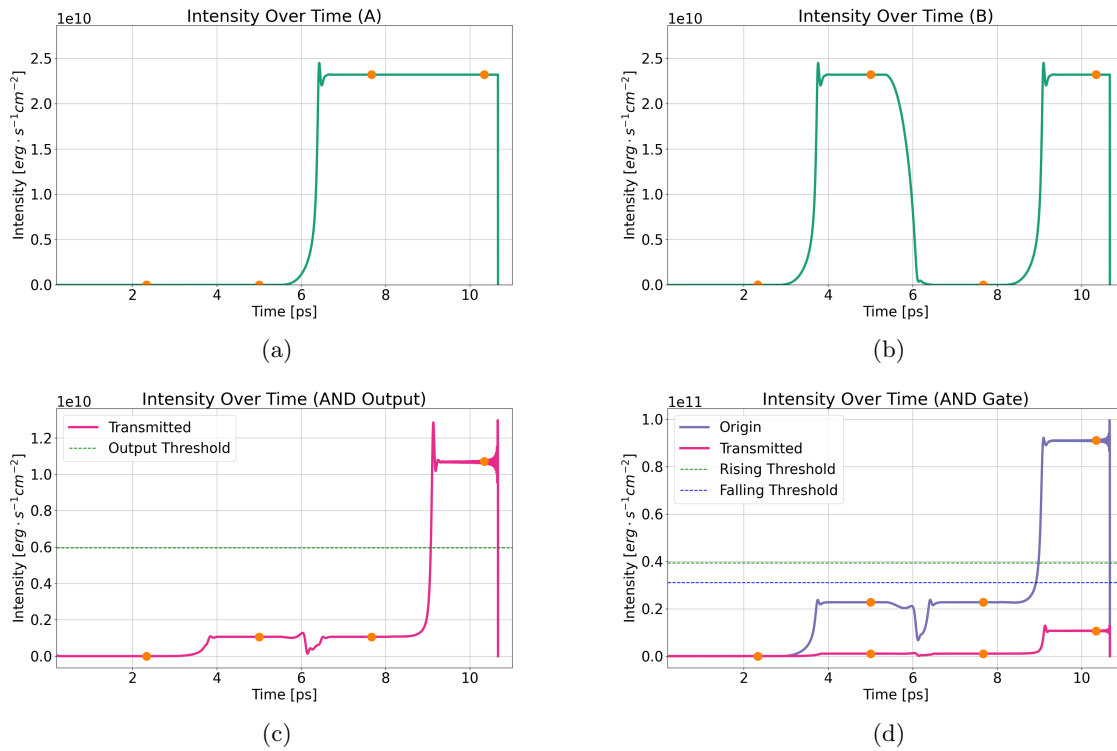


Figure 4.10: AND functionality corresponding to Table 4.4 with the inputs (a) A (post amplification) and (b) B (post amplification) from input buffer devices. These inputs are used to generate (c) the transmitted AND gate's signal. The orange dots correspond to the time at which the values are examined for logic values. Any values above the horizontal green line are considered a '1' and those below the green line are '0.' (d) Transmitted and input (post amplification) intensity comparison of the AND gate, showing that the output is naturally buffered compared to the inputs by the Fabry-Perot device.

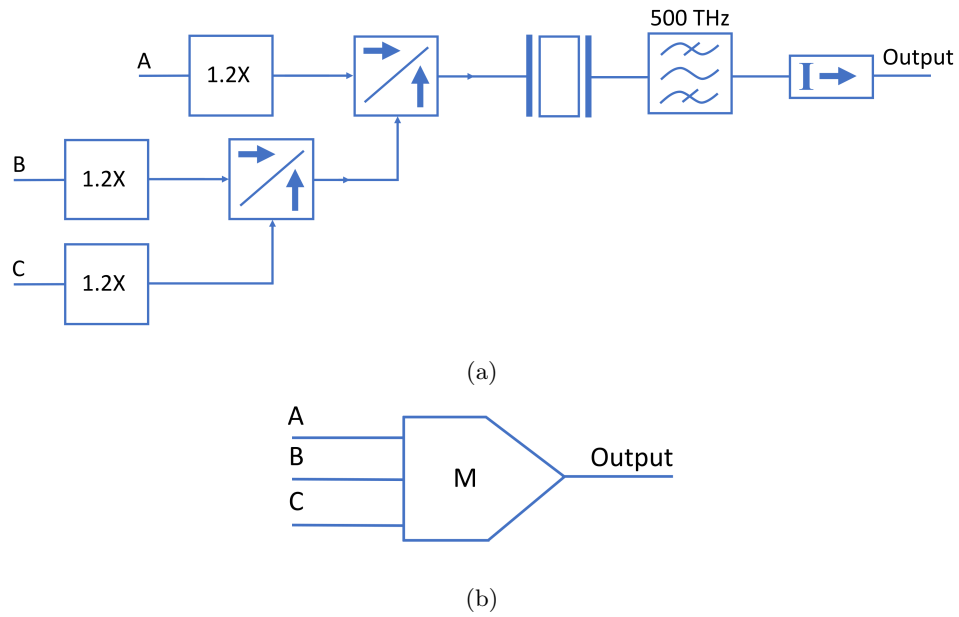


Figure 4.11: (a) Schematic of the majority gate, including the input amplifiers, which amplify each signal 1.2X. (b) The symbol used to represent the schematic of (a).

Table 4.5: Majority Gate Functionality

Input A	Input B	Input C	Output
0	0	0	0
0	0	1	0
0	1	0	0
0	1	1	1
1	0	0	0
1	0	1	1
1	1	0	1
1	1	1	1

which results in a '1' if at least two of the inputs are '1.' The graphical results are shown in Fig. 4.12. The input to output comparison is shown in Fig. 4.13.

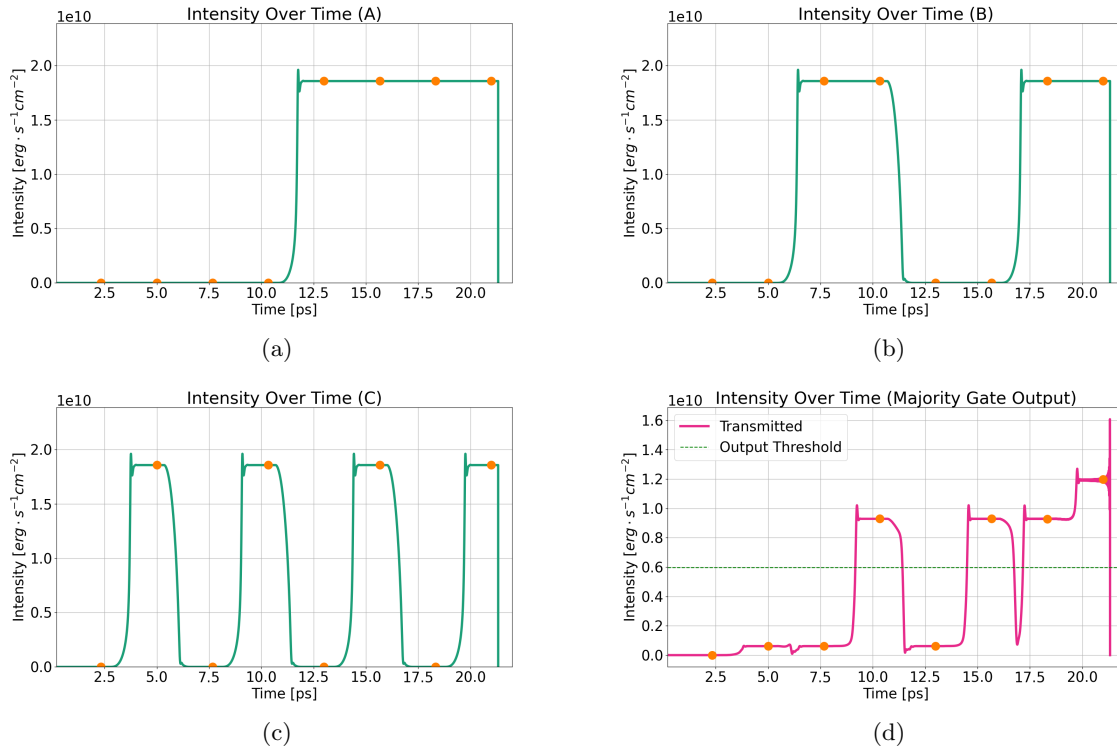


Figure 4.12: Majority gate functionality corresponding to Table 4.5 with the inputs (a) A (post amplification), (b) B (post amplification), and (c) C (post amplification) from input buffer devices. These inputs are used to generate (d) the majority gate's transmitted signal. The orange dots correspond to the time at which the values are examined for logic values. Any values above the horizontal green line are considered a '1' and those below the green line are '0.'

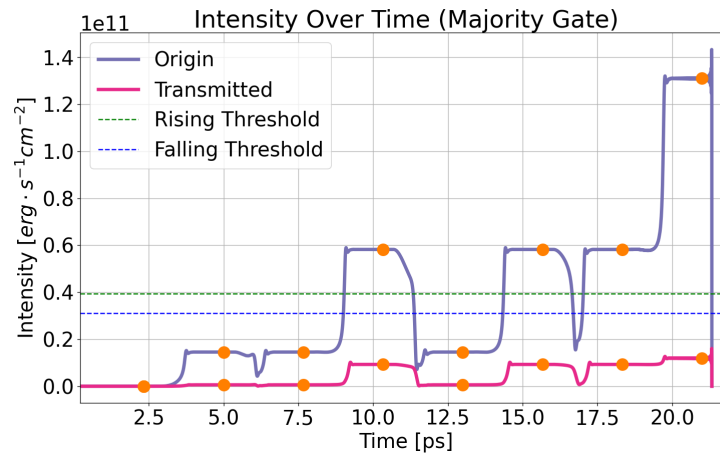


Figure 4.13: The transmitted and input (post amplification) intensity comparison of the majority gate, showing that the output is again naturally buffered compared to the inputs by the Fabry-Perot device.



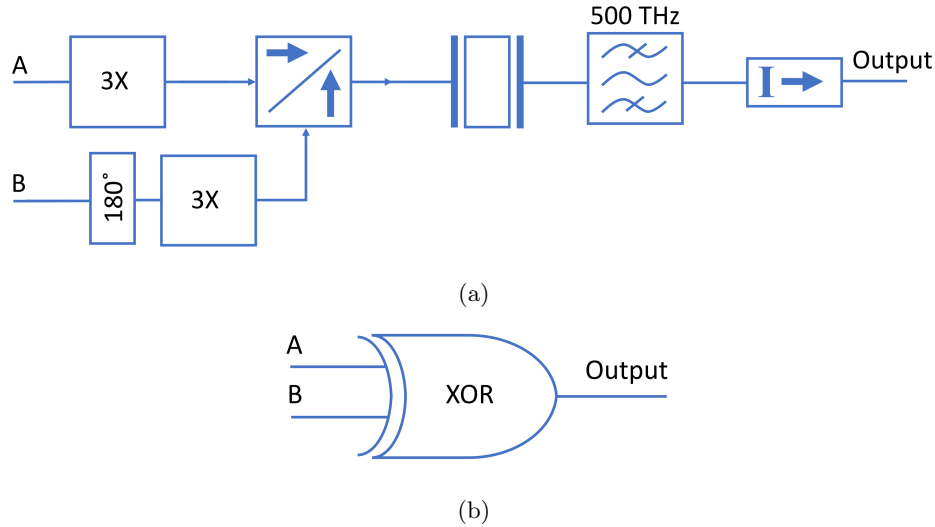


Figure 4.14: (a) Schematic of the XOR gate including the input amplifiers, which amplify each signal 3X. There is a  $180^\circ$  phase shift on one of the inputs. (b) The symbol used to represent the schematic of (a).

Table 4.6: XOR Gate Functionality

Input A	Input B	Output
0	0	0
0	1	1
1	0	1
1	1	0

#### 4.1.6 XOR GATE

The last logic gate necessary in an adder is the XOR gate, shown in Fig. 4.14, that returns the results of Table 4.6. Figure 4.15 shows the inputs into the XOR device, shown as transmitted signals from buffer devices as shown in Fig. 4.5, and the corresponding output (transmitted) signal's intensity. The outputs match the desired functionality shown in Table 4.6. This behavior is generated by multiplying each set of  $E_y$  and  $H_z$  inputs by 3. One set of inputs also undergoes a  $180^\circ$  phase shift using a phase plate, effectively canceling out the other input if both inputs are high.

It is important to note that there is a phase difference when looking at the two logical '1' values. Even though the intensity magnitudes on the second and third dots look the same in Fig. 4.15(c), they have opposite phases because input B is shifted by  $180^\circ$ . This is shown in Fig. 4.16.

This phase difference is problematic because there is a different output depending on whether the first or the second bit is a '1.' The goal in this work is for those outputs to be indistinguishable to any subsequent gates. To remove this phase shift, the proposed 3-gate XOR design uses an OR and an

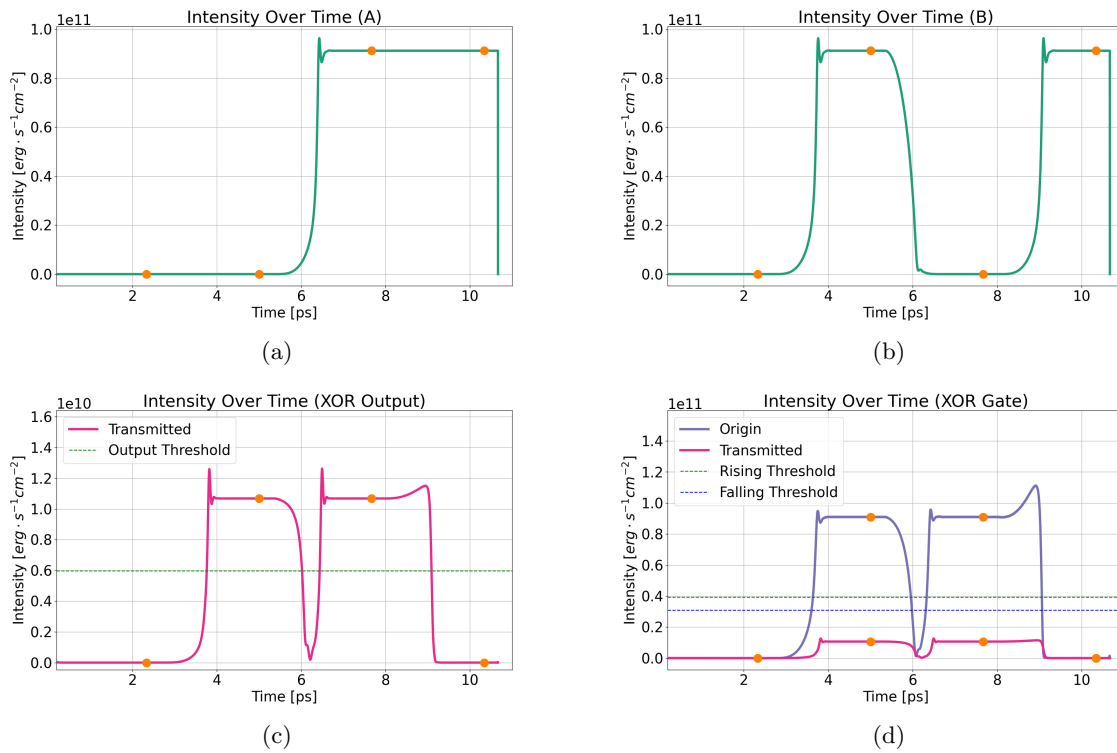


Figure 4.15: XOR functionality corresponding to Table 4.6 with the inputs (a) A (post amplification) and (b) B (post amplification) from input buffer devices. These inputs are used to generate (c) the transmitted XOR gate's signal. The orange dots correspond to the time at which the values are examined for logic values. Any values above the horizontal green line are considered a '1' and those below the green line are '0.' (d) Transmitted and input (post amplification) intensity comparison of the XOR gate.

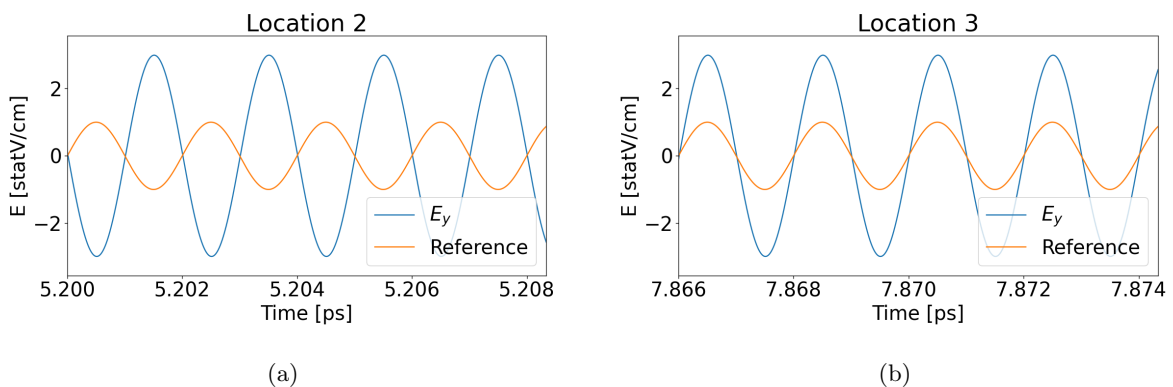


Figure 4.16: Transmitted  $E_y$  from the XOR device shown in Fig. 4.15(c) corresponding to the second and third orange dots. A steady reference sinusoidal wave is shown in orange to compare with the transmitted  $E_y$  shown in blue. Though the magnitude is the same in both cases, (a)  $E_y$  is out of phase with the reference signal, corresponding to input B being a '1,' and (b)  $E_y$  is in phase with the reference signal, corresponding to input A being '1.'

Table 4.7: Phase-Compensated XOR Logic corresponding to Fig. 4.17

Input A	Input B	Out 1	Out 2	A XOR B
0	0	0	0	0
0	1	1	0	1
1	0	1	0	1
1	1	1	1	0

AND gate to feed in the data to the XOR gate already described, as shown in Fig. 4.17. The OR and AND gates composing the 3-gate phase-compensated XOR are identical to those previously described. The XOR functionality, from the amplifiers onward in the signal path, is the same as that described in Fig. 4.14(a) except that the phase plate is unnecessary. The corresponding truth table is shown in Table 4.7. The output of the OR gate will always have the same phase. Since this signal is always the first bit of the single XOR gate, the output phase of the single XOR gate will be consistent regardless of input. The only time an input to the XOR gate will be phase-shifted is if both inputs are high, and the signals should cancel each other out in this situation.

The intensity results are shown in Fig. 4.18, and the  $E_y$  phase is shown in Fig. 4.19. In this case, the outputs are tuned to be the same magnitude with a ‘1’ that they were in Fig. 4.15(c). This means there is a nonzero intensity magnitude for the transmitted signal on the fourth location in Fig. 4.18(c), corresponding to the inputs A and B canceling out. That can be adjusted by reducing the magnitude of the amplification of the first bit into the single XOR gate to adjust the interaction of the OR and AND outputs going in to the single XOR gate, though phase mismatch between the OR and AND outputs prevents that value from being zero.

All XOR gates going forward will be the phase-compensated XOR shown in Fig. 4.17(a) due to the better phase matching. Each of the three gates forming the phase-compensated XOR will be shown in schematics to clearly identify how many Fabry-Perot devices are required for the design implementation as shown in Fig. 4.17(b).

## 4.2 ADDER DESIGN

This section describes how the logic gates described in the previous section can be used together to create a half-adder, a full-adder, and a 2-bit adder.

### 4.2.1 HALF-ADDER

Now that the logic gates have been described, they can be put together to implement more complicated functionality. The half-adder consists of the phase-compensated XOR of Fig. 4.17 and an extra splitter for generating the CARRY bit. The truth table is shown in Table 4.8. Since these gates have

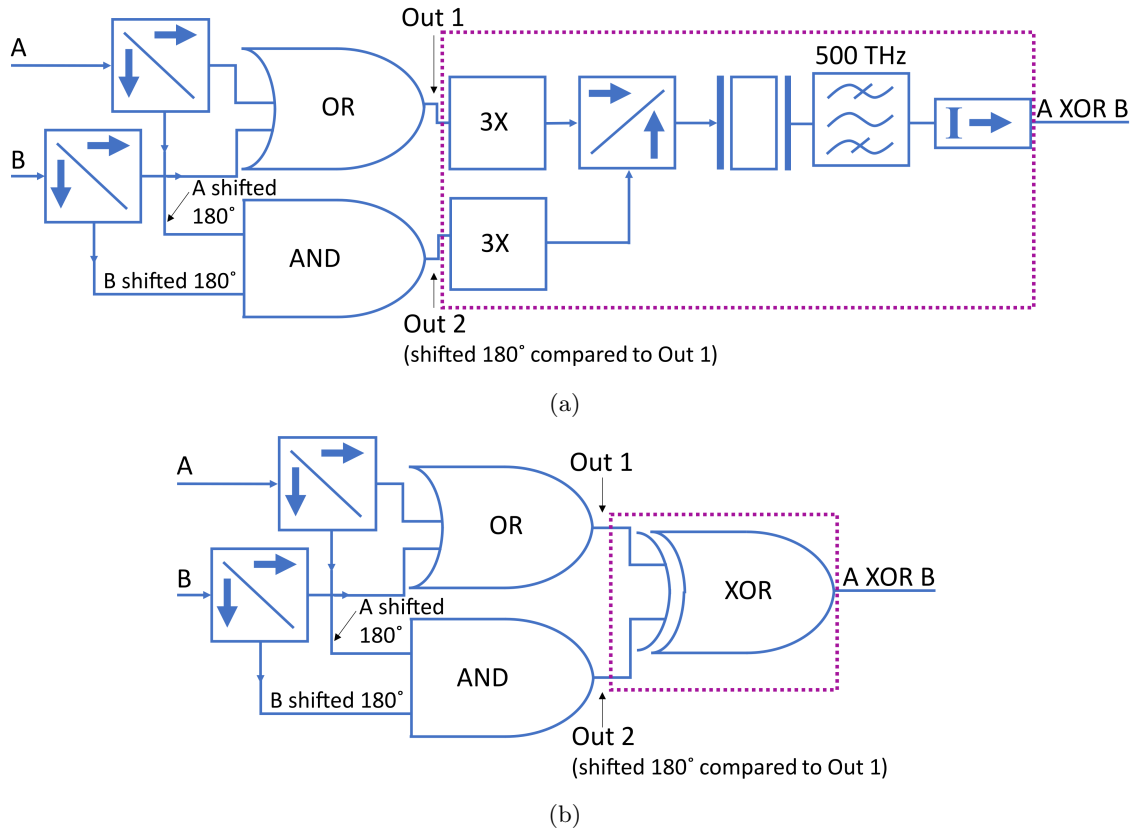


Figure 4.17: (a) The phase-compensated XOR gate consists of two splitters, an OR gate, an AND gate, two amplifiers, a combiner, one Fabry-Perot device, a filter, and an optical isolator. Since the splitter shifts one output  $180^\circ$ , the phase plate of Fig. 4.14 is not necessary. This version of the XOR gate ensures the output has the same phase whether only input A or input B is a '1.' (b) The schematic used for the phase-compensated XOR gate going forward. This includes the AND and OR gates in the schematic to show how many Fabry-Perot devices are required in a schematic. The area enclosed in a rectangle in (a) is abbreviated as shown in (b). Note one input of the XOR gate expects an input phase shifted  $180^\circ$  compared to the other input.

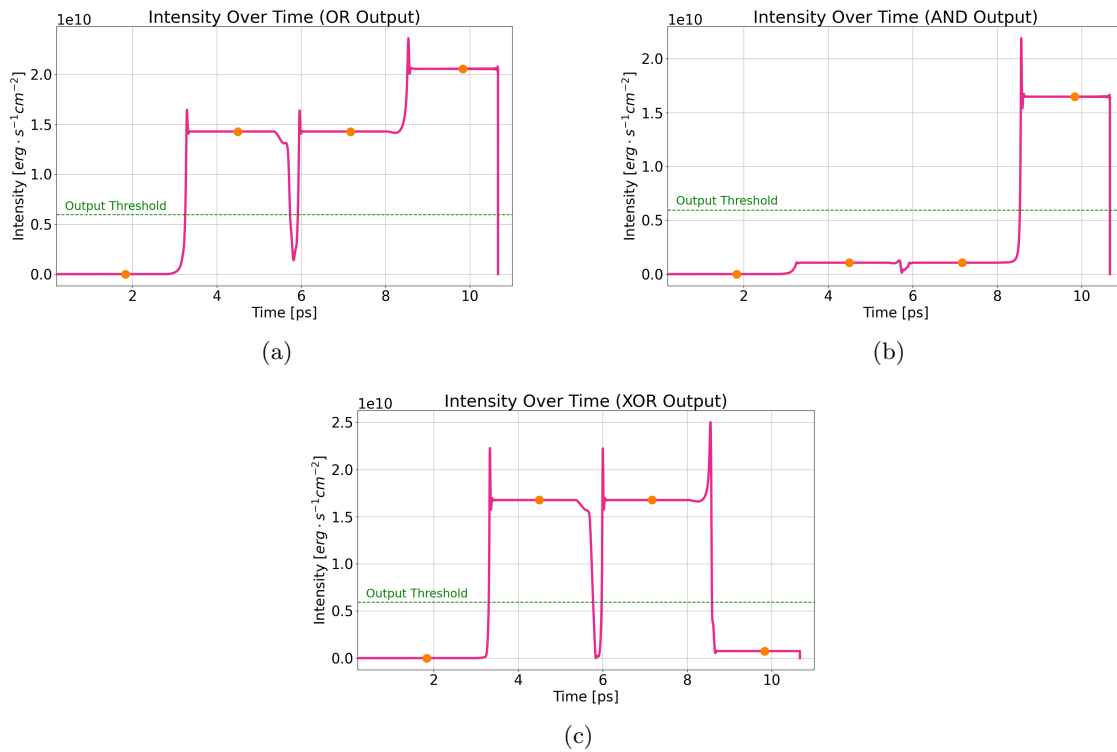


Figure 4.18: XOR functionality corresponding to Fig. 4.17 and Table 4.7 with the same inputs A and B from Figs. 4.15(a) and (b). The intermediate outputs of (a) OR from Fig. 4.17 and (b) AND from Fig. 4.17 are fed into the single XOR gate, resulting in (c) the transmitted XOR gate's signal. The orange dots correspond to the time at which the values are examined for logic values. Any values above the horizontal green line are considered a '1' and those below the green line are '0.'

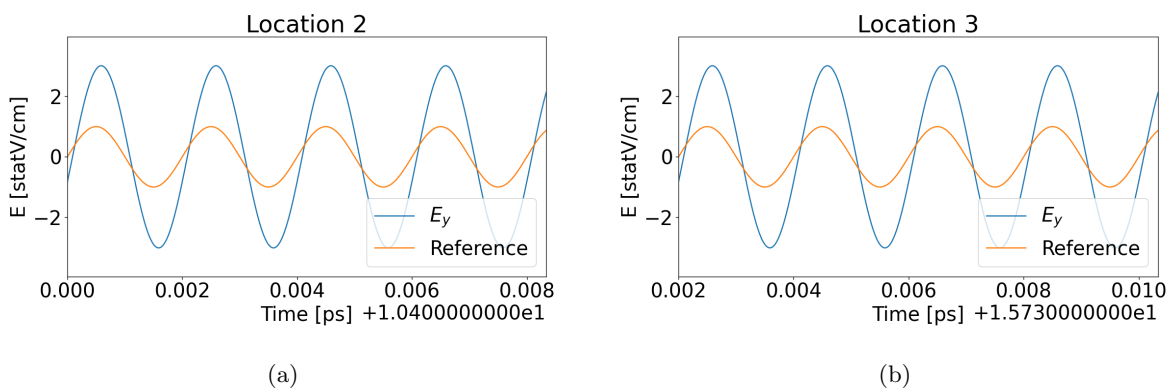


Figure 4.19: Transmitted  $E_y$ , the intensity of which was shown in Fig. 4.18(c), generated by the output of the phase-compensated XOR in Fig. 4.17(a). A steady reference sinusoidal wave is shown in orange to compare with the transmitted  $E_y$  shown in blue. The magnitude is the same in both cases. Additionally, (a)  $E_y$  is in phase with the reference signal, corresponding to input B being a '1' at the second orange dot in Fig. 4.18(c), and (b)  $E_y$  is in phase with the reference signal, corresponding to input A being '1' at the third orange dot in Fig. 4.18(c).

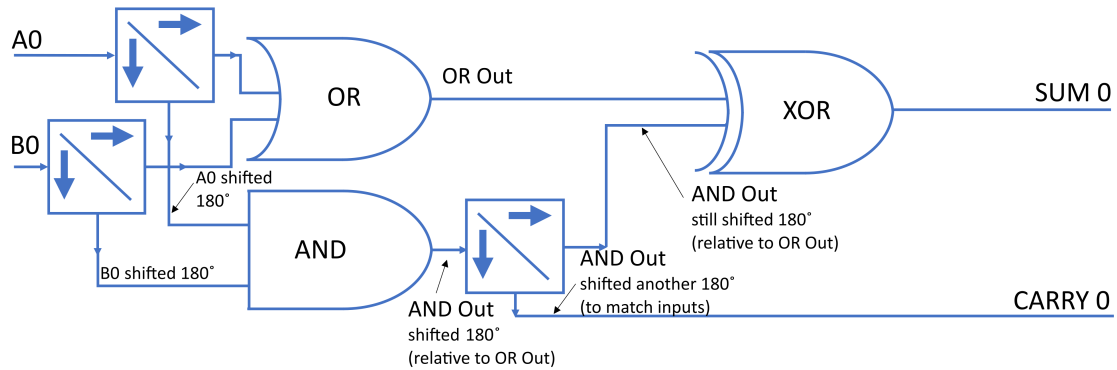


Figure 4.20: The half-adder schematic.

Table 4.8: Half-Adder Logic corresponding to Fig. 4.20

Input A	Input B	SUM	CARRY
0	0	0	0
0	1	1	0
1	0	1	0
1	1	0	1

already been described, the result of the SUM bit will be the same as Fig. 4.18(c) and the CARRY bit will be the same result as in Fig. 4.10(c), given the inputs of Figs. 4.10(a) and (b).

#### 4.2.2 FULL-ADDER

The full-adder, though more complicated than the half-adder, uses similar building blocks. However, instead of an AND gate being used to generate the CARRY, a majority gate is used. The schematic is shown in Fig. 4.21. It consists of two sets of the phase-compensated XOR. The truth table is shown in Table 4.9. The SUM and CARRY outputs are shown in Fig. 4.22.

The full-adder has a more complex response than the half-adder since more signals must be mixed

Table 4.9: Full-Adder Logic corresponding to Fig. 4.21

Input A	Input B	Input C	SUM	CARRY
0	0	0	0	0
0	0	1	1	0
0	1	0	1	0
0	1	1	0	1
1	0	0	1	0
1	0	1	0	1
1	1	0	0	1
1	1	1	1	1

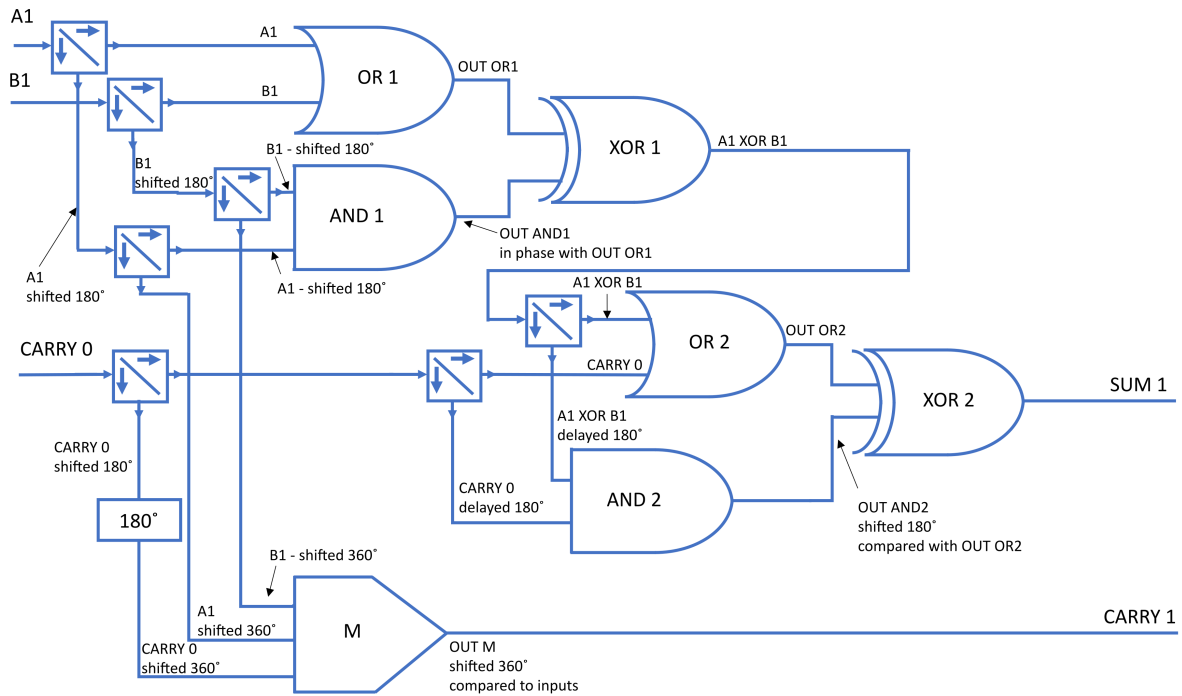


Figure 4.21: The full-adder schematic.

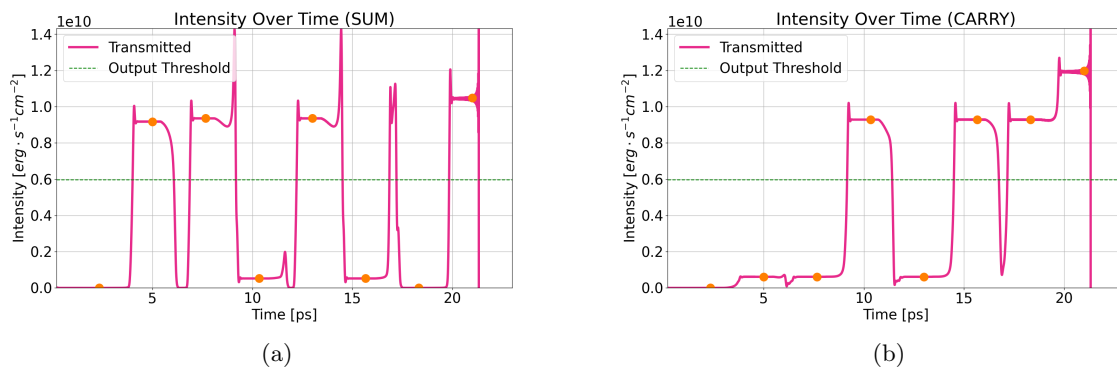


Figure 4.22: Full-adder functionality corresponding to Fig. 4.21 and Table 4.9 with the outputs (transmitted intensities) of (a) the last Fabry-Perot device used to generate the SUM bit of Fig. 4.21 (XOR 2) and (b) the last Fabry-Perot device used to generate the CARRY bit from Fig. 4.21 (the majority gate). The orange dots correspond to the time at which the values are examined for logic values.

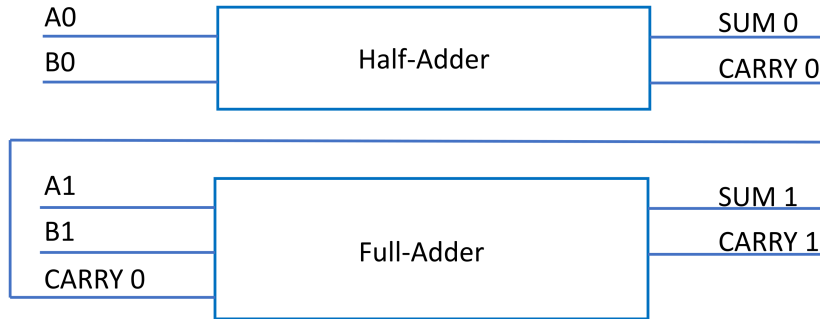


Figure 4.23: 2-bit adder composed of one half-adder (Fig. 4.20) and one full-adder (Fig. 4.21).

Table 4.10: Sample of 2-Bit Adder Logic corresponding to Fig. 4.23

A0	B0	S0	C0	A1	B1	S1	C1
1	1	0	1	0	0	1	0
1	0	1	0	1	1	0	1
1	1	0	1	1	1	1	1
0	1	1	0	1	0	1	0
1	1	0	1	1	0	0	1
0	0	0	0	0	1	1	0
1	1	0	1	0	1	0	1
1	0	1	0	0	0	0	0

together. Any phase shifting from the individual gates can create problems. Particularly important is the case when the XOR gates receive two ‘1’ input signals. These inputs should cancel resulting in a ‘0’ output as in Fig. 4.18. The gate labeled ‘XOR 2’ in Fig. 4.21 is particularly susceptible to phase shifting and magnitude mismatch since it has an input CARRY signal to compare with the XOR of bits A and B. Mitigating solutions will be discussed in a subsequent section.

### 4.2.3 2-BIT ADDER

The 2-bit adder is configured with the same method used in standard circuit design. It uses a half-adder for the first bit and a full-adder for the second bit. The schematic is shown in Fig. 4.23. The half-adder was shown in Fig. 4.20 and the full-adder in Fig. 4.21.

The truth table is shown in Table 4.10. The table lists a sample of inputs that vary the SUM and CARRY bits to maximally stress the intermediate steps. In particular, the XOR gates are all tested with both inputs as ‘1.’ All eight possible inputs to the full adder are included in the table. ‘S0’ refers to SUM bit 0, ‘C0’ refers to CARRY bit 0, and so on. The output SUM and CARRY bits corresponding to Table 4.10 are shown in Fig. 4.24.



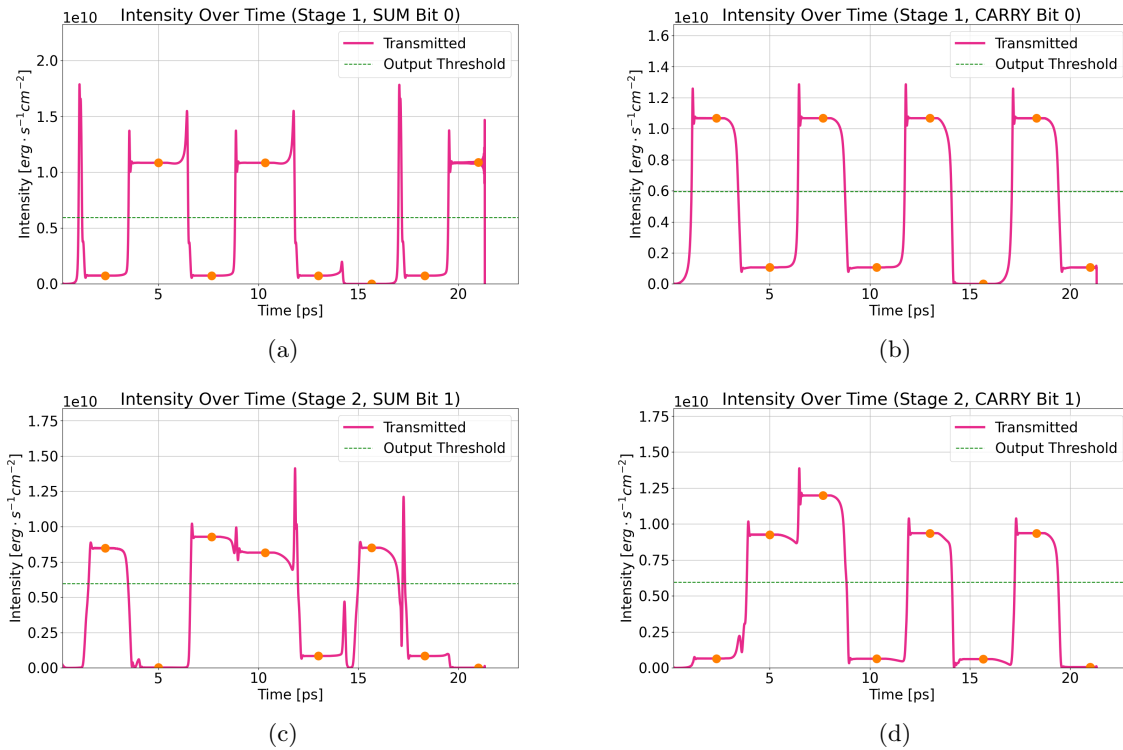


Figure 4.24: 2-bit adder functionality corresponding to Fig. 4.23 and Table 4.10 with the outputs (transmitted intensities) of (a) the last Fabry-Perot device used in the SUM 0 bit generation (XOR in Fig. 4.20), (b) the last Fabry-Perot device used in the CARRY 0 bit generation (AND in Fig. 4.20), (c) the last Fabry-Perot device used in the SUM 1 bit generation (XOR 2 in Fig. 4.21), and (d) the last Fabry-Perot device used in the CARRY 1 bit generation (the majority gate in Fig. 4.21). The orange dots correspond to the time at which the values are examined for logic values. A '1' is above the horizontal green dashed line and a '0' is below the same line.

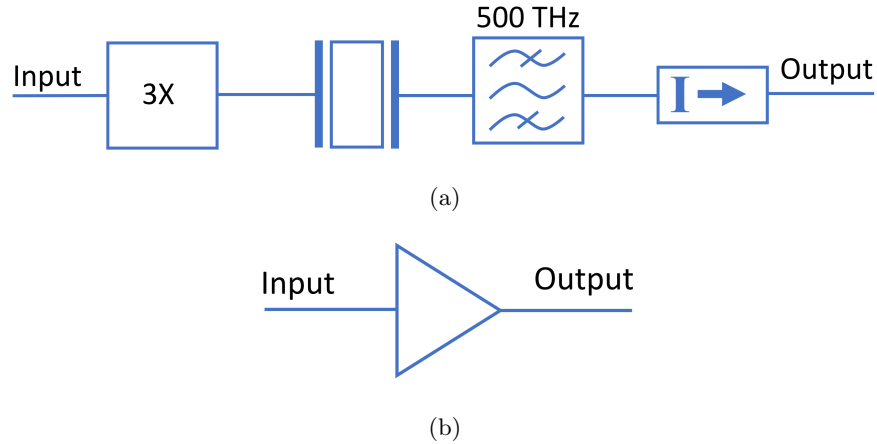


Figure 4.25: (a) Schematic of the buffer including the input amplifier of 3X. (b) The symbol used to represent the schematic of (a).

### 4.3 CHALLENGES AND SOLUTIONS

This section describes some of the potential problems encountered with this technology along with mitigating solutions. Buffering devices are used to standardize the amplitude, standardize the phase, and create desired phase delays. The buffer schematic and symbol are shown in Fig. 4.25. The buffer is similar to that used to buffer the inputs as described in Fig. 4.5, but includes an amplifier. Some possible 2-bit adder designs with buffers are also described in this section.

#### 4.3.1 BUFFERING WITH AMPLITUDE STANDARDIZATION

As previously mentioned, the inputs in Table 4.10 are specifically chosen to maximize the transitions for individual gates as well as ensure each XOR gate receives two '1' inputs during the simulation. The least robust gate is the second XOR gate in the full-adder of Fig. 4.21. This is because that XOR gate ultimately compares outputs that are based on two different types of signals. One signal being compared is the output of the first XOR gate of Fig. 4.21. The other signal is the CARRY bit from the half-adder. The second XOR gate will ideally perfectly cancel out the outputs from the OR and the AND that feed into it. However, this does not always occur because the transmitted magnitudes from the OR and AND gates differ from each other. The AND transmitted magnitude at certain times, even when comparing times at which the outputs all indicate a '0,' will differ. Similarly, the '1' OR transmitted magnitude values at different times will have different magnitudes.

The difference in inputs to the second XOR is unavoidable in this design since the AND and OR gates are built to add intensities together as was seen in Figs. 4.8 and 4.10. These input magnitude differences are shown for OR 2 in Fig. 4.26(a) and for AND 2 in Fig. 4.26(c). The corresponding transmitted

intensities are shown in Fig. 4.26(b) for OR 2 and in Fig. 4.26(d) for AND 2. The transmitted intensities both show a difference in transmitted magnitudes even when comparing transmitted ‘1’ values. The input and transmitted signals for the second XOR are shown in Fig. 4.26(e) and Fig. 4.26(f), respectively.

The input intensities in Fig. 4.26(e) show the wide variety of input intensities. The input intensity at location 4 (at approximately 10.5 ps) is barely above the threshold for a ‘1.’ The input from the OR gate cannot simply be amplified though since that would interfere with the canceling out of the AND input at location 5 (at approximately 13 ps) and at location 7 (at approximately 18 ps), which utilize the XOR gate to cancel out two ‘1’ inputs.

To even out the inputs and make the system more robust, buffer devices can be included. The Fabry-Perot device naturally buffers signals, which can be seen when comparing the input and transmitted intensities in Fig. 4.26. Fig. 4.27 shows the full-adder with two buffers.

The result of using a single buffer after each OR 2 and AND 2 in the full-adder is a more robust full-adder. Fig. 4.28 shows the input and transmitted intensities of the buffers after the second OR and AND gates, as well as the input and transmitted intensities of the XOR gate. There is additional margin built in to the XOR gate when comparing Fig. 4.28(e) to Fig. 4.26(e). Additional buffering devices could further increase the margin for error. For robust functionality, anything registering as a ‘1’ should be well above the dashed green horizontal lines, and a ‘0’ should be well below the horizontal dashed blue lines when looking at input intensities in Figs. 4.26(e) and 4.28(e).

A second buffer device can be added after each buffer of Fig. 4.27. The second buffer further standardizes the transmitted magnitudes that enter the second XOR gate, as shown in Fig. 4.29 for the OR input signal.

### 4.3.2 BUFFERING WITH PHASE STANDARDIZATION

For the logic in this work to function, phase matching is essential. The gates described here utilize either constructive or destructive interference between light signals, so having differing phases is potentially problematic. Since the transmitted signal is measured relative to a mirror as was shown in Fig. 4.1, the phase is predictable depending on the physical location at which the signal is recorded, as was shown in Fig. 4.3. Therefore, the signal can be recorded at a certain cell to minimize the phase shift when comparing transmitted to input intensity.

Regardless of the cell at which the data was saved, there will be a certain amount of phase shift depending on the transmitted intensity. There is a sharp distinction in phase shift depending whether the device is operating below or above the nonlinear threshold. Figure 4.30 shows the relationship between the intensity at the origin and the phase, and the relationship between the transmitted intensity and the phase.

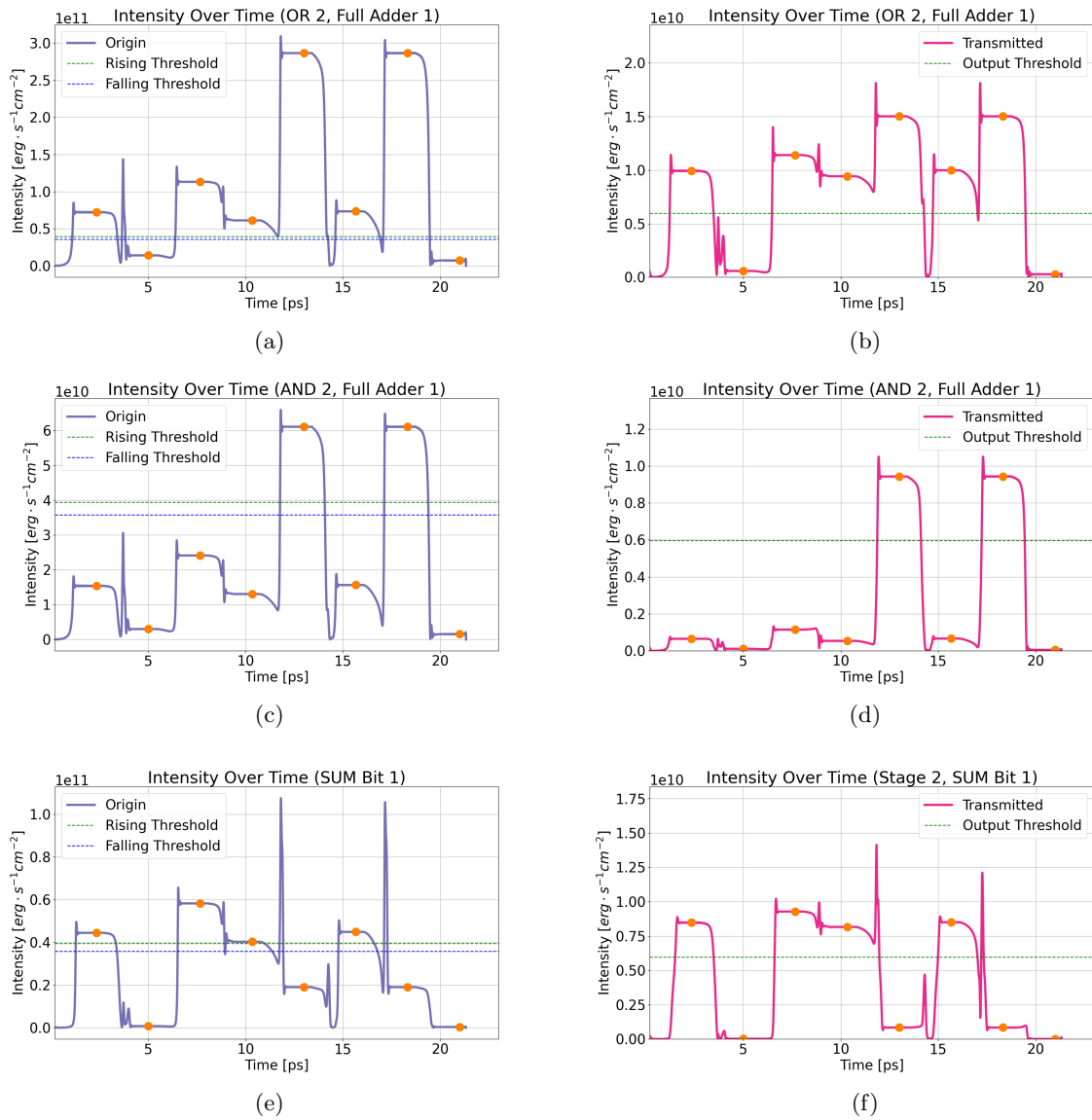


Figure 4.26: The functionality of several devices in Fig. 4.21. The inputs to the full-adder are shown in Table 4.10. This shows (a) the input (post amplification) and (b) the output (transmitted) intensity from the Fabry-Perot device acting as OR 2; (c) the input (post amplification) and (d) the output (transmitted) intensity from the Fabry-Perot device acting as AND 2; and (e) the input (post amplification) and (f) the output (transmitted) intensity from the Fabry-Perot device acting as XOR 2 to generate the SUM bit 1 data. The orange dots correspond to the time at which the magnitudes are examined for logic values. Each value is correct, but the input intensities vary significantly when comparing the ‘1’ values to each other or the ‘0’ values to each other. The result of combining the signals in (b) and (d), and then amplifying them, is shown in (e), which is the input to the Fabry-Perot device representing XOR 2. The intensity at the fourth dot in (e) shows very little margin for being a ‘1’ compared to the intensity at other times because outputs of OR 2 and AND 2 vary significantly from one another. Due to the phase differences, there is also destructive interference on the input at this location.

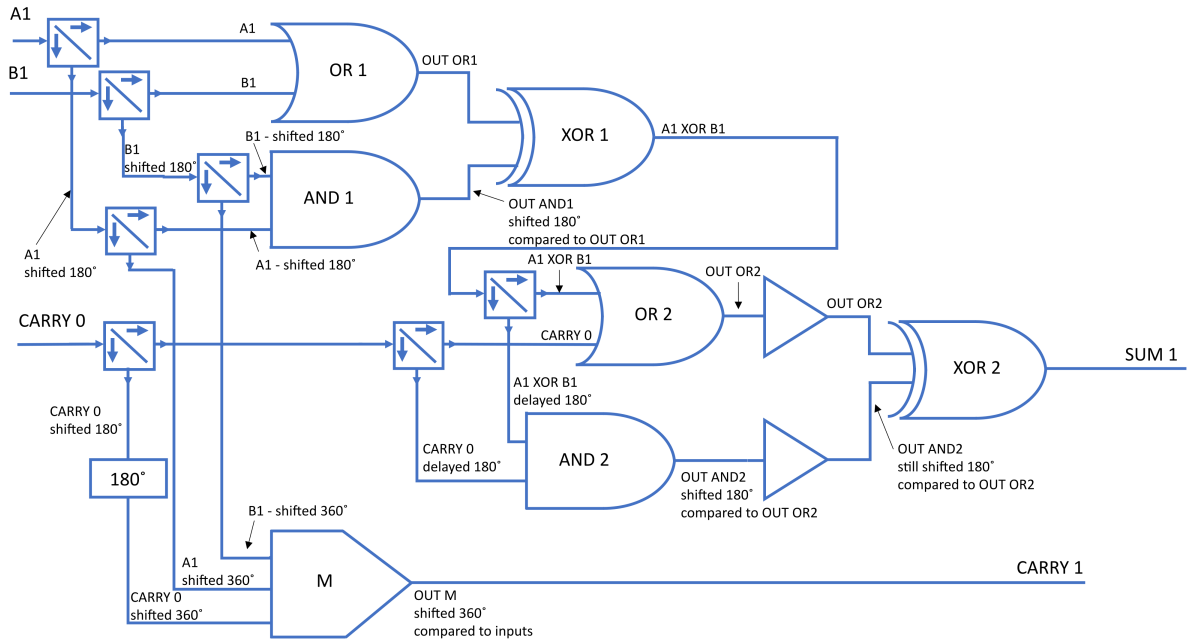


Figure 4.27: Full-adder with two buffers.

Buffer devices, as shown in Fig. 4.27, will help standardize the phase shift in addition to the magnitude. Consistent magnitudes lead to consistent phase shifts.

### 4.3.3 PHASE DELAYS

Time delay components are common in electrical circuits. An equivalent in this type of technology is phase delays. If each device introduces a certain amount of phase shift, buffering devices can be used to create paths of the same length for each signal, allowing the signals to interact in the desired manner. Figure 4.31 shows the path of the CARRY 1 bit in a 2-bit adder with buffers added. One of the inputs to the AND 2 device is the CARRY from the previous stage. If each gate introduces a delay of 0.64 radians, the CARRY 1 signal will marginally fail without the buffers. However, with the buffers, it will clearly pass. These results are shown in Fig. 4.32. Buffering devices can potentially play several important roles in this technology.

### 4.3.4 BUFFER PLACEMENT

There are a number of possibilities for adding buffers to the full-adder circuit. In Fig. 4.27, buffers were added to the second XOR gate inputs. Another possibility is to add the buffers prior to the OR 2 and AND 2 gates, as shown in Fig. 4.33. This will standardize the output of the first XOR gate and the CARRY bit from the previous stage.

The advantage to this is that, as previously described, the outputs will be standardized in both phase

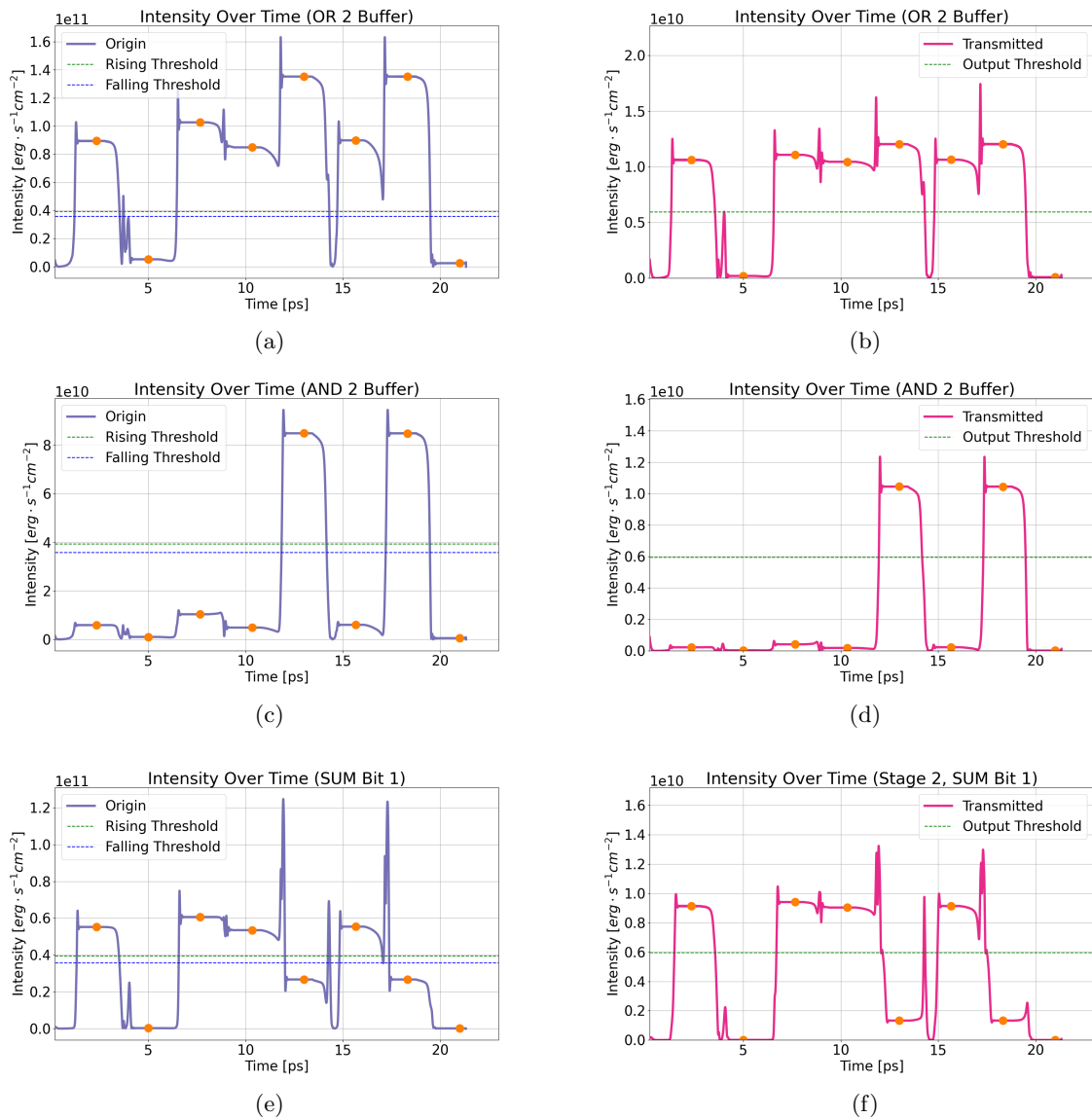


Figure 4.28: The functionality of several devices corresponding to Fig. 4.27. The inputs to the full-adder are shown in Table 4.10. This shows (a) the input (post amplification) and (b) the output (transmitted) intensity from the Fabry-Perot device acting as the buffer after OR 2; (c) the input (post amplification) and (d) the output (transmitted) intensity from the Fabry-Perot device acting as the buffer after AND 2; and (e) the input (post amplification) and (f) the output (transmitted) intensity from the Fabry-Perot device acting as XOR 2 to generate the SUM bit 1 data. The orange dots correspond to the time at which the magnitudes are examined for logic values. The margin in (e) is improved compared to Fig. 4.26(e), particularly when looking at location 4 (at approximately 10.5 ps).

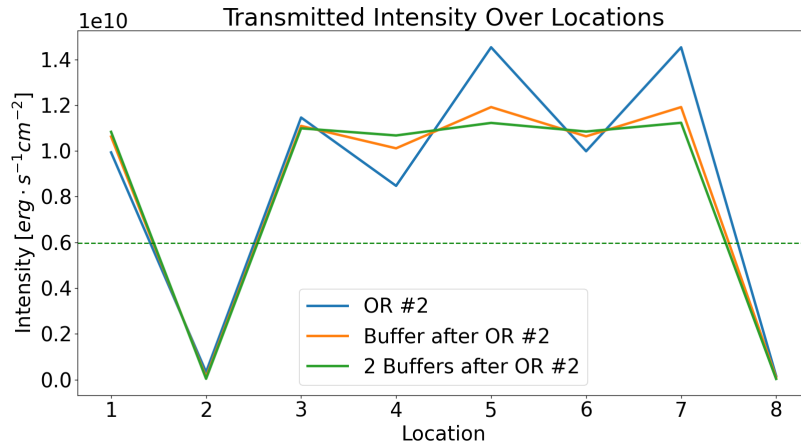


Figure 4.29: The intensity transmitted from the second OR gate of the full-adder and through two subsequent series buffers. Each additional buffer causes the output ‘1’ levels to be more consistent. The intensity is recorded at the eight times indicated by dots in Fig. 4.26(b).

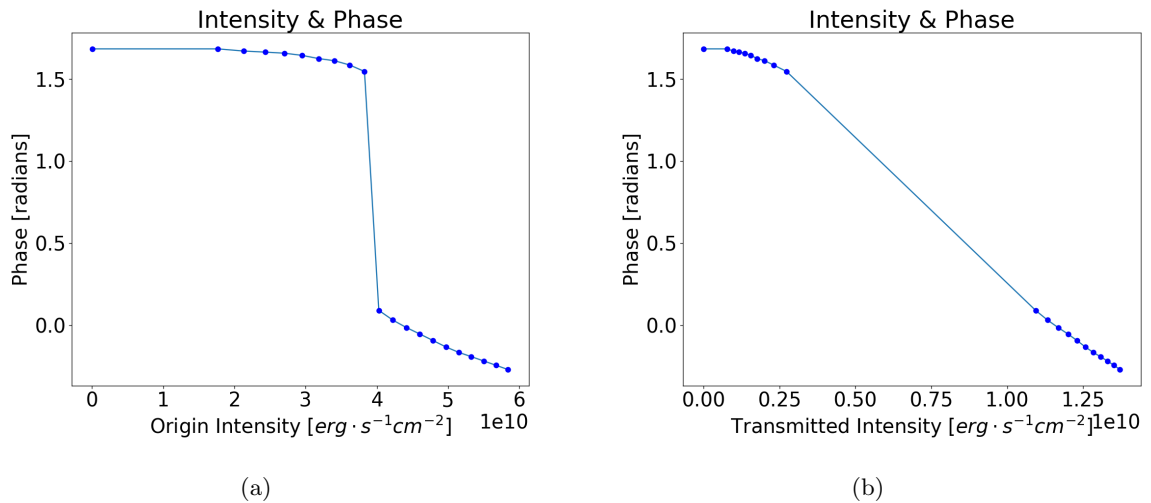


Figure 4.30: The phase versus (a) the intensity (post amplification) at the origin and (b) the intensity transmitted. There is a significant difference in phase when looking at input intensities above versus below the nonlinear threshold. The phase ranges between 1.54 and 1.68 radians when the signal is below the nonlinear threshold (representing a ‘0’) compared to between -0.27 and 0.09 radians when the signal is above the nonlinear threshold (representing a ‘1’). The difference in the phases above and below the nonlinear threshold explains why destructive interference can occur when combining signals.

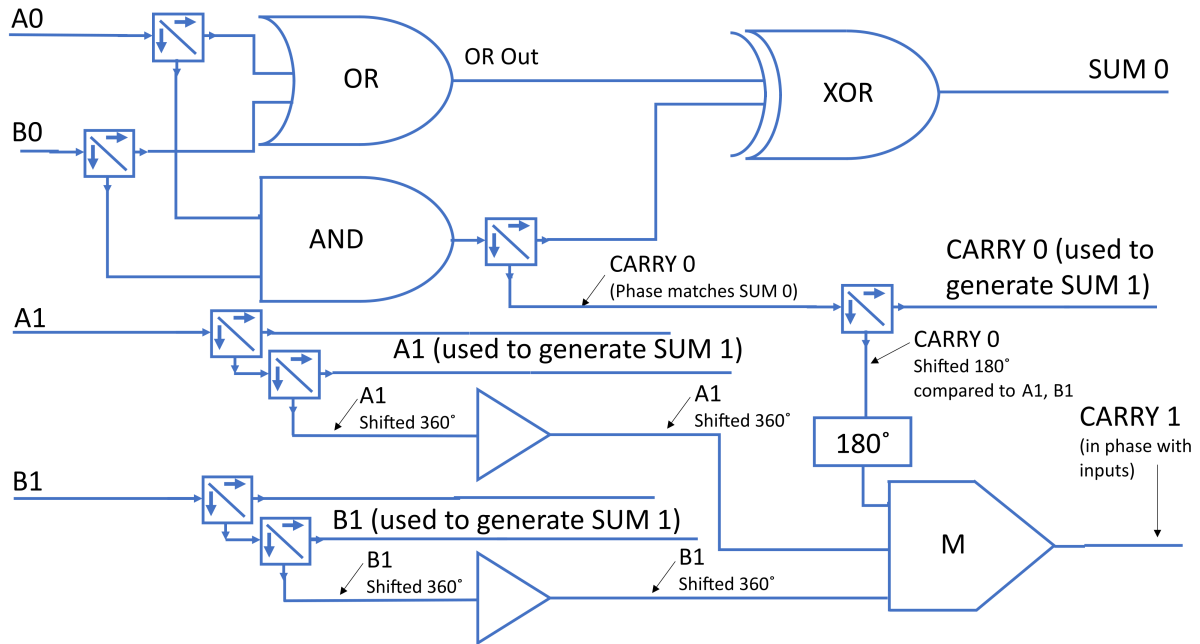


Figure 4.31: 2-bit adder CARRY 1's path with buffers.

and amplitude. Even though the transmitted intensity is clearly either a '0' or a '1,' there is a difference in the levels of each binary option. This means the phase can also differ, as was shown in Fig. 4.30. Figure 4.34 shows the input and transmitted intensity related to the Fabry-Perot device acting as the XOR 2 gate of the full-adder without buffers in Fig. 4.21. The input is post amplification. Fig. 4.35 shows a sample of the input electric fields relative to a reference sinusoid.

Looking at the inputs of of Table 4.10, the interaction for the fourth input, at the time represented by the fourth orange dot in Fig. 4.34, should be (and is) a '1,' However, as shown by the time varying electric field in Figs. 4.35(b) and 4.35(d), there is introduced phase shift. This ultimately reduces their combined input. Though it is still a '1,' the margin is less than expected as shown in Fig. 4.36 at the fourth dot.

Using the buffers of Fig. 4.33 reduces this problem as seen in Fig. 4.37. Fig. 4.38 can be compared to Fig. 4.35 showing a reduction in the electric field for the '0' values.



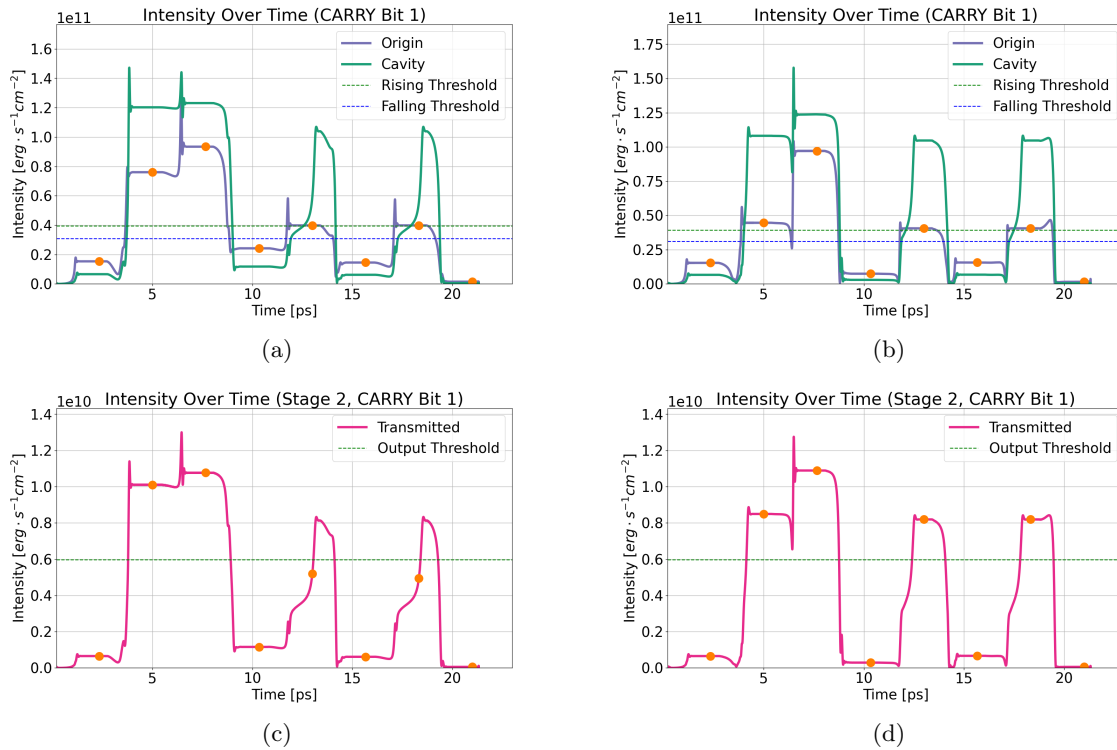


Figure 4.32: The input and transmitted intensities for the Fabry-Perot device used as a majority gate to generate the CARRY 1 signal. The inputs are the same as in Table 4.10, but each device intentionally creates a phase shift of 0.64 radians. The origin intensity (post amplification) and the cavity intensity (a) without any buffers and (b) with the buffers as shown in Fig. 4.31. The CARRY 1 output (transmitted) signal alone is shown for the circuit (c) without any buffers and (d) with the buffers as shown in Fig. 4.31. Without the buffers, the output (transmitted) signal marginally fails at the 5th and 7th locations shown in (c), but it clearly passes with the additional buffers as shown in (d).

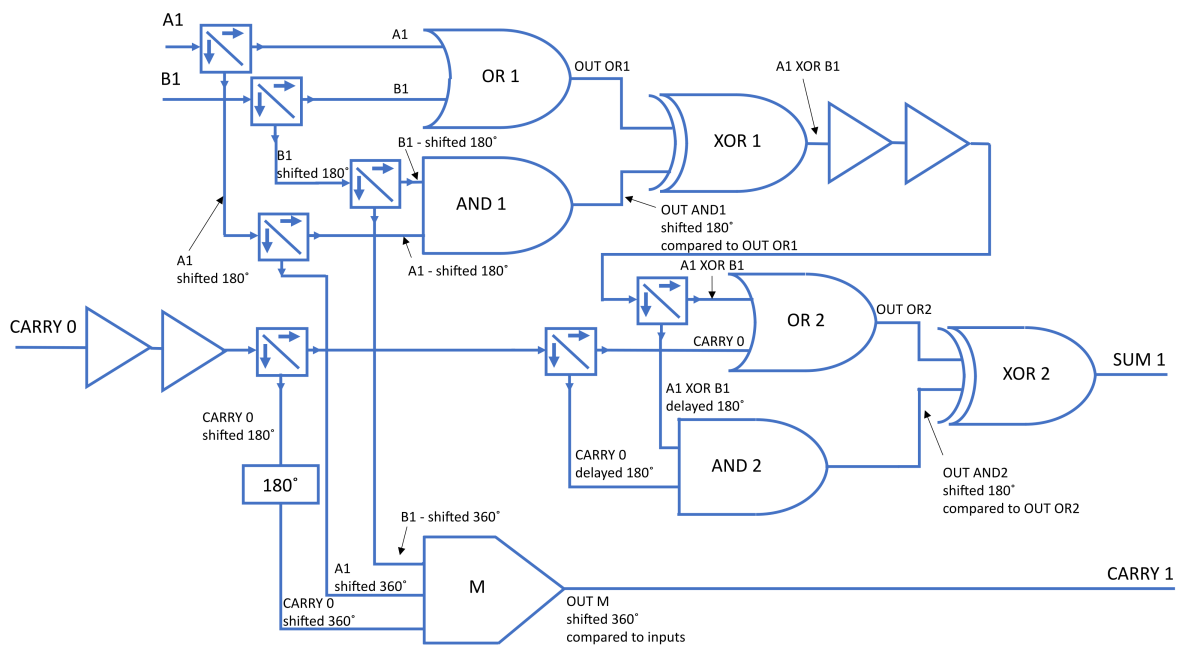


Figure 4.33: Full-adder with four buffers added. Two buffers are added to each input of the second OR, which are also the inputs to the second AND gate.

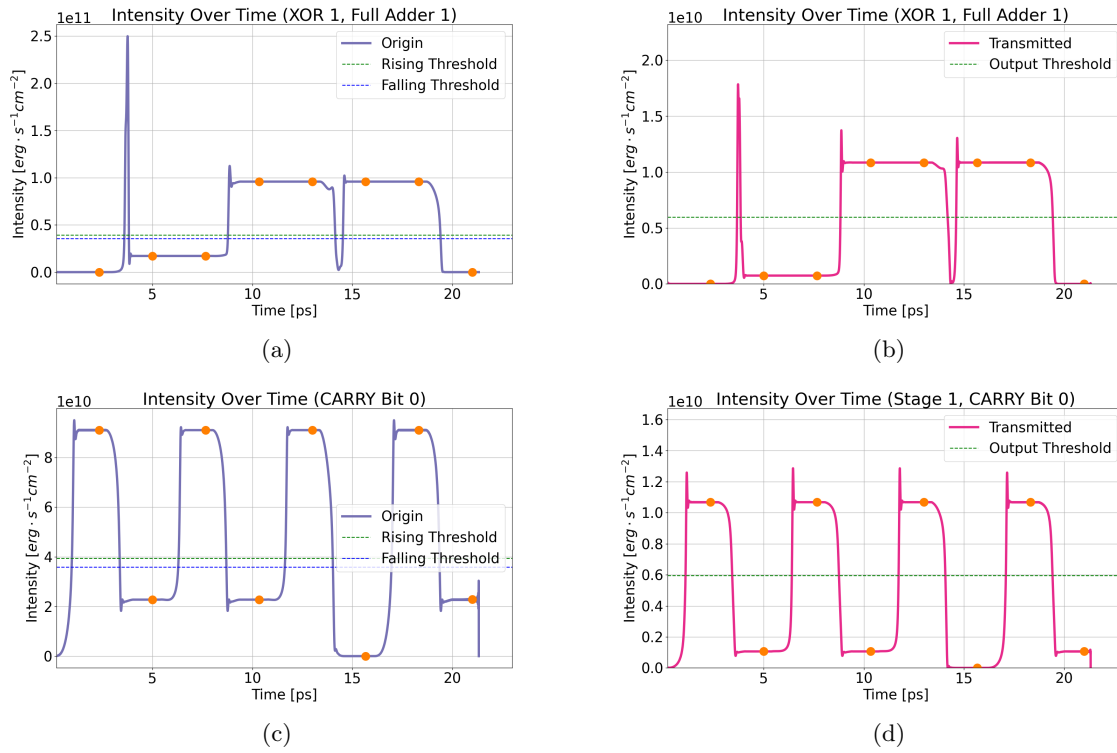


Figure 4.34: The (a) the input (post amplification) to the Fabry-Perot device acting as the XOR 1 gate and (b) its corresponding output. The (c) the input (post amplification) to the Fabry-Perot device acting as the AND gate of the half-adder to generate the CARRY 0 bit and (d) its corresponding output. The outputs of (b) and (d) act as inputs to the second OR gate of the full-adder. Although the transmitted intensities can be clearly identified in (b) and (d) as '0' or '1,' the '0' values are not at exactly zero and therefore have a phase shift associated with them. This is a simulation of the full-adder without buffers.

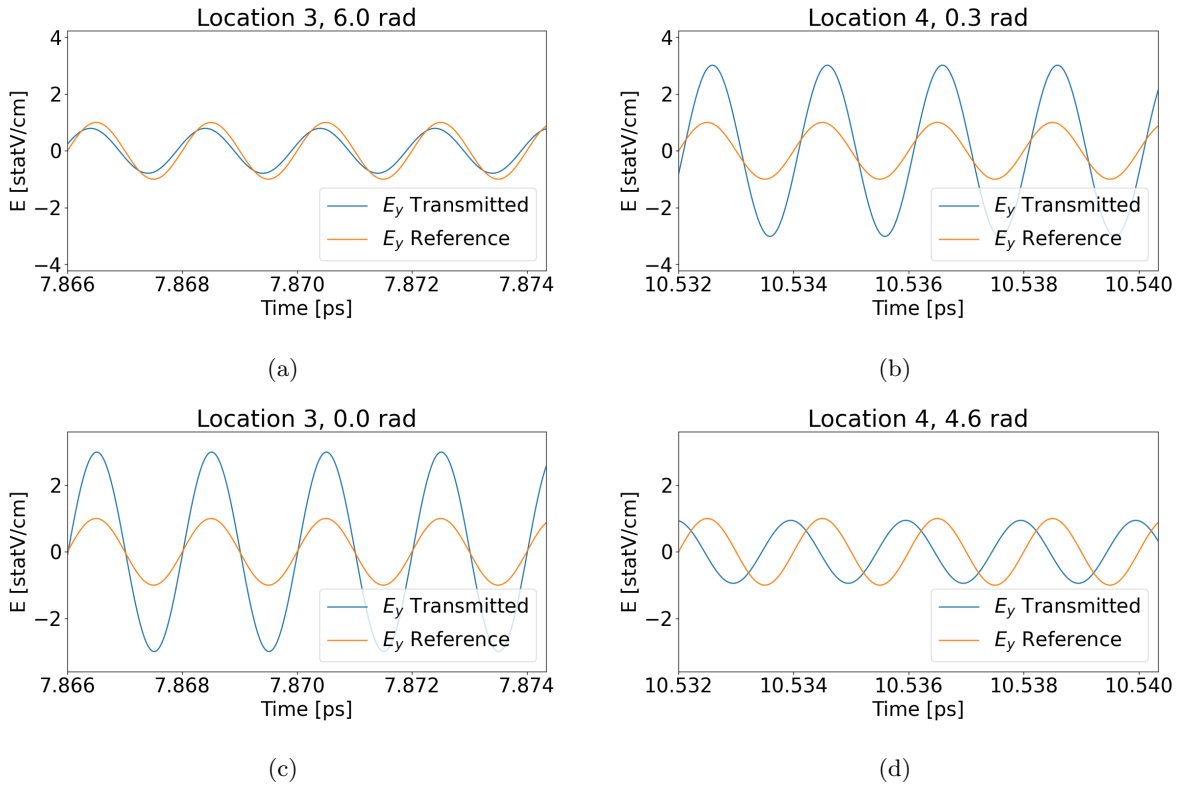


Figure 4.35: The input electric fields to the OR 2 gate of the full-adder without buffers given with respect to a reference signal at the time of (a) the third dot of the transmitted XOR 1 signal in Fig. 4.34(b), (b) the fourth dot of the transmitted XOR 1 signal in Fig. 4.34(b), (c) the third dot of the transmitted CARRY signal in Fig. 4.34(d), (d) the fourth dot of the transmitted CARRY signal in Fig. 4.34(d). Although the signals of (a) and (d) both represent a logic ‘0,’ these do not have amplitudes of zero. The phase shift of (d) can interact with the signal shown in (b) to reduce the combined input to the subsequent OR and AND gates.

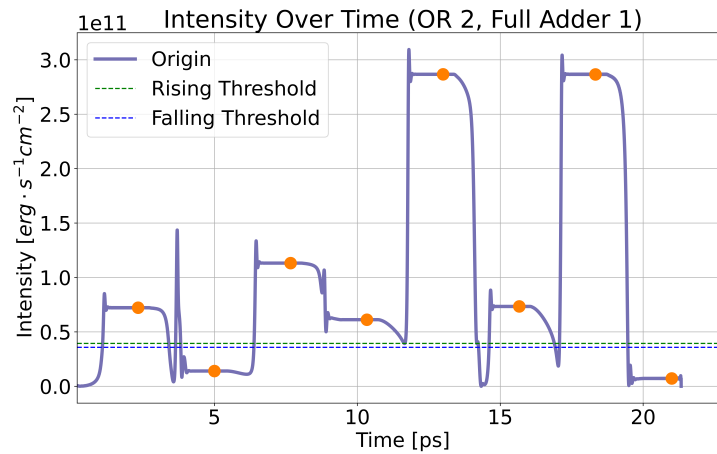


Figure 4.36: The input intensity to the OR 2 gate of the full-adder without buffers. There is little margin at the fourth dot around 10.5 ps due to the destructive interference of the phase-shifted zero input of Fig. 4.35(d).

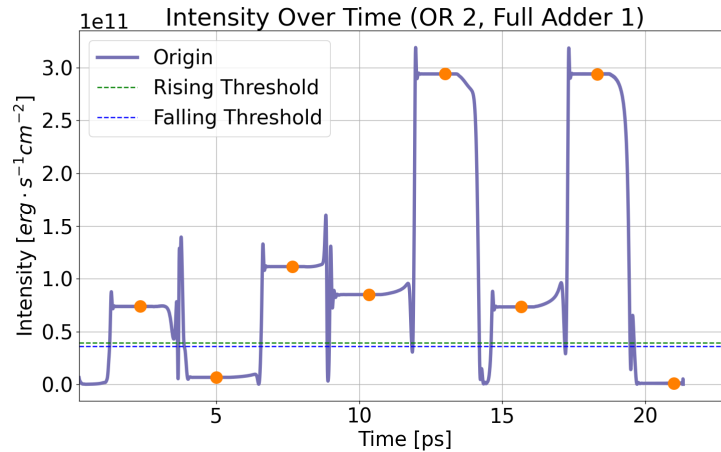


Figure 4.37: The input intensity to the OR 2 gate of the full-adder with two buffers as in Fig. 4.33. There is far more margin at the fourth dot around 10.5 ps compared to the fourth dot in Fig. 4.36.

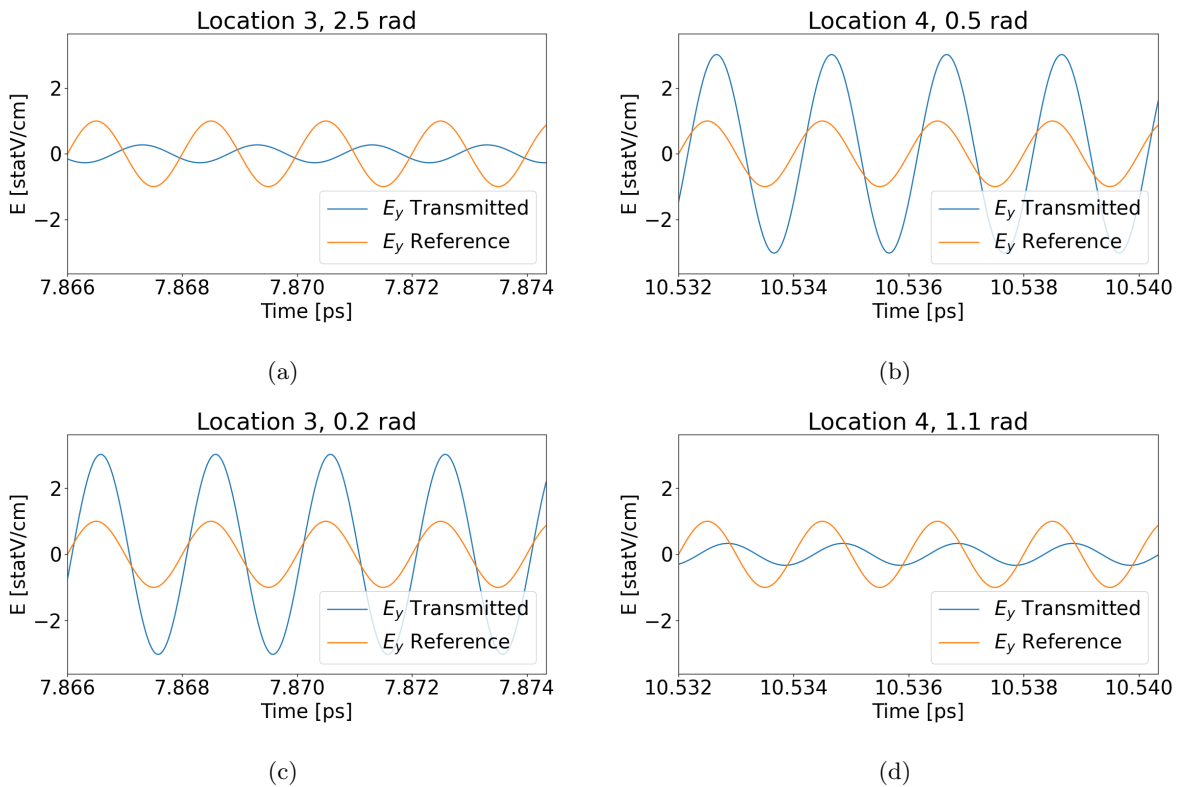


Figure 4.38: Adding buffers, as in Fig. 4.33, this shows the input electric fields to the second OR gate of the full-adder, given with respect to a reference signal, at the time of (a) the third dot of the buffered XOR 1 signal in Fig. 4.34(b), (b) the fourth dot of the buffered XOR 1 signal in Fig. 4.34(b), (c) the third dot of the buffered CARRY signal in Fig. 4.34(d), (d) the fourth dot of the buffered CARRY signal signal in Fig. 4.34(d). The signals of (a) and (d) representing input 0's are smaller than those in Fig. 4.35, creating less potential problems with destructive interference.

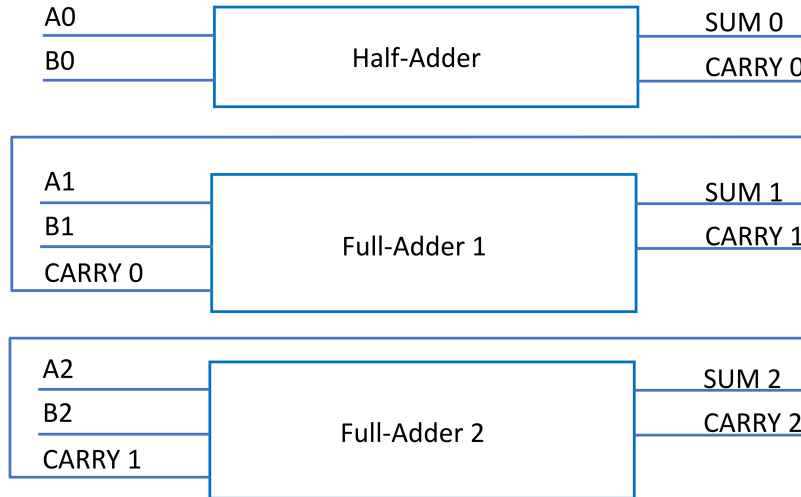


Figure 4.39: 3-bit adder composed of one half-adder and two full-adders.

## 4.4 3-BIT AND 4-BIT ADDERS

This section shows how the 2-bit adder design previously described can be expanded to the 3-bit and the 4-bit adder. The results are those expected, showing these devices can be cascaded.

### 4.4.1 3-BIT ADDER

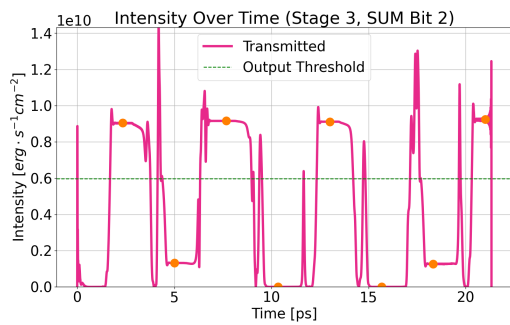
The 3-bit adder is an extension of the 2-bit adder. It simply connects another full-adder to the 2-bit adder's CARRY bit. Due to the previously described phase shifts and amplitude variation, the full-adder with buffers of Fig. 4.33 will be used when constructing the 3-bit adder. Superior performance can be achieved with additional buffers, but this combination was used as a compromise between performance and efficiency in the number of devices used for a full-adder.

The schematic is shown in Fig. 4.39. The half-adder was shown in Fig. 4.20 and the full-adder with buffers in Fig. 4.33. The truth table is shown in Table 4.11. The table lists a sample of inputs that vary the SUM and CARRY bits to maximally stress the intermediate steps. In particular, the XOR gates are all tested with both inputs as '1.' Each possible input to Full-Adder 2 is also included. 'S2' refers to SUM bit 2, 'C2' refers to CARRY bit 2, and so on. The output SUM 2 and CARRY 2 bits corresponding to Table 4.11 are shown in Fig. 4.40. These outputs all show the expected results.

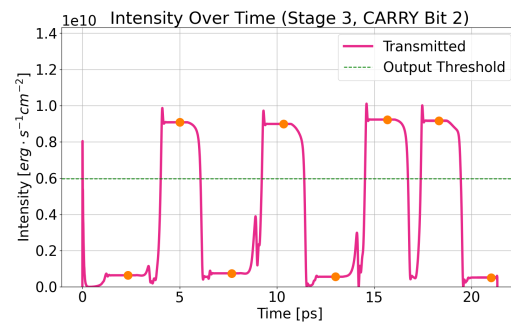
These results are not as clean-looking as those in prior plots. To improve the functionality, the device could be adjusted for better optical bistability by adjusting the cavity length and the Lorentz parameters. Additional buffering devices could be used, or the simulation time could be extended to make the transients occupy a smaller percentage of the simulation time.

Table 4.11: 3-Bit Adder Logic corresponding to Fig. 4.39

A2	B2	C1	XOR1	OR2	AND2	S2	C2
1	0	0	1	1	0	1	0
0	1	1	1	1	1	0	1
0	0	1	0	1	0	1	0
1	1	0	0	0	0	0	1
0	0	1	0	1	0	1	0
1	1	0	0	0	0	0	1
0	1	1	1	1	1	0	1
1	0	0	1	1	0	1	0



(a)



(b)

Figure 4.40: 3-bit adder functionality corresponding to Fig. 4.39 and Table 4.11 with the outputs of (a) the SUM 2 bit and (b) the CARRY 2 bit. The orange dots correspond to the time at which the values are examined for logic values. A ‘1’ is above the horizontal green dashed line and a ‘0’ is below the same line. The outputs for S0, S1, C0, and C1 were shown in Fig. 4.24, with C1 being an input to the third stage of the adder.

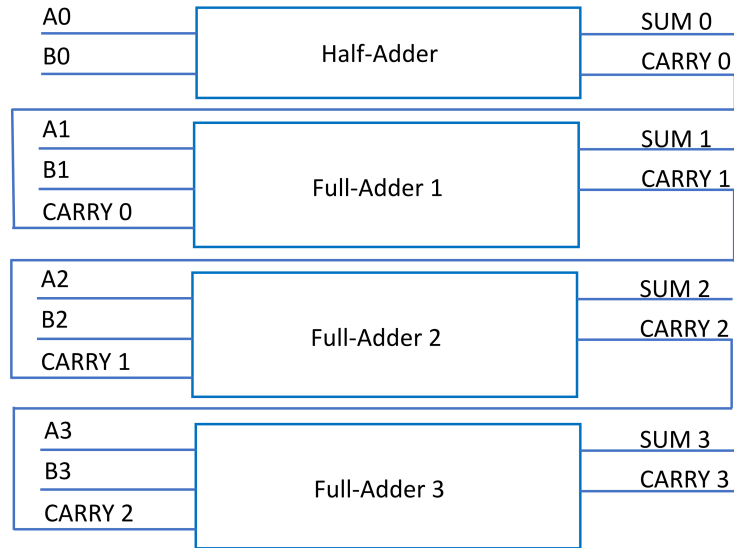


Figure 4.41: 4-bit adder composed of one half-adder and three full-adders.

Table 4.12: 4-Bit Adder Logic corresponding to Fig. 4.41

A3	B3	C2	XOR1	OR2	AND2	S3	C3
1	0	0	1	1	0	1	0
0	1	1	1	1	1	0	1
0	0	0	0	0	0	0	0
1	1	1	0	1	0	1	1
0	0	0	0	0	0	0	0
1	1	1	0	1	0	1	1
0	1	1	1	1	1	0	1
1	0	0	1	1	0	1	0

#### 4.4.2 4-BIT ADDER

The 4-bit adder adds an additional full-adder to the 3-bit adder previously described. The schematic is shown in Fig. 4.41. The half-adder was shown in Fig. 4.20 and the full-adder with buffers in Fig. 4.33. The truth table is shown in Table 4.12. The table lists a sample of inputs that vary the SUM and CARRY bits again to maximally stress the intermediate steps. In particular, the XOR gates are all tested with both inputs as '1.' Each possible input to Full-Adder 3 are included. 'S3' refers to SUM bit 3, 'C3' refers to CARRY bit 3, and so on. The output SUM 3 and CARRY 3 bits corresponding to Table 4.12 are shown in Fig. 4.42. The outputs are all as expected.



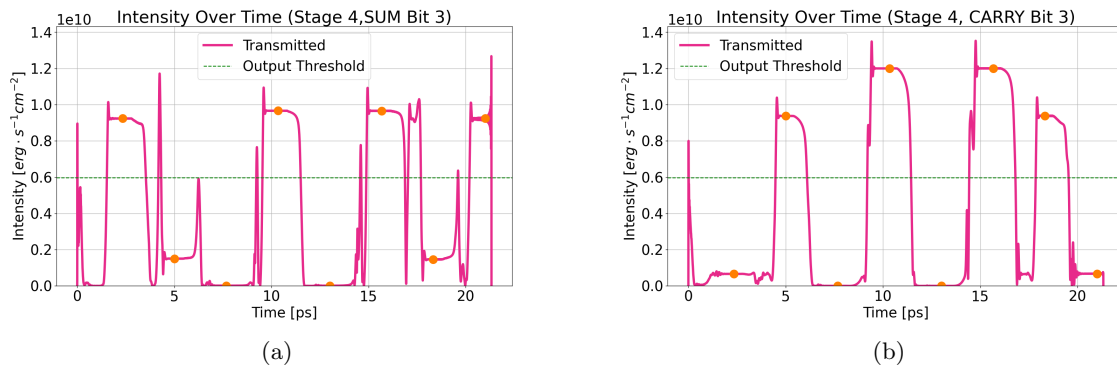


Figure 4.42: 4-bit adder functionality corresponding to Fig. 4.41 and Table 4.12 with the outputs of (a) the SUM 3 bit, (b) the CARRY 3 bit. The orange dots correspond to the time at which the values are examined for logic values. A '1' is above the horizontal green dashed line and a '0' is below the same line. The outputs for S0, S1, C0, and C1 were shown in Fig. 4.24, and S2 and C2 were shown in Fig. 4.40, with C2 being an input to the fourth stage of the adder.

## CHAPTER 5: CONCLUSIONS

This work describes the use of the FDTD method to model complex, nonlinear materials, with a focus on simulating a Fabry-Perot device. A cavity is created using DR1-PMMA characteristics and surrounded by highly reflective silver plasma mirrors. The cavity is approximately three wavelengths long using an input 500 THz signal. The behavior of the device is explored and characterized.

The optically bistable nature of the Fabry-Perot device described makes it a promising candidate for building optical logic circuits that are analogous to classical electrical logic. Basic logic gates, such as AND, OR, and XOR gates, can be created using these devices. Furthermore, these gates can be combined to create adders, including multi-bit adders. The 4-bit adder demonstrated the expected functionality, showing that these adders can be cascaded while maintaining their functionality. The logic for the 4-bit adder runs on the equivalent of a 2.67 ps clock, indicating that the response time of these devices is extremely fast.

Unwanted phase shifting is expected to be a major limitation of this technology. The manufacturing of these optical circuits will require extreme precision. Some phase shifting and amplitude modulation will be possible through the use of buffering devices. Some investigation of buffering devices, including their placement and effects, was presented here. There are many possibilities for future experimentation in this area.

In addition to using more buffering devices, the functionality of the 4-bit adder could be improved by adjusting the Lorentz parameters. The cavity length can also be adjusted to enhance the bistable characteristics of the devices.

This technology provides a novel optical logic device that can interact with other purely optical components, enabling the implementation of current digital logic designs in optical computers. Given the numerous advantages of optical computers, such as speed and power efficiency, investigating optical logic is essential in creating the next generation of computers. These devices could bring purely optical computers one step closer to becoming a reality.

## REFERENCES

- [1] Pierre Ambs. “Optical Computing: A 60-Year Adventure.” In: *Advances in Optical Technologies* (2010).
- [2] Kamanashis Goswami, Haraprasad Mondal, and Mrinal Sen. “A review on all-optical logic adder: Heading towards next-generation processor”. In: *Optics Communications* 483 (2021), p. 126668.
- [3] Brian Guiana and Ata Zadehgol. “Characterizing THz scattering loss in nano-scale SOI waveguides exhibiting stochastic surface roughness with exponential autocorrelation”. In: *Electronics* 11.3 (2022), p. 307.
- [4] Chris Mack. “The Multiple Lives of Moore’s Law”. In: *IEEE Spectrum* 52.4 (2015), pp. 31–31. DOI: 10.1109/MSPEC.2015.7065415.
- [5] Rachel Courtland. “Transistors could stop shrinking in 2021”. In: *IEEE Spectrum* 53.9 (2016), pp. 9–11. DOI: 10.1109/MSPEC.2016.7551335.
- [6] Brian Cline et al. “Next-Gen Chips will be Powered from Below”. In: *IEEE Spectrum* (Aug. 26, 2021). URL: <https://spectrum.ieee.org/next-gen-chips-will-be-powered-from-below> (visited on 08/26/2021).
- [7] Rina Diane Caballar. “Here’s How AI Will Change Chip Design”. In: *IEEE Spectrum* (Aug. 2, 2022). URL: <https://spectrum.ieee.org/ai-chip-design-matlab> (visited on 08/02/2022).
- [8] Sajjad Abdollahramezani, Omid Hemmatyar, and Ali Adibi. “Meta-optics for spatial optical analog computing”. In: *Nanophotonics* 9.13 (2020), pp. 4075–4095.
- [9] Jiamin Wu et al. “Analog optical computing for artificial intelligence”. In: *Engineering* (2021).
- [10] PG Kasherininov and AA Tomasov. “High-throughput optical processors based on semiconductor nanostructures for incoherent-light optical analog computers with parallel image processing”. In: *Technical Physics Letters* 34.4 (2008), pp. 350–353.
- [11] Nikolay L Kazanskiy, Muhammad A Butt, and Svetlana N Khonina. “Optical Computing: Status and Perspectives”. In: *Nanomaterials* 12.13 (2022), p. 2171.
- [12] Sumit Sharma and Sudip Roy. “A survey on design and synthesis techniques for photonic integrated circuits”. In: *The Journal of Supercomputing* 77.5 (2021), pp. 4332–4374.
- [13] Amir H Atabaki et al. “Integrating photonics with silicon nanoelectronics for the next generation of systems on a chip”. In: *Nature* 556.7701 (2018), pp. 349–354.

- [14] Ke Liu et al. “Review and perspective on ultrafast wavelength-size electro-optic modulators”. In: *Laser & Photonics Reviews* 9.2 (2015), pp. 172–194.
- [15] SungWon Chung, Makoto Nakai, and Hossein Hashemi. “Low-power thermo-optic silicon modulator for large-scale photonic integrated systems”. In: *Optics express* 27.9 (2019), pp. 13430–13459.
- [16] Zhihong Li and Guifang Li. “Ultrahigh-speed reconfigurable logic gates based on four-wave mixing in a semiconductor optical amplifier”. In: *IEEE Photonics Technology Letters* 18.12 (2006), pp. 1341–1343.
- [17] Jingya Xie et al. “Ultracompact all-optical full-adder and half-adder based on nonlinear plasmonic nanocavities”. In: *Nanophotonics* 6.5 (2017), pp. 1161–1173.
- [18] Mohsen Olyaei, Mohammad Bagher Tavakoli, and Abbas Mokhtari. “Propose, Analysis and Simulation of an All Optical Full Adder Based on Plasmonic Waves using Metal-Insulator-Metal Waveguide Structure”. In: *Journal of Optoelectronic Nanostructures* 4.3 (2019), pp. 95–116.
- [19] Somayyeh Asgari, Nosrat Granpayeh, and Zahra Ghattan Kashani. “Plasmonic mid-infrared wavelength selector and linear logic gates based on graphene cylindrical resonator”. In: *IEEE Transactions on Nanotechnology* 18 (2018), pp. 42–50.
- [20] Saif Hasan Abdalnabi and Mohammed Nadhim Abbas. “Design an all-optical combinational logic circuits based on nano-ring insulator-metal-insulator plasmonic waveguides”. In: *Photonics*. Vol. 6. MDPI. 2019, p. 30.
- [21] Deeksha Rani, Rajinder Singh Kaler, and Balveer Painam. “All-optical NOR gate based on cross structures in 2D photonic crystal using logic NOT and OR gates”. In: *Journal of Optical Technology* 84.12 (2017), pp. 851–857.
- [22] Kouddad Elhachemi et al. “Performance evaluation of all-optical NOT, XOR, NOR, and XNOR logic gates based on 2D nonlinear resonant cavity photonic crystals”. In: *Optical and Quantum Electronics* 53.12 (2021), pp. 1–15.
- [23] Parisa Andalib and Nosrat Granpayeh. “All-optical ultracompact photonic crystal AND gate based on nonlinear ring resonators”. In: *JOSA B* 26.1 (2009), pp. 10–16.
- [24] Man Mohan Gupta and Sarang Medhekar. “All-optical NOT and AND gates using counter propagating beams in nonlinear Mach-Zehnder interferometer made of photonic crystal waveguides”. In: *Optik* 127.3 (2016), pp. 1221–1228.
- [25] Hamed Alipour-Banaei, Somaye Serajmohammadi, and Farhad Mehdizadeh. “All optical NOR and NAND gate based on nonlinear photonic crystal ring resonators”. In: *Optik* 125.19 (2014), pp. 5701–5704.

- [26] Aref Rahmani and Mehrnoush Asghari. “An ultra-compact and high speed all optical OR/NOR gate based on nonlinear PhCRR”. In: *Optik* 138 (2017), pp. 314–319.
- [27] Alok Kumar and Sarang Medhekar. “All optical NOR and NAND gates using four circular cavities created in 2D nonlinear photonic crystal”. In: *Optics & Laser Technology* 123 (2020), p. 105910.
- [28] Zhi-Hong Zhu et al. “High-contrast light-by-light switching and AND gate based on nonlinear photonic crystals”. In: *Optics Express* 14.5 (2006), pp. 1783–1788.
- [29] P Andalib and N Granpayeh. “All-optical ultra-compact photonic crystal NOR gate based on nonlinear ring resonators”. In: *Journal of Optics A: Pure and Applied Optics* 11.8 (2009), p. 085203.
- [30] Somaye Serajmohammadi and Hassan Absalan. “All optical NAND gate based on nonlinear photonic crystal ring resonator”. In: *Information processing in Agriculture* 3.2 (2016), pp. 119–123.
- [31] Golnaz Tavakoli, Hamed Alipour-Banaei, and Mahdi Hassangholizadeh-Kashtiban. “A novel proposal for all-optical compact and fast XOR/XNOR gate based on photonic crystal”. In: *Journal of Modern Optics* 66.6 (2019), pp. 599–605.
- [32] Yaw-Dong Wu, Tien-Tsorng Shih, and Mao-Hsiung Chen. “New all-optical logic gates based on the local nonlinear Mach-Zehnder interferometer”. In: *Optics Express* 16.1 (2008), pp. 248–257.
- [33] M Tajaldini and MZ Jafri. “Simulation of all-optical NOT/OR/AND/NAND/NOR/XNOR/XOR logic gates using a single structure high contrast index nonlinear multimode interference coupler”. In: *Physica Scripta* 94.10 (2019), p. 105004.
- [34] F Cheraghi, M Soroosh, and G Akbarizadeh. “An ultra-compact all optical full adder based on nonlinear photonic crystal resonant cavities”. In: *Superlattices and Microstructures* 113 (2018), pp. 359–365.
- [35] Mohamed Nady Abdul Aleem, Khalid Fawzy Ahmed Hussein, et al. “Ultrafast all-optical full adder using quantum-dot semiconductor optical amplifier-based mach-zehnder interferometer”. In: *Progress In Electromagnetics Research B* 54 (2013), pp. 69–88.
- [36] Jianji Dong et al. “Single SOA based all-optical adder assisted by optical bandpass filter: Theoretical analysis and performance optimization”. In: *Optics communications* 270.2 (2007), pp. 238–246.
- [37] Mona Neisy, Mohammad Soroosh, and Karim Ansari-Asl. “All optical half adder based on photonic crystal resonant cavities”. In: *Photonic Network Communications* 35.2 (2018), pp. 245–250.
- [38] Tobias Birr et al. “Ultrafast surface plasmon-polariton logic gates and half-adder”. In: *Optics express* 23.25 (2015), pp. 31755–31765.

- [39] Qiang Liu et al. “All-optical half adder based on cross structures in two-dimensional photonic crystals”. In: *Optics express* 16.23 (2008), pp. 18992–19000.
- [40] Saghar Sadegh-Bonab and Hamed Alipour-Banaei. “A novel proposal for an all-optical 2-bit adder/subtractor based on photonic crystal ring resonators”. In: *Photonics and Nanostructures-Fundamentals and Applications* 39 (2020), p. 100777.
- [41] Ranran Fan et al. “2D photonic crystal logic gates based on self-collimated effect”. In: *Journal of Physics D: Applied Physics* 49.32 (2016), p. 325104.
- [42] Andy Eu-Jin Lim et al. “Review of silicon photonics foundry efforts”. In: *IEEE Journal of Selected Topics in Quantum Electronics* 20.4 (2013), pp. 405–416.
- [43] MG Kuzyk, UC Paek, and CW Dirk. “Guest-host polymer fibers for nonlinear optics”. In: *Applied physics letters* 59.8 (1991), pp. 902–904.
- [44] DJ Welker and MG Kuzyk. “Optical and mechanical multistability in a dye-doped polymer fiber Fabry-Perot waveguide”. In: *Applied physics letters* 66.21 (1995), pp. 2792–2794.
- [45] DJ Welker and MG Kuzyk. “All-optical switching in a dye-doped polymer fiber Fabry-Perot waveguide”. In: *Applied physics letters* 69.13 (1996), pp. 1835–1836.
- [46] Shaoping Bian, Dirk Robinson, and Mark G Kuzyk. “Optically activated cantilever using photomechanical effects in dye-doped polymer fibers”. In: *JOSA B* 23.4 (2006), pp. 697–708.
- [47] Xianjun Ye and Mark G Kuzyk. “Photomechanical response of disperse red 1 azobenzene dye-doped PMMA polymer fiber”. In: *Optics Communications* 312 (2014), pp. 210–215.
- [48] Bojun Zhou et al. “Theoretical and experimental studies of photomechanical materials”. In: *JOSA B* 36.6 (2019), pp. 1492–1517.
- [49] Mark G Kuzyk. *Nonlinear optics: a student’s perspective with Python problems and examples*. CreateSpace Independent Publishing Platform, 2017.
- [50] Kane Yee. “Numerical solution of initial boundary value problems involving Maxwell’s equations in isotropic media”. In: *IEEE Transactions on antennas and propagation* 14.3 (1966), pp. 302–307.
- [51] Allen Taflov and Susan Hagness. *Computational electrodynamics: the finite-difference time-domain method, third edition*. Artech House Publishers, 2005.
- [52] Constantine A Balanis. *Advanced engineering electromagnetics*. John Wiley & Sons, 2012.
- [53] David Cheng. *Field and wave electromagnetics, second edition*. Addison-Wesley, 1989.
- [54] Jennifer E Houle and Dennis M Sullivan. *Electromagnetic simulation using the FDTD method with Python*. John Wiley & Sons, 2020.

- [55] Jean-Pierre Berenger. “A perfectly matched layer for the absorption of electromagnetic waves”. In: *Journal of computational physics* 114.2 (1994), pp. 185–200.
- [56] Dennis Sullivan, Jun Liu, and Mark Kuzyk. “Three-dimensional optical pulse simulation using the FDTD method”. In: *IEEE transactions on microwave theory and techniques* 48.7 (2000), pp. 1127–1133.
- [57] Akira Ishimaru. *Electromagnetic Wave Propagation, Radiation, and Scattering*. Prentice Hall, 1991.
- [58] Dennis M Sullivan. “Nonlinear FDTD formulations using Z transforms”. In: *IEEE Transactions on microwave theory and techniques* 43.3 (1995), pp. 676–682.
- [59] Dennis M Sullivan. “Z-transform theory and the FDTD method”. In: *IEEE Transactions on Antennas and Propagation* 44.1 (1996), pp. 28–34.
- [60] wolfies. *StackExchange*. 2017. URL: <https://stats.stackexchange.com/questions/203629/is-there-a-plateau-shaped-distribution> (visited on 08/10/2022).
- [61] Peter B Johnson and R-WJPrB Christy. “Optical constants of the noble metals”. In: *Physical review B* 6.12 (1972), p. 4370.
- [62] Weiya Zhang. “Effect of a thin optical Kerr medium on a Laguerre-Gaussian beam and the applications”. PhD thesis. Washington State University, 2006.
- [63] Joseph Lanska. “Optical wave propagation in photomechanical materials with arbitrary dispersive profiles”. PhD thesis. Washington State University, 2018.
- [64] Ph Prêtre et al. “Optical properties of nonlinear optical polymers: a method for calculation”. In: *JOSA B* 15.1 (1998), pp. 359–368.

## APPENDIX A: KERR APPROXIMATION COMPARISON

The Kerr approximation used in this work, derived from the Taylor series expansion, is

$$E_y^3(x, t_n) \approx 3E_y^2(x, t_{n-1})E_y(x, t_n) - 2E_y^3(x, t_{n-1}). \quad (\text{A.1})$$

This is a rewritten form of Eq. (2.48), shown here for convenience. Alternatively, if the electric field is changing slowly, the same approximation can be made using another method [1, 2, 3, 4]:

$$E_y^3(x, t_n) \approx E_y^2(x, t_{n-1})E_y(x, t_n). \quad (\text{A.2})$$

This second method can be used with the Kerr formulation and implemented in the same manner as the Taylor series expansion method that was used in Ch. 2.2.3. The accuracy of the two methods can be compared using a simple sine wave. For a 500 THz signal with an amplitude of 1, a sine wave is generated. A time step of  $2.1 \times 10^{-18} s$  is chosen, and both estimation methods are used to find  $E_y^3(x, t_n)$  based on the current value of the sine wave and its value at the previous time step. These estimates are then compared to the actual value of the sine wave cubed. The results are in Fig. A.1.

The error for both methods increases as the signal's frequency increases, since the signal changes by a larger amount between time steps. Figure A.2 shows a comparison similar to Fig. A.1, but for frequencies of 1500 and 2500 THz.

The signal in a nonlinear simulation will primarily be a combination of the fundamental signal and the first few harmonics. When a sine consisting of 500 THz, 1500 THz, and 2500 THz is used, Eq. (A.1) still outperforms Eq. (A.2), with the latter having approximately 30 times the error. This is shown in Fig. A.3.

Next, both methods are compared using an FDTD simulation of an electromagnetic wave. In this case, a Kerr cavity of 225 cells is created, and surrounded by mirrors, to the right of the origin of a right-moving wave. 992 cells of free space are located to the right of the cavity and mirrors. The simulation space is surrounded by a PML on both sides. The setup is depicted in Fig. A.4.

If the Kerr material has a small nonlinearity of  $\chi^{(3)} = 1 \times 10^{-5} \frac{cm^3}{erg}$ , both methods yield extremely similar results. A small amount of third harmonic is introduced regardless of the stability parameter of Eq. (2.17), as long as  $S \leq 1$ . Figure A.5 shows the transmitted waveforms and corresponding spatial Fourier transforms with the stability parameter  $S = 0.25$ .



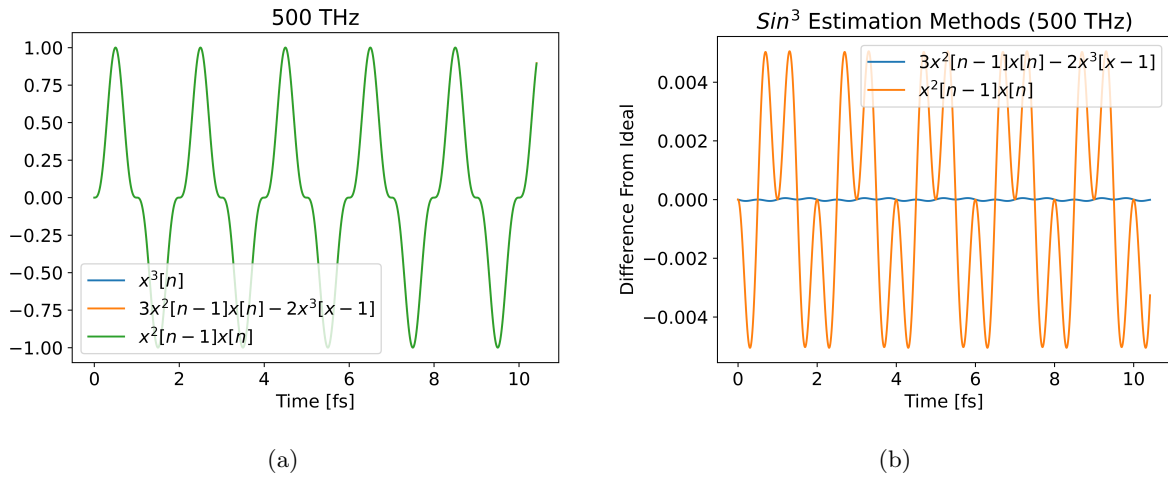


Figure A.1: (a) Comparisons of a sine wave cubed of 500 THz compared with the two estimation methods in Eq. (A.1) and Eq. (A.2), where  $x[n]$  is the sine wave at a particular time step. All three methods appear indistinguishable. (b) The difference between each estimation method and the actual sine wave cubed. The method of Eq. (A.1) is much more accurate, though both methods show small errors.

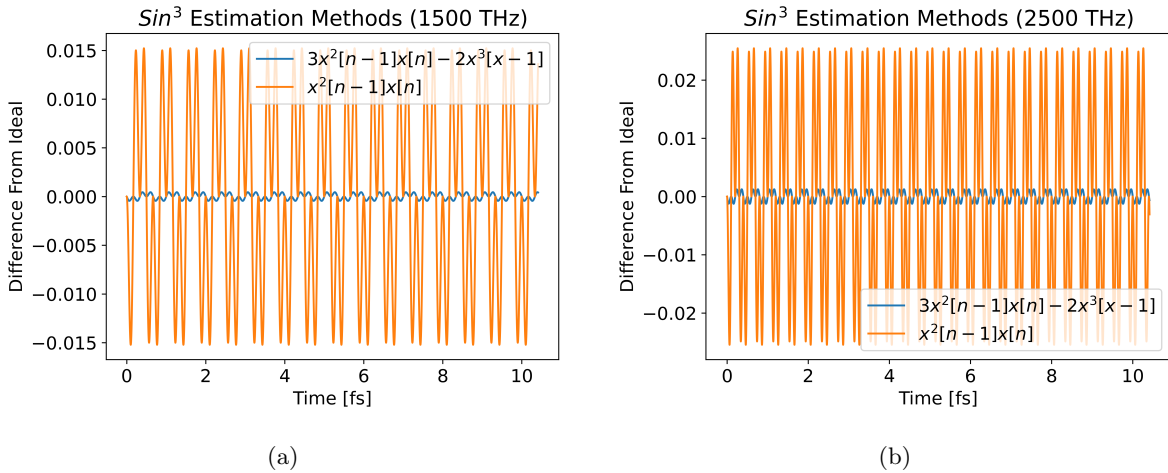


Figure A.2: Comparisons of a sine wave cubed compared with the two estimation methods in Eq. (A.1) and Eq. (A.2), where  $x[n]$  is the sine wave at a particular time step. (a) The sine wave is 1500 THz and (b) the sine wave is 2500 THz. The errors for both methods are small, though for 2500 THz, the error using Eq. (A.1) is less than 5% of the error using Eq. (A.2).

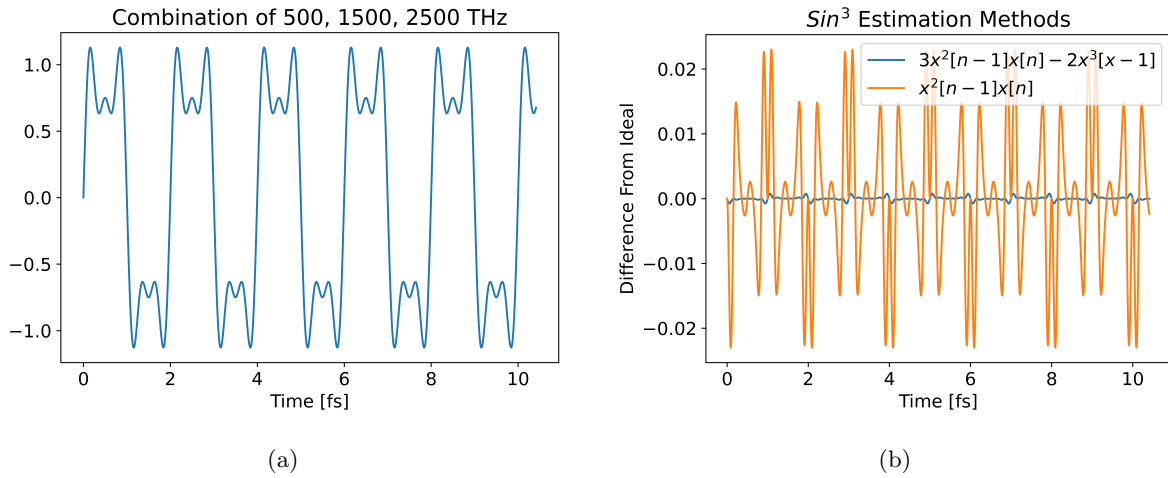


Figure A.3: (a) Plot of a sine wave with components at 500 THz, 1500 THz, and 2500 THz. (b) Comparison of the two estimation methods of Eq. (A.1) and Eq. (A.2) to the sine wave cubed. The errors for both methods are small, but the error using Eq. (A.1) is less than 3.5% of the error using Eq. (A.2).

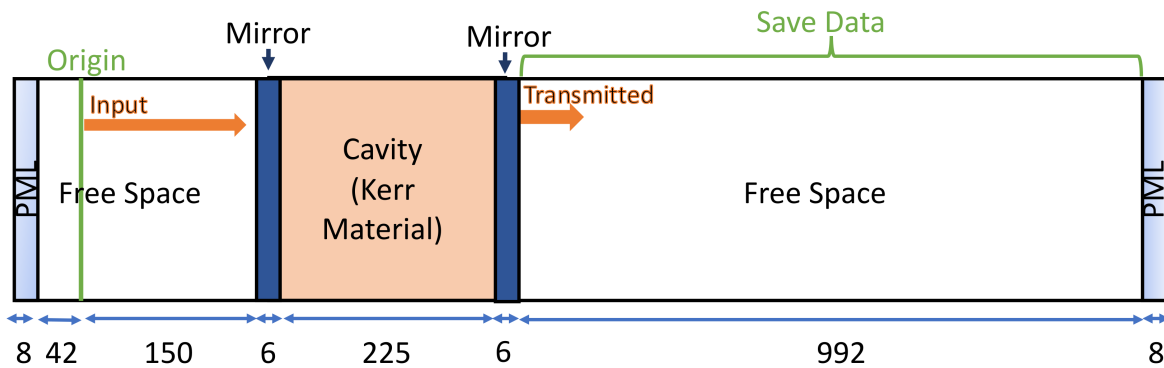


Figure A.4: Setup for the Kerr cavity simulation.

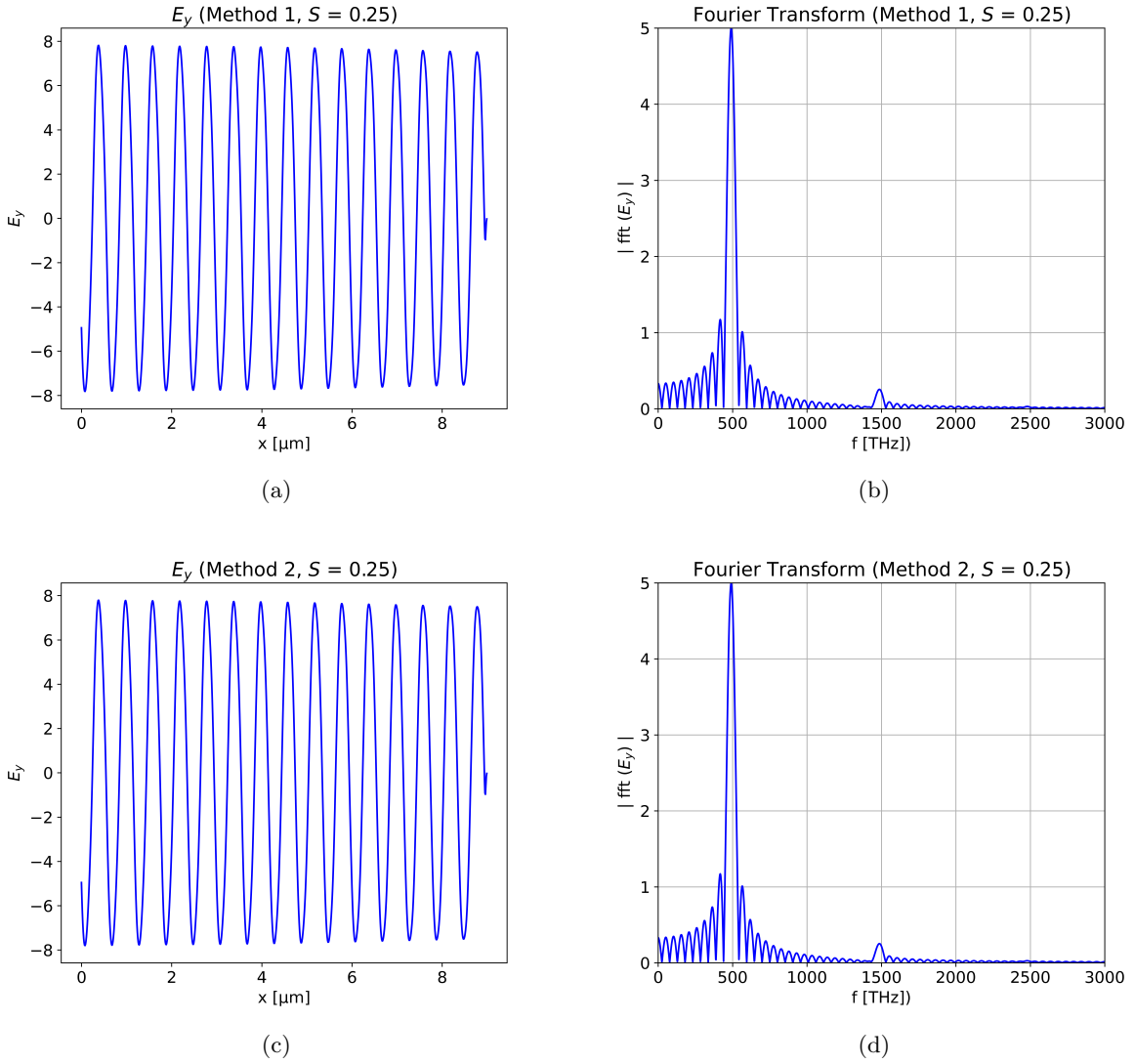


Figure A.5: Using the method of Eq. (A.1), (a) the transmitted wave from Fig. A.4 for a cavity with  $\chi^{(3)} = 1 \times 10^{-5} \frac{\text{cm}^3}{\text{erg}}$  and (b) the corresponding spatial Fourier transform. Using the method of Eq. (A.2), (c) the transmitted wave from Fig. A.4 for a cavity with  $\chi^{(3)} = 1 \times 10^{-5} \frac{\text{cm}^3}{\text{erg}}$  and (d) the corresponding spatial Fourier transform. Both results are similar.

If  $\chi^{(3)} = 5 \times 10^{-4} \frac{\text{cm}^3}{\text{erg}}$ , the methods begin to yield different results from each other. The method of Eq. (A.1) yields more higher frequency components for a given  $\chi^{(3)}$ .

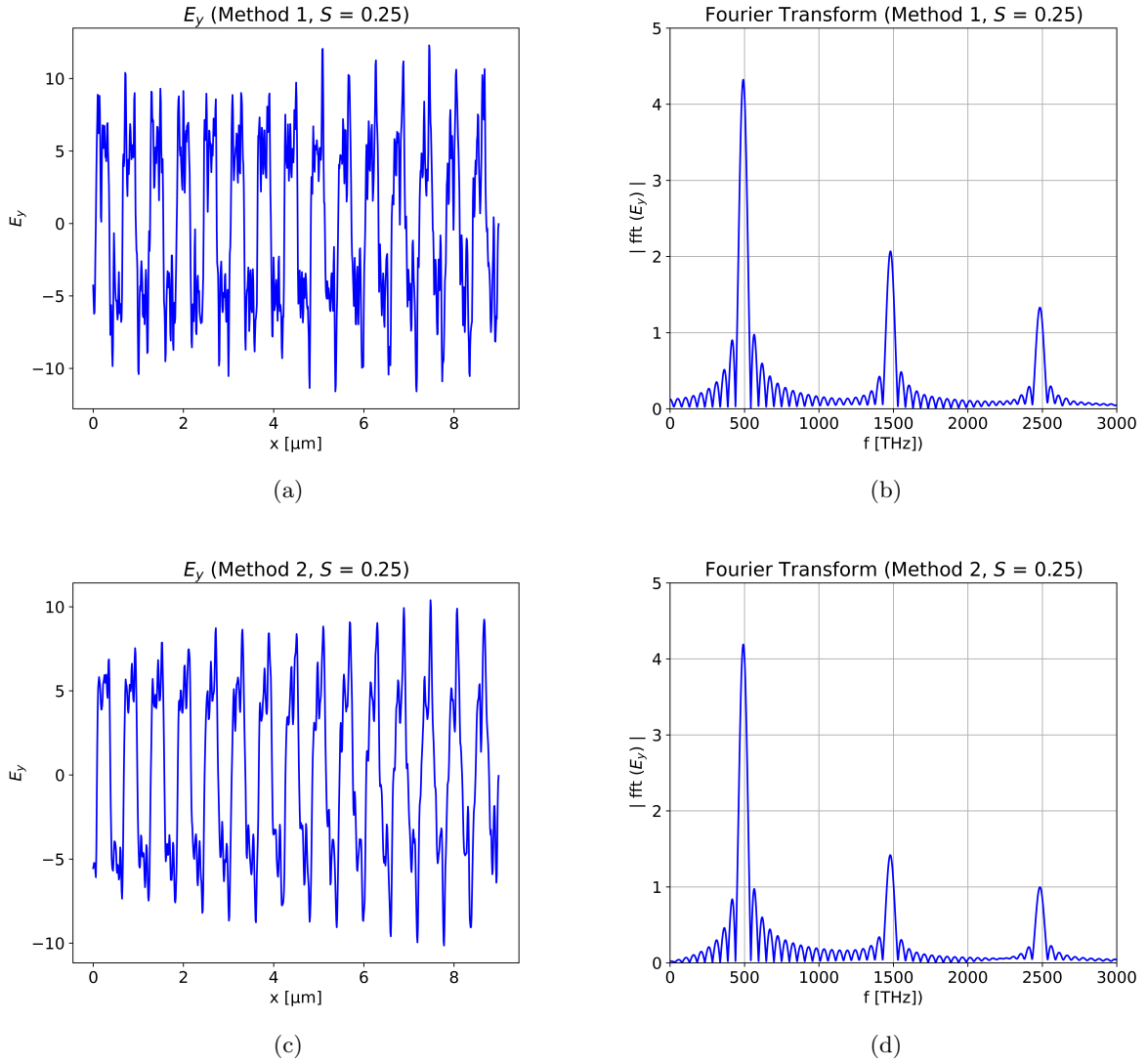
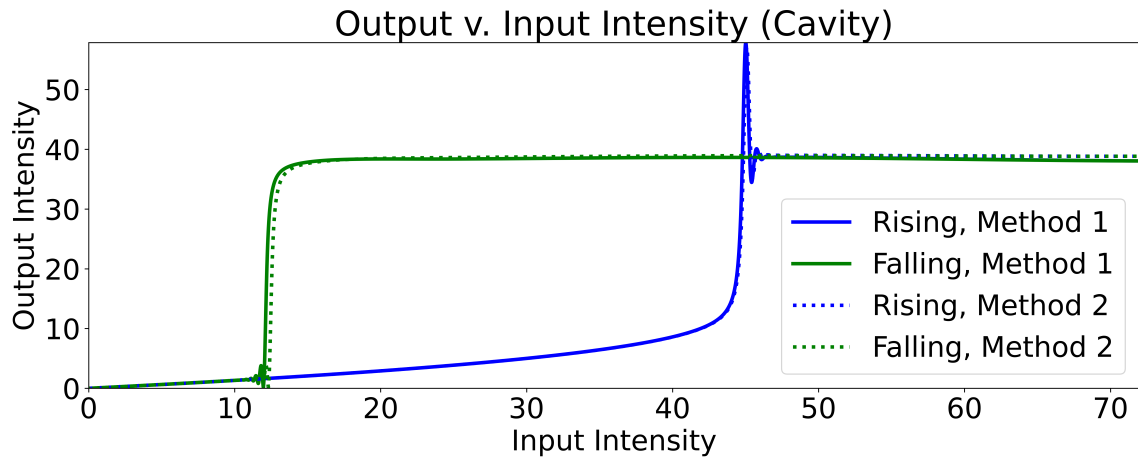


Figure A.6: Using the method of Eq. (A.1), (a) the transmitted wave from Fig. A.4 for a cavity with  $\chi^{(3)} = 5 \times 10^{-4} \frac{\text{cm}^3}{\text{erg}}$  and (b) the corresponding spatial Fourier transform. Using the method of Eq. (A.2), (c) the transmitted wave from Fig. A.4 for a cavity with  $\chi^{(3)} = 5 \times 10^{-4} \frac{\text{cm}^3}{\text{erg}}$  and (d) the corresponding spatial Fourier transform. Equation (A.1) results in more high frequency components.

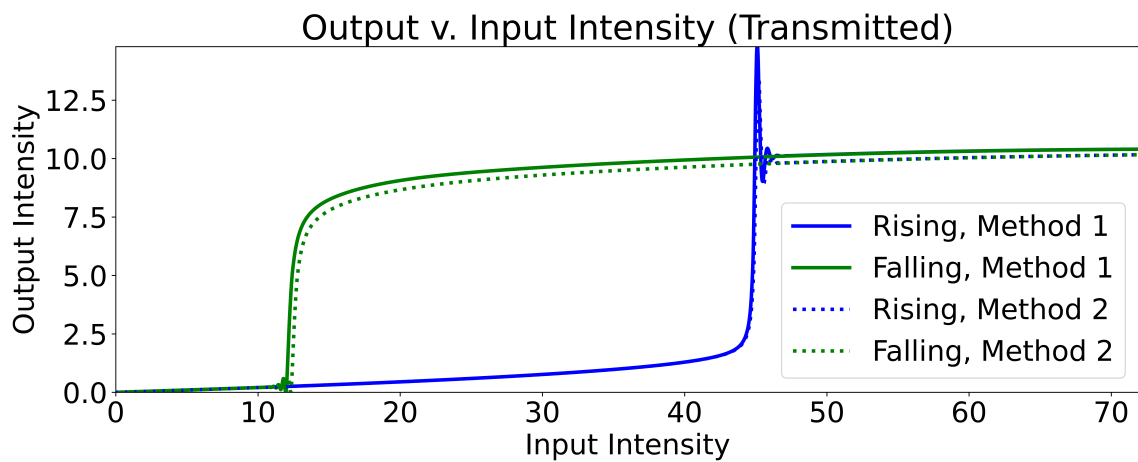
The effect of using Eq. (A.1) is that more nonlinearity appears in the results, as shown in Fig. A.6. With additional higher frequency components appearing, the simulation becomes less reliable for a given stability parameter and Kerr characteristics when using Eq. (A.1). Once higher frequency components appear, more resolution is needed to avoid missing information contained in the waveform. The method of Eq. (A.1) is used in this work because it has been shown to be more accurate in predicting pure sinusoids. Therefore, a greater amount of precision is used by employing a lower stability parameter.

Ultimately, the method of approximation has minor effects when looking at the time-averaged inten-

sity over time as, shown in Fig. A.7.



(a)



(b)

Figure A.7: Comparison of the two approximation methods of Eq. (A.1) and Eq. (A.2) when looking at the intensity versus input intensity for (a) the cavity, and (b) to the right of the cavity (transmitted). There is a small difference when looking at the falling edge of the transmitted signal.

## REFERENCES

- [1] Chen Lixue et al. “Finite-difference time-domain analysis of optical bistability with low threshold in one-dimensional nonlinear photonic crystal with Kerr medium”. In: *Optics communications* 209.4-6 (2002), pp. 491–500.
- [2] Ivan S Maksymov et al. “Comparative study of FDTD-adopted numerical algorithms for Kerr nonlinearities”. In: *IEEE Antennas and Wireless Propagation Letters* 10 (2011), pp. 143–146.
- [3] Weiya Zhang. “Effect of a thin optical Kerr medium on a Laguerre-Gaussian beam and the applications”. PhD thesis. Washington State University, 2006.
- [4] Joseph Lanska. “Optical wave propagation in photomechanical materials with arbitrary dispersive profiles”. PhD thesis. Washington State University, 2018.

## APPENDIX B: LORENTZ FORMULATION COMPARISON

The Lorentz formulation developed in Ch. 2.2.4 utilized the Z-transform [1, 2]. An alternate method is to use derivative approximations in the time domain [3, 4, 5]. The  $x$  indicating physical location is dropped within this appendix for more concise equations to allow easier comparisons between the methods, but the parameters are still a function of  $x$  as in Ch. 2.2.4. Converting Eq. (2.54) to the frequency domain and combining it with Eq. (2.57) results in

$$P_L(\omega) = \frac{1}{4\pi} \left( \frac{\omega_p^2}{\omega_0^2 + j\gamma\omega - \omega^2} \right) E_y(\omega). \quad (\text{B.1})$$

Rearranging the equation, it becomes

$$4\pi \left( \omega_0^2 + j\gamma\omega + (j\omega)^2 \right) P_L(\omega) = \omega_p^2 E_y(\omega), \quad (\text{B.2})$$

which can be converted back to the time domain using the inverse Fourier transform, resulting in

$$4\pi \left( \omega_0^2 P_L(t) + \gamma \frac{dP_L(t)}{dt} + \frac{d^2 P_L(t)}{dt^2} \right) = \omega_p^2 E_y(t). \quad (\text{B.3})$$

The derivatives can then be approximated with the central difference time domain method as

$$\frac{\partial F(t)}{\partial t} \cong \frac{F(n+1) - F(n-1)}{2\Delta t} \quad (\text{B.4})$$

and

$$\frac{\partial^2 F(t)}{\partial t^2} \cong \frac{F(n+1) - 2F(n) + F(n-1)}{(\Delta t)^2}. \quad (\text{B.5})$$

Using Eq. (B.4) and Eq. (B.5) with Eq. (B.3) results in

$$4\pi \left( \omega_0^2 P_L(t) + \gamma \frac{P_L(t+1) - P_L(t-1)}{2\Delta t} + \frac{P_L(t+1) - 2P_L(t) + P_L(t-1)}{(\Delta t)^2} \right) = \omega_p^2 E_y(t), \quad (\text{B.6})$$

which can be simplified using the notation of Ch. 2, with  $n$  representing the time step in a superscript, as

$$4\pi \left( \omega_0^2 P_L^n + \gamma \frac{P_L^{n+1} - P_L^{n-1}}{2\Delta t} + \frac{P_L^{n+1} - 2P_L^n + P_L^{n-1}}{(\Delta t)^2} \right) = \omega_p^2 E_y^n. \quad (\text{B.7})$$

This can again be rearranged to group the polarization at each time step together as

$$\left(\frac{\gamma\Delta t + 2}{2(\Delta t)^2}\right)P_L^{n+1} + \left(\frac{\omega_0^2(\Delta t)^2 - 2}{(\Delta t)^2}\right)P_L^n + \left(\frac{2 - \gamma\Delta t}{2(\Delta t)^2}\right)P_L^{n-1} = \frac{\omega_p^2}{4\pi}E_y^n. \quad (\text{B.8})$$

Then the polarization at the next time step can be solved for in terms of the polarization at the current and previous time steps, and in terms of the current electric field, as in

$$\left(\frac{\gamma\Delta t + 2}{2(\Delta t)^2}\right)P_L^{n+1} = -\left(\frac{\omega_0^2(\Delta t)^2 - 2}{(\Delta t)^2}\right)P_L^n - \left(\frac{2 - \gamma\Delta t}{2(\Delta t)^2}\right)P_L^{n-1} + \frac{\omega_p^2}{4\pi}E_y^n \quad (\text{B.9})$$

which simplifies to

$$P_L^{n+1} = \left(\frac{4 - 2\omega_0^2(\Delta t)^2}{2 + \gamma\Delta t}\right)P_L^n - \left(\frac{2 - \gamma\Delta t}{2 + \gamma\Delta t}\right)P_L^{n-1} + \left(\frac{2(\Delta t)^2}{2 + \gamma\Delta t}\right)\frac{\omega_p^2}{4\pi}E_y^n. \quad (\text{B.10})$$

This can be rewritten in the format previously used in Ch. 2.2.4 as

$$P_L^{n+1} = c_1P_L^n - c_2P_L^{n-1} + \frac{c_3}{4\pi}E_y^n, \quad (\text{B.11a})$$

$$c_1 = \frac{4 - 2\omega_0^2(\Delta t)^2}{2 + \gamma\Delta t}, \quad (\text{B.11b})$$

$$c_2 = \frac{2 - \gamma\Delta t}{2 + \gamma\Delta t}, \quad (\text{B.11c})$$

$$c_3 = \frac{2\omega_p^2(\Delta t)^2}{2 + \gamma\Delta t}. \quad (\text{B.11d})$$

The polarization in Eq. (B.11a) can be compared with Eq. (2.71b), repeated below and relabeled shifting the time steps to be on the whole versus half time step to keep the notation more concise:

$$P_L^{n+1} = c_1P_L^n - c_2P_L^{n-1} + \frac{c_3}{4\pi}E_y^n. \quad (\text{B.12})$$

Note the  $4\pi$  in Eq. (B.12) is present since this is written in terms of polarization instead of  $S_L$ . The coefficients, originally in Eq. (2.63), are

$$\gamma_1 = \frac{\omega_p^2}{\beta}, \quad (\text{B.13a})$$

$$c_1 = 2e^{-\alpha\Delta t} \cos(\beta\Delta t), \quad (\text{B.13b})$$

$$c_2 = e^{-2\alpha\Delta t}, \quad (\text{B.13c})$$

$$c_3 = \gamma_1\Delta t \cdot e^{-\alpha\Delta t} \sin(\beta\Delta t). \quad (\text{B.13d})$$



Rearranging Eq. (2.58) to convert  $\gamma$  and  $\omega_0$  to  $\alpha$  and  $\beta$ ,

$$\alpha = \frac{\gamma}{2}, \quad (\text{B.14a})$$

$$\beta = \sqrt{\omega_0^2 - \left(\frac{\gamma}{2}\right)^2}, \quad (\text{B.14b})$$

Eqs. (B.13) can be converted to

$$\gamma_1 = \frac{\omega_p^2}{\sqrt{\omega_0^2 - \left(\frac{\gamma}{2}\right)^2}}, \quad (\text{B.15a})$$

$$c_1 = 2e^{-\frac{\gamma}{2}\Delta t} \cos\left(\sqrt{\omega_0^2 - \left(\frac{\gamma}{2}\right)^2} \Delta t\right), \quad (\text{B.15b})$$

$$c_2 = e^{-\gamma\Delta t}, \quad (\text{B.15c})$$

$$c_3 = \gamma_1 \Delta t \cdot e^{-\frac{\gamma}{2}\Delta t} \sin\left(\sqrt{\omega_0^2 - \left(\frac{\gamma}{2}\right)^2} \Delta t\right). \quad (\text{B.15d})$$

Now these coefficients can be compared with those found using the central finite difference approximation in Eq. (B.11) [3]. The first term using the central finite difference approximation given in Eq. (B.11b) is

$$c_1 = \frac{4 - 2\omega_0^2 (\Delta t)^2}{2 + \gamma\Delta t} \approx \frac{4}{2 + \gamma\Delta t} \quad (\text{B.16})$$

using the condition that  $2\omega_0^2 (\Delta t)^2 \ll 1$  since there should be many time steps per period.

Using the Z-transform method, in which the approximation

$$\cos(\theta) \cong 1, \theta \ll 1 \quad (\text{B.17})$$

can be used along with

$$e^{-\delta} \cong \frac{1}{1 + \delta}, \delta \ll 1, \quad (\text{B.18})$$

the result is Eq. (B.15b) being approximated as

$$c_1 \approx \frac{2}{1 + \frac{\gamma}{2}\Delta t} = \frac{4}{2 + \gamma\Delta t} \quad (\text{B.19})$$

which is the same as Eq. (B.16) using the central finite difference approximation.

The second term in the derivation using the central difference approximation from Eq. (B.11c) is

$$c_2 = \frac{2 - \gamma\Delta t}{2 + \gamma\Delta t}. \quad (\text{B.20})$$

Table B.1: Comparisons of the Lorentz Formulations

Term	Central Finite Difference Approximation	Z-Transform	Approximation(s)	Critical Condition(s)
$c_1$	$\frac{4-2\omega_0^2(\Delta t)^2}{2+\gamma\Delta t}$	$2e^{-\frac{\gamma}{2}\Delta t} \cos\left(\sqrt{\omega_0^2 - \left(\frac{\gamma}{2}\right)^2}\Delta t\right)$	$\cos(\theta) \cong 1$ $e^{-\delta} \cong \frac{1}{1+\delta}$	$\theta \ll 1$ $\delta \ll 1$
$c_2$	$\frac{2-\gamma\Delta t}{2+\gamma\Delta t}$	$e^{-\gamma\Delta t}$	$e^{-2\delta} \cong \frac{1-\delta}{1+\delta}$	$\delta \ll 1$
$c_3$	$\frac{2\omega_p^2(\Delta t)^2}{2+\gamma\Delta t}$	$\frac{\omega_p^2\Delta t}{\sqrt{\omega_0^2 - \left(\frac{\gamma}{2}\right)^2}} e^{-\frac{\gamma}{2}\Delta t} \sin\left(\sqrt{\omega_0^2 - \left(\frac{\gamma}{2}\right)^2}\Delta t\right)$	$\sin(\theta) \cong \theta$ $e^{-\delta} \cong \frac{1}{1+\delta}$	$\theta \ll 1$ $\delta \ll 1$

Using the approximation [3]

$$e^{-2\delta} \cong \frac{1-\delta}{1+\delta}, \delta \ll 1, \quad (\text{B.21})$$

the Z-transform term in Eq. (B.15c) can be approximated as

$$c_2 = e^{-2\frac{\gamma\Delta t}{2}} \approx \frac{1 - \frac{\gamma\Delta t}{2}}{1 + \frac{\gamma\Delta t}{2}} = \frac{2 - \gamma\Delta t}{2 + \gamma\Delta t}, \quad (\text{B.22})$$

which is the same as the approximation using the central difference method in Eq. (B.20). Finally, the third term in the central difference approximation from Eq. (B.11d) is

$$c_3 = \frac{2\omega_p^2(\Delta t)^2}{2 + \gamma\Delta t}. \quad (\text{B.23})$$

The final term in the Z-transform, Eq. (B.15d), is approximated using Eq. (B.18) and

$$\sin(\theta) \cong \theta, \theta \ll 1 \quad (\text{B.24})$$

resulting in

$$c_3 \approx \frac{\omega_p^2}{\sqrt{\omega_0^2 - \left(\frac{\gamma}{2}\right)^2}} \Delta t \frac{1}{1 + \frac{\gamma}{2}\Delta t} \sqrt{\omega_0^2 - \left(\frac{\gamma}{2}\right)^2} \Delta t = \frac{2\omega_p^2(\Delta t)^2}{2 + \gamma\Delta t}, \quad (\text{B.25})$$

which is the same approximation as in Eq. (B.23) using the central difference approximation. Table B.1 shows the approximations using the central finite difference approximation and those using the Z-transform, as well as the relevant approximations used.

The Lorentz coefficients can be compared graphically as shown in Fig. B.1. These show the terms using both methods align well given the approximations of Table B.1.

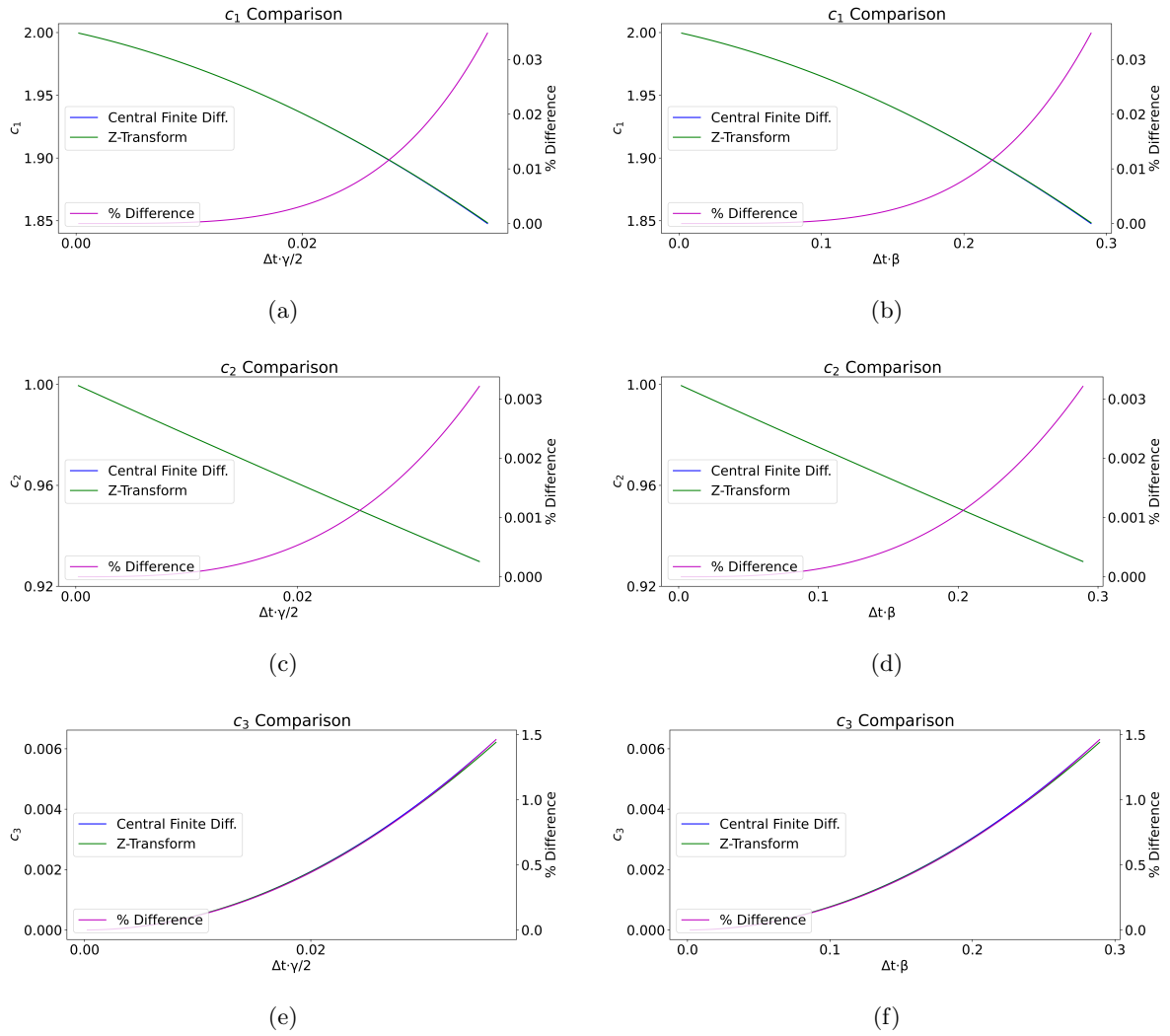


Figure B.1: Comparison of the coefficients defined in Eq. (B.11) and Eq. (B.15). The values are identical given that  $\Delta t \cdot \beta$  and  $\Delta t \cdot \gamma/2$  are small, with  $\beta$  related to  $\gamma$  and  $\omega_0$  in Eq. (B.14b).

## REFERENCES

- [1] Dennis M Sullivan. “Nonlinear FDTD formulations using Z transforms”. In: *IEEE Transactions on microwave theory and techniques* 43.3 (1995), pp. 676–682.
- [2] Dennis M Sullivan. “Z-transform theory and the FDTD method”. In: *IEEE Transactions on Antennas and Propagation* 44.1 (1996), pp. 28–34.
- [3] Jennifer E Houle and Dennis M Sullivan. *Electromagnetic simulation using the FDTD method with Python*. John Wiley & Sons, 2020.
- [4] Allen Taflov and Susan Hagness. *Computational electrodynamics: the finite-difference time-domain method, third edition*. Artech House Publishers, 2005.
- [5] Joseph Lanska. “Optical wave propagation in photomechanical materials with arbitrary dispersive profiles”. PhD thesis. Washington State University, 2018.

## APPENDIX C: THE PERFECTLY MATCHED LAYER (PML)

The PML is a type of boundary condition that is able to absorb outgoing waves at simulation boundaries with minimal reflection. This boundary condition has become widely used due to its ability to work in a wide variety of materials and in three dimensions. Although not necessary for one-dimensional simulations with free space at the edges of the simulation space, the PML was used in this work to make the simulation setup transferable to future simulations with more complex boundaries. The PML described here is a simplified version of that presented in [1]. The simplifications are due to the fact that the PML used here is only one-dimensional.

The PML requires that there be no reflection at the boundaries. The reflection coefficient,  $\Gamma$ , of a wave moving from material A to material B, given a lossless material at normal incidence, is given by

$$\Gamma = \frac{\eta_B - \eta_A}{\eta_B + \eta_A} \quad (\text{C.1})$$

where  $\eta_A$  is the impedance of material A and  $\eta_B$  is the impedance of material B. The impedance is given by

$$\eta = \sqrt{\frac{\mu}{\varepsilon}}, \quad (\text{C.2})$$

where  $\varepsilon$  is the permittivity and  $\mu$  is the permeability. The ideal PML will have a  $\Gamma = 0$ , so the impedances of the two materials will be equal. If one material has a higher  $\varepsilon$  than the other material, the  $\mu$  can be adjusted proportionally to keep the impedances of the two materials equal. In addition to the reflectivity, the wave must be absorbed in the PML. Otherwise, the wave will move through the PML without being reflected, but the boundary of the simulation space will still reflect the wave. To absorb the signal, the conductivity will need to be adjusted.

In the Fourier domain, Maxwell's equations from Eqs. (2.28) can be rewritten as [1]

$$j\omega D_y(x, \omega) = -c_0 \frac{\partial H_z(x, \omega)}{\partial x} \quad (\text{C.3a})$$

$$D_y(x, \omega) = \varepsilon_r^*(x, \omega) E_y(x, \omega) \quad (\text{C.3b})$$

$$j\omega H_z(x, \omega) = -c_0 \frac{\partial E_y(x, \omega)}{\partial x}. \quad (\text{C.3c})$$

Equations (C.3) use Gaussian units. Now, additional permeabilities and permittivities will be added to implement the PML. These quantities, which are not tied to any parameters in the real world, will be

called  $\varepsilon_{PML}^*$  and  $\mu_{PML}^*$ . They are used in Eqs. (C.3) to generate [1]

$$j\omega D_y(x, \omega) \varepsilon_{PML}^*(x) = -c_0 \frac{\partial H_z(x, \omega)}{\partial x} \quad (C.4a)$$

$$D_y(x, \omega) = \varepsilon_r^*(x, \omega) E_y(x, \omega) \quad (C.4b)$$

$$j\omega H_z(x, \omega) \mu_{PML}^*(x) = -c_0 \frac{\partial E_y(x, \omega)}{\partial x}, \quad (C.4c)$$

which multiplies  $D_y(x, \omega)$  by  $\varepsilon_{PML}^*(x)$  and  $H_z(x, \omega)$  by  $\mu_{PML}^*(x)$ . Since  $\varepsilon_{PML}^*(x)$  and  $\mu_{PML}^*(x)$  are not tied to any physical parameters, they can be inserted into the equations wherever is convenient, as opposed to multiplying  $E_y(x, \omega)$  by  $\varepsilon_{PML}^*(x)$ . The reason for the choice made here is to keep all the PML parameters in Eq. (C.4a) and Eq. (C.4c), while keeping the parameters related to the material in Eq. (C.4b). The parameters  $\varepsilon_{PML}^*(x)$  and  $\mu_{PML}^*(x)$  are complex to allow an adjustable surface charge density in each term. These then become [1]

$$\varepsilon_{PML}^*(x) = \varepsilon_{PML}(x) + \frac{\sigma_{PML}(x)}{j\omega} \quad (C.5a)$$

$$\mu_{PML}^*(x) = \mu_{PML}(x) + \frac{\sigma_{PML}(x)}{j\omega}, \quad (C.5b)$$

where  $\varepsilon_{PML}(x) = \mu_{PML}(x) = 1$  for simplicity. This satisfies the condition for the reflectivity coefficient being zero in Eq. (C.1) since the impedance, calculated with Eq. (C.2), is

$$\eta(x) = \sqrt{\frac{\mu_{PML}(x) + \frac{\sigma_{PML}(x)}{j\omega}}{\varepsilon_{PML}(x) + \frac{\sigma_{PML}(x)}{j\omega}}} = \sqrt{\frac{1 + \frac{\sigma_{PML}(x)}{j\omega}}{1 + \frac{\sigma_{PML}(x)}{j\omega}}} = 1 \quad (C.6)$$

for each location within the PML. The attenuation of the signal will originate from  $\sigma_{PML}(x)$ , which will increase in each PML cell when approaching the simulation boundaries, starting at zero. Using Eqs. (C.5), with the real components set to one in Eq. (C.4a) and Eq. (C.4c), results in

$$j\omega D_y(x, \omega) \left(1 + \frac{\sigma_{PML}(x)}{j\omega}\right) = -c_0 \frac{\partial H_z(x, \omega)}{\partial x} \quad (C.7a)$$

$$j\omega H_z(x, \omega) \left(1 + \frac{\sigma_{PML}(x)}{j\omega}\right) = -c_0 \frac{\partial E_y(x, \omega)}{\partial x}, \quad (C.7b)$$

which can be expanded to

$$j\omega D_y(x, \omega) + \sigma_{PML}(x) D_y(x, \omega) = -c_0 \frac{\partial H_z(x, \omega)}{\partial x} \quad (C.8a)$$

$$j\omega H_z(x, \omega) + \sigma_{PML}(x) H_z(x, \omega) = -c_0 \frac{\partial E_y(x, \omega)}{\partial x}. \quad (C.8b)$$

These can be converted back to the time domain, resulting in

$$\frac{\partial D_y(x, t)}{\partial t} + \sigma_{PML}(x)D_y(x, t) = -c_0 \frac{\partial H_z(x, t)}{\partial x} \quad (\text{C.9a})$$

$$\frac{\partial H_z(x, t)}{\partial t} + \sigma_{PML}(x)H_z(x, t) = -c_0 \frac{\partial E_y(x, t)}{\partial x}. \quad (\text{C.9b})$$

These equations can be discretized, using the FDTD methods of Ch. 2, to

$$\begin{aligned} \frac{D_y^{n+\frac{1}{2}}(i) - D_y^{n-\frac{1}{2}}(i)}{\Delta t} + \sigma_{PML}(i) \left( \frac{D_y^{n+\frac{1}{2}}(i) + D_y^{n-\frac{1}{2}}(i)}{2} \right) \\ = -c_0 \frac{H_z^n(i + \frac{1}{2}) - H_z^n(i - \frac{1}{2})}{\Delta x} \end{aligned} \quad (\text{C.10a})$$

$$\begin{aligned} \frac{H_z^{n+1}(i + \frac{1}{2}) - H_z^n(i + \frac{1}{2})}{\Delta t} + \sigma_{PML}\left(i + \frac{1}{2}\right) \left( \frac{H_z^{n+1}(i + \frac{1}{2}) + H_z^n(i + \frac{1}{2})}{2} \right) \\ = -c_0 \frac{E_y^{n+\frac{1}{2}}(i+1) - E_y^{n+\frac{1}{2}}(i)}{\Delta x}, \end{aligned} \quad (\text{C.10b})$$

which averages the  $\sigma_{PML}$  effect over two time steps. The fields calculated at the next time steps will be kept on the left side of the equation and everything else will be moved to the right side of the equation,

$$\begin{aligned} \left( \frac{2 + \sigma_{PML}(i)\Delta t}{2\Delta t} \right) D_y^{n+\frac{1}{2}}(i) \\ = \left( \frac{2 - \sigma_{PML}(i)\Delta t}{2\Delta t} \right) D_y^{n-\frac{1}{2}}(i) - \frac{c_0}{\Delta x} \left[ H_z^n\left(i + \frac{1}{2}\right) - H_z^n\left(i - \frac{1}{2}\right) \right] \end{aligned} \quad (\text{C.11a})$$

$$\begin{aligned} \left( \frac{2 + \sigma_{PML}\left(i + \frac{1}{2}\right)\Delta t}{2\Delta t} \right) H_z^{n+1}\left(i + \frac{1}{2}\right) \\ = \left( \frac{2 - \sigma_{PML}\left(i + \frac{1}{2}\right)\Delta t}{2\Delta t} \right) H_z^n\left(i + \frac{1}{2}\right) - \frac{c_0}{\Delta x} \left[ E_y^{n+\frac{1}{2}}(i+1) - E_y^{n+\frac{1}{2}}(i) \right], \end{aligned} \quad (\text{C.11b})$$

and this will finally be simplified to

$$\begin{aligned} D_y^{n+\frac{1}{2}}(i) \\ = \left( \frac{2 - \sigma_{PML}(i)\Delta t}{2 + \sigma_{PML}(i)\Delta t} \right) D_y^{n-\frac{1}{2}}(i) - \left( \frac{2c_0\Delta t}{\Delta x(2 + \sigma_{PML}(i)\Delta t)} \right) \left( H_z^n\left(i + \frac{1}{2}\right) - H_z^n\left(i - \frac{1}{2}\right) \right) \end{aligned} \quad (\text{C.12a})$$

$$\begin{aligned} H_z^{n+1}\left(i + \frac{1}{2}\right) \\ = \left( \frac{2 - \sigma_{PML}\left(i + \frac{1}{2}\right)\Delta t}{2 + \sigma_{PML}\left(i + \frac{1}{2}\right)\Delta t} \right) H_z^n\left(i + \frac{1}{2}\right) - \left( \frac{2c_0\Delta t}{\Delta x(2 + \sigma_{PML}\left(i + \frac{1}{2}\right)\Delta t)} \right) \left( E_y^{n+\frac{1}{2}}(i+1) - E_y^{n+\frac{1}{2}}(i) \right). \end{aligned} \quad (\text{C.12b})$$

Finally, the term in front of the spatially varying components will be rearranged. From Eq. (2.17), the coefficient can be simplified and rearranged to

$$\frac{2c_0\Delta t}{\Delta x(2 + \sigma_{PML}(i)\Delta t)} = \frac{2S}{2 + \sigma_{PML}(i)\Delta t} = \frac{S}{1 + \frac{\sigma_{PML}(i)\Delta t}{2}}. \quad (\text{C.13})$$

This allows Eqs. (C.12) to be rewritten as

$$D_y^{n+\frac{1}{2}}(i) = \left( \frac{1 - \frac{\sigma_{PML}(i)\Delta t}{2}}{1 + \frac{\sigma_{PML}(i)\Delta t}{2}} \right) D_y^{n-\frac{1}{2}}(i) - \left( \frac{S}{1 + \frac{\sigma_{PML}(i)\Delta t}{2}} \right) \left( H_z^n \left( i + \frac{1}{2} \right) - H_z^n \left( i - \frac{1}{2} \right) \right) \quad (\text{C.14a})$$

$$H_z^{n+1} \left( i + \frac{1}{2} \right) = \left( \frac{1 - \frac{\sigma_{PML}(i+\frac{1}{2})\Delta t}{2}}{1 + \frac{\sigma_{PML}(i+\frac{1}{2})\Delta t}{2}} \right) H_z^n \left( i + \frac{1}{2} \right) - \left( \frac{S}{1 + \frac{\sigma_{PML}(i+\frac{1}{2})\Delta t}{2}} \right) \left( E_y^{n+\frac{1}{2}}(i+1) - E_y^{n+\frac{1}{2}}(i) \right). \quad (\text{C.14b})$$

If a variable to represent the attenuation is defined as [1]

$$x_{att}(i) = \frac{\sigma_{PML}(i)\Delta t}{2}, \quad (\text{C.15})$$

it can be used in a set of auxiliary equations [1],

$$g_{d1}(i) = \frac{1}{1 + x_{att}(i)} \quad (\text{C.16a})$$

$$g_{d2}(i) = \frac{1 - x_{att}(i)}{1 + x_{att}(i)} \quad (\text{C.16b})$$

$$g_{h1} \left( i + \frac{1}{2} \right) = \frac{1}{1 + x_{att} \left( i + \frac{1}{2} \right)} \quad (\text{C.16c})$$

$$g_{h2} \left( i + \frac{1}{2} \right) = \frac{1 - x_{att} \left( i + \frac{1}{2} \right)}{1 + x_{att} \left( i + \frac{1}{2} \right)}, \quad (\text{C.16d})$$

$$(\text{C.16e})$$

which allows the simplification of Eqs. (C.14) to [1]

$$D_y^{n+\frac{1}{2}}(i) = g_{d2}(i)D_y^{n-\frac{1}{2}}(i) - g_{d1}(i)S \left( H_z^n \left( i + \frac{1}{2} \right) - H_z^n \left( i - \frac{1}{2} \right) \right) \quad (\text{C.17a})$$

$$H_z^{n+1} \left( i + \frac{1}{2} \right) = g_{h2} \left( i + \frac{1}{2} \right) H_z^n \left( i + \frac{1}{2} \right) - g_{h1} \left( i + \frac{1}{2} \right) S \left( E_y^{n+\frac{1}{2}}(i+1) - E_y^{n+\frac{1}{2}}(i) \right). \quad (\text{C.17b})$$

The PML absorption control will be done with Eq. (C.15). Since the purpose of this parameter is to absorb the signal within the PML, and  $\sigma_{PML}(i)$  is not tied to a real parameter, this entire equation can



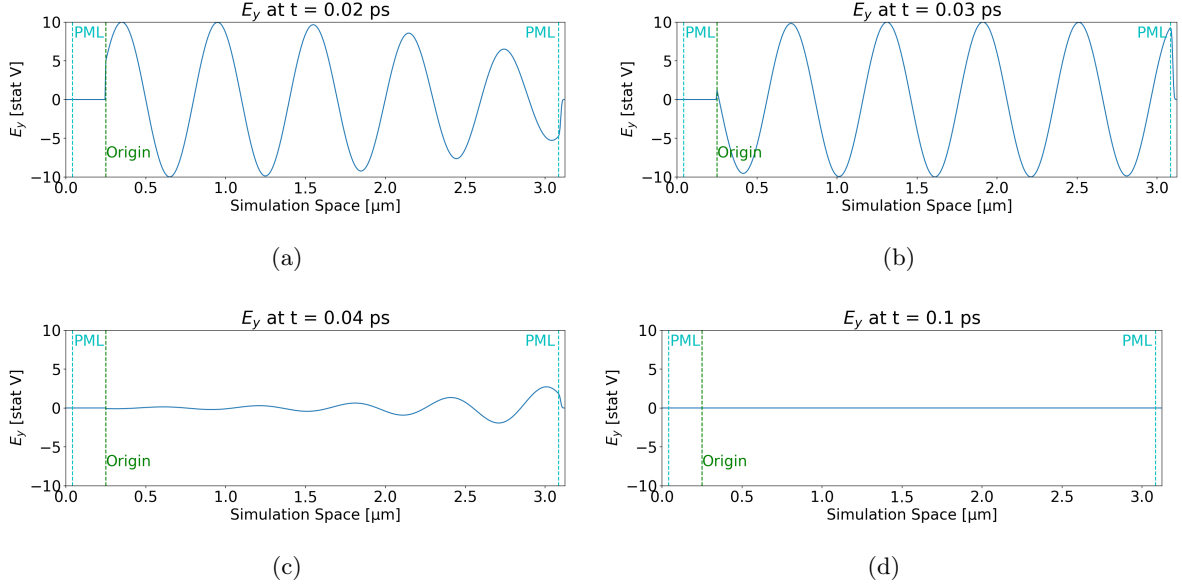


Figure C.1: The electric field at various times within the simulation space with a wave inserted at the origin moving right. (a-c) The right PML of eight cells absorbs the signal, and (d) eventually the entire signal has been absorbed.

be set using different arbitrary parameters. The important part is that the parameter changes slowly over the PML, beginning with a small amount of absorption at the edge adjacent to the main problem space and increasing as the cells approach the simulation space boundary. One possible replacement of Eq. (C.15) is [1]

$$x_{att}(i) = \frac{1}{3} \left( \frac{i}{n_{PML}} \right)^3, \quad (\text{C.18})$$

where  $n_{PML}$  is the number of cells in the PML at each boundary. In this work,  $n_{PML} = 8$ . Fig. C.1 shows a simulation of free space with an 8-cell PML. A single-directional sine wave within a Gaussian envelope is inserted into the simulation at the origin. The right PML absorbs the entire signal.

## REFERENCES

- [1] Jennifer E Houle and Dennis M Sullivan. *Electromagnetic simulation using the FDTD method with Python*. John Wiley & Sons, 2020.

## APPENDIX D: TOTAL FIELD/SCATTERED FIELD

The total field/scattered field approach is used to create a single-directional input pulse. This approach minimizes the input incident field to the simulation, reducing the amount of signal interacting with the boundary conditions. While the boundary conditions used in this work are nearly perfect and this is not a major concern, generating only one pulse is still desirable for simplicity in simulation analysis. Here, an extremely simple application of the total field/scattered field approach is described to create a single-directional input.

The basic FDTD loop, including a simple source, can be written as

$$E_y^{n+\frac{1}{2}}(i) = E_y^{n-\frac{1}{2}}(i) + S \left[ H_z^n \left( i - \frac{1}{2} \right) - H_z^n \left( i + \frac{1}{2} \right) \right] \quad (\text{D.1a})$$

$$E_y^{n+\frac{1}{2}}(\text{origin})_+ = \text{Input}^{n+\frac{1}{2}} \quad (\text{D.1b})$$

$$H_z^{n+1} \left( i + \frac{1}{2} \right) = H_z^n \left( i + \frac{1}{2} \right) + S \left[ E_y^{n+\frac{1}{2}}(i) - E_y^{n+\frac{1}{2}}(i+1) \right], \quad (\text{D.1c})$$

which is similar to Eqs. (2.19). The difference is the addition of a source at the origin cell. This is referred to as a soft source, since the input is added to existing data [1, 2]. A hard source would set the value at the origin to the input value instead and create a barrier for any reflected signals. The soft source shown here will allow reflected signals to pass through the point without interference. This simple soft source will generate one pulse moving to the left and one moving to the right as seen in Fig. D.1. The pulses travel in opposite directions, as apparent when looking at  $E_y$  and  $H_z$  on either side of the origin.

The reason for the creation of two pulses can be seen when looking at the  $E_y$  and  $H_z$  calculations around the origin. To look at  $H_z$  calculated to the right of the origin,  $i$  in Eq. (D.1c) is replaced by *origin* resulting in

$$H_z^{n+1} \left( \text{origin} + \frac{1}{2} \right) = H_z^n \left( \text{origin} + \frac{1}{2} \right) + S \left[ E_y^{n+\frac{1}{2}}(\text{origin}) - E_y^{n+\frac{1}{2}}(\text{origin} + 1) \right]. \quad (\text{D.2a})$$

This shows that  $H_z^{n+1} \left( \text{origin} + \frac{1}{2} \right)$  is based on  $E_y^{n+\frac{1}{2}}(\text{origin})$ , which was updated with the input value in Eq. (D.1b). If the input at that time is greater than zero,  $E_y^{n+\frac{1}{2}}(\text{origin})$  will increase in value, and so will  $H_z^{n+1} \left( \text{origin} + \frac{1}{2} \right)$ . For an input signal, if both  $E_y$  and  $H_z$  are positive, the wave moves in the positive x-direction. On the other hand, when looking at  $H_z$  to the left of the origin, replacing  $i$  in

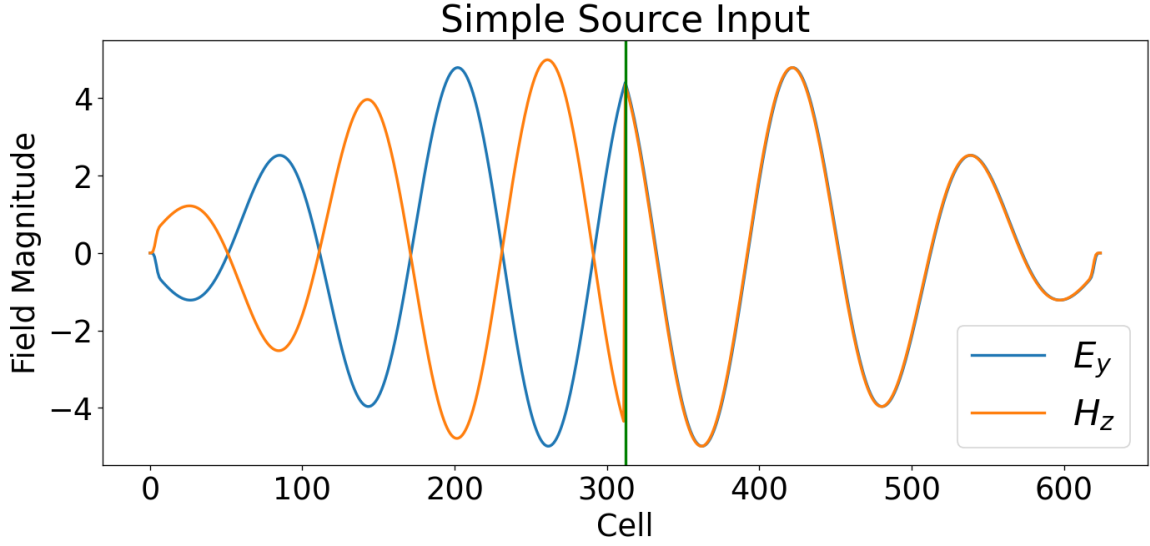


Figure D.1: An input to an FDTD simulation with a simple input sinusoid added to  $E_y$ , in the manner of Eqs. (D.1), at the center of the simulation space, represented by the vertical green line.

Eq. (D.1c) with  $origin - 1$ , results in

$$H_z^{n+1} \left( origin - \frac{1}{2} \right) = H_z^n \left( origin - \frac{1}{2} \right) + S \left[ E_y^{n+\frac{1}{2}}(origin - 1) - E_y^{n+\frac{1}{2}}(origin) \right]. \quad (D.3a)$$

This shows  $H_z^{n+1} \left( origin - \frac{1}{2} \right)$  is also updated based on  $E_y^{n+\frac{1}{2}}(origin)$ . This time, if the input is greater than zero and  $E_y^{n+\frac{1}{2}}(origin)$  increases,  $H_z^{n+1} \left( origin - \frac{1}{2} \right)$  will decrease. If  $E_y$  is positive and  $H_z$  is negative, the wave moves in the negative  $x$  direction.

Instead of the simple source, a single-directional source was used in this work. Since adding an input to  $E_y$ , as seen in Eq. (D.1b), creates a two-directional pulse, the principle of the total field/scattered field can be used to cancel out the input on  $H_z$  to the left of the origin. A simple way to implement that is

$$E_y^{n+\frac{1}{2}}(i) = E_y^{n-\frac{1}{2}}(i) + S \left[ H_z^n \left( i - \frac{1}{2} \right) - H_z^n \left( i + \frac{1}{2} \right) \right] \quad (D.4a)$$

$$E_y^{n+\frac{1}{2}}(origin)_+ = Input^{n+\frac{1}{2}} \quad (D.4b)$$

$$H_z^{n+1} \left( i + \frac{1}{2} \right) = H_z^n \left( i + \frac{1}{2} \right) + S \left[ E_y^{n+\frac{1}{2}}(i) - E_y^{n+\frac{1}{2}}(i+1) \right] \quad (D.4c)$$

$$H_z^{n+1} \left( origin - \frac{1}{2} \right)_+ = Input^{n+\frac{1}{2}-\delta}, \quad (D.4d)$$

which is Eqs. (D.1) with one additional line. The time offset  $\delta$  will be described below. If a positive

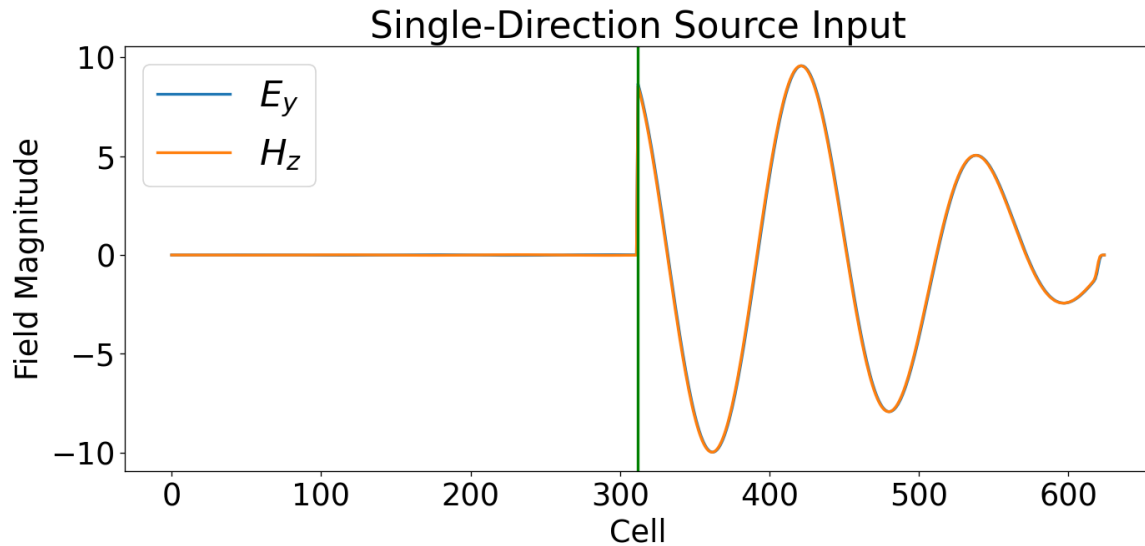


Figure D.2: An input to an FDTD simulation with a single-directional input sinusoid added to  $E_y$  at the center of the simulation space, represented by the vertical green line. The input is defined by Eqs. (D.4) and (D.5).

input is added to  $E_y$ ,  $H_z$  to the left of the origin will be negative, as shown in Fig. D.1. Therefore addition is required to cancel the input to the left of the origin. The  $\delta$  here must account for the time it takes the input to cross a one half cell. The half cell offset is due to the Yee cell configuration of Fig. 2.1. This  $\delta$ , assuming the medium is free space and the signal is moving at the speed of light  $c_0$ , is

$$\delta = \frac{1}{2} \left( \frac{\Delta x}{c_0} \right) \frac{1}{\Delta t} = \frac{1}{2} \frac{\Delta x}{c_0 \Delta t} = \frac{1}{2S}, \quad (\text{D.5})$$

with  $S$  defined in Eq. (2.17). The time offset,  $\delta$ , is defined in terms of time steps and must be a whole number. To convert this to an amount of time measured in seconds, it would need to be multiplied by  $\Delta t$  in the usual manner. The input now moves only in the positive x-direction using Eqs. (D.4) and (D.5), as shown in Fig. D.2.

## REFERENCES

- [1] Allen Taflov and Susan Hagness. *Computational electrodynamics: the finite-difference time-domain method, third edition*. Artech House Publishers, 2005.
- [2] Jennifer E Houle and Dennis M Sullivan. *Electromagnetic simulation using the FDTD method with Python*. John Wiley & Sons, 2020.